II. International Conference on Engineering Sciences

المؤتمر الدولي الثاني للعلوم الهندسية

II.Uluslararası Mühendislik Bilimleri Konferansı

Rimar Academy
أكاديمية ريمار

2025

المؤتمر الدولي الثاني للعلوم الهندسية

كتاب الوقائع

TAM METIN KITABI

2025

ISBN 978-625924390-0

YAYINEVI:	دار النشر:	RIMAR ACADEMY
EDITÖR:	المحرر:	Prof. Dr. Ghuson H. MOHAMMED
YAYIN KOORDINATÖRÜ:	تنسيق النشر:	AMIR MUAENI
ISBN:	نظام الترميز الدولى لترقيم الكتاب :	978-625-92439-0-0
DOI :	رقم معرف الكائن الرقمي:	http://dx.doi.org/10.47832/EngConf1
BASKI:	تاريخ الطباعة:	02 / 11 / 2025
KONGRE TARIHI:	تاريخ المؤتمر:	20 - 21 - 22 / 08 / 2025
SAYFALAR:	عدد الصفحات:	123
URL:	رابط النشر:	WWW.RIMARACADEMY.COM
NO SERTIFIKASI MATBAA:	رقم شهادة المطبعة:	47843

PREFACE

II. International Conference on Engineering Sciences was organized by Igdir University in collaboration with Rimar Academy. The primary objective of this event was to compile and disseminate valuable scientific knowledge andmake ameaningful contribution to the future.

A substantial number of researchers from both local and international backgrounds demonstrated their interest in this conference. The scientific committee meticulously reviewed the submissions and ultimately accepted a select group of applicants—20 in total—of whom 15 were approved by the scientific committee.

The core of this conference was the presentation of 13 full research papers, while the remaining articles and research findings are set to be featured in for the coming issues of the MINAR Journal.

I would like to extend my sincere appreciation to all the contributors and scholars who played an essential role in making this conference a resounding success. Your dedication and valuable contributions are deeply respected and acknowledged.

Editor-in-Chief
Prof. Dr. Ghuson H. MOHAMMED

الرؤساء الفخريون
HONORARY COMMITTEE

الأستاذ الدكتور زكريا ظلام
Prof. Dr..Zakaria ZALLAM
جامعة غازي عنتاب
Gaziantep University
Türkiye-تركيا

الأستاذ الدكتور وعد محمود رؤوف
Prof. Dr. Waad Mahmood RAOOF
رئيس جامعة تكريت
Rector of Tikrit University
Iraq - العراق

الأستاذ الدكتور علياء عباس علي العطار
Prof. Dr. Alyaa A. Ali Al-ATTAR
رئيس الجامعة التقنية الشمالية
Rector of Northern Technical University
Iraq - العراق

الأستاذ الدكتور طارق حفظي الخياط
Prof. Dr. Tariq Hafdhi Abbd Tawfeeq
رئيس جامعة الفراهيدي
Iraq - العراق

الأستاذ الدكتور ثائر سعود الغشام
Prof.Dr.Thaar S Al-Gasham
رئيس جامعة واسط
Rector of the University of Wasit
Iraq - العراق

الأستاذ الدكتور عباس لفته كنيهر
Prof Dr Abbas Lafta Kneehr
رئيس جامعة واسط
Rector of the University of Wasit
Iraq - العراق

رئيس المؤتمر
CHAIR OF CONGRESS

Prof. Dr. Ghuson H. MOHAMMED

Baghdad University

Iraq

الهيئة التحضيرية
ORGANIZING COMMITTEE

Prof. Dr. Abbas Fadhil Ibrahim
University of Technology
Iraq

Prof. Yasser Estanbouli
Aleppo University
syria

Dr.Rehab Mahmoud Ibrahim Ibrahim sayed ahmed
University of Engineering and Technology
Egypt

Dr. Muna Faeq Ali Al-Araji
University of Baghdad
Iraq

Dr. Lamya M. J. Mahdi Al-Saeed
University of Technology
Iraq

Lect. Dr.Ahmad N.AL-SHAMMAA
University of Baghdad
Iraq

Dr.Ali Abed Asal Al-Graiti
college of engieering
Iraq

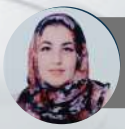

Dr. Hadeel Mowaffaq Mahmood Al Qaicy
University of Technology
Iraq

الهيئة العلمية
SCIENTIFIC BODY

Assist. Prof. Dr. Abdal Jabbar Saad Jomah Al Jubory
University of Diyala
Iraq

Assist. Prof. Dr. Ahmed I. Jaber
University of Diyala
Iraq

Assist. Prof. Dr. Ali H. Numan
University of Technology
Iraq

Assist. Prof. Dr. Mohammed Molhem
Alayen Iraqi University
syria

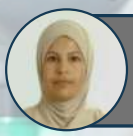

Assist. Prof. Dr. Intisar A.M. Al Sayed
Uruk University
Iraq

Assist. Prof Dr. Huda Hamdan Ali
Imam Kadhim College
Iraq

Assist. Prof. Dr. Mohammed Salih Ahmed
University of Tikrit
Iraq

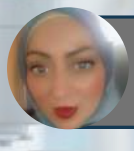

Assist. prof. shaimaa Muthana Abudlrhman
University of Technology
Iraq

Assist. Prof. Ruaa Haitham Abdul Raheem
University of Technology
Iraq

Lect. Dr.Mohammed Falah Mohammed
University of Mosul College of Engineering Mechatronics Departmen
Iraq

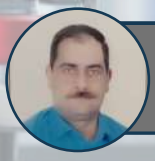

Lect. Dr. Bilal Ahmed Hbeeb
University of Technology
Iraq

Lect. Dr. Sabah Noori Hammoodi Al Ani
Ashur Private University
Iraq

Dr. Zainab Falih Alkhazaali
ibn sina university
Iraq

Dr. Souad Kamal Mekni
University of Jeddah
Alsueudia

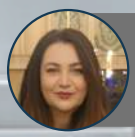

Dr. Gainullina Leysan
Kazan State Power Engineering University
Russia

Assist. Prof . Dr Mahmood ismael Mohammed
University of baghdad
Iraq

Assist. Prof. Dr. Adil Hatem Nawar Aldulaymi
Al-Huda University
Iraq

Assist. Prof. Dr. Ahmed Hameed Kaleel
University of Baghdad
Iraq

INDEX


KAWADA

Analysis of Chaotic Dynamics, Particle Trajectories, and Average Particle Velocity Using Poincaré Maps for Nonlinear Vibrations

Sajad W. Noori [1]

Duaa Alaa Lafta [2]

Mustafa M. Mansour [3]

Alaa M. lafta [4]

Abstract:

This work examines the dynamics of particle paths and the mean particle velocity in systems exhibiting nonlinear behavior. This work also uses the Poincaré mapping technique. The nonlinear vibratory systems are most famous for their elaborate frame that results to complex motion, referred to as chaotic motion of which the characterization is normally hard when common techniques are employed. The paper focuses on the presentation of the tool, known as Poincaré maps, and their application to analyze the paths of particles within the discussed systems, with an example of transition from periodic to chaotic motion. Through the calculation of the intersections of two particle paths on the Poincaré section, the study gains further understanding of the stability, bifurcations, and chaos of nonlinear oscillators. Additionally, the correlation between the chaotic behavior and the mean particle velocity is also considered to provide insights into how chaotic motion degrades performance. Thus, the results imply that using Poincaré maps as an investigative tool, it is possible to achieve a better insight into the type of chaotic vibrations, the causes leading to them, and their influence on the overall dynamics of the function.

Keywords: *Chaotic Resonance, Particle Velocity, Neural System, Lyapunov Exponent, Chaos Control, Synchronization.*

http://dx.doi.org/10.47832/EngConf1-1

[1] Researcher. College of engineering, University of Thi-Qar, Iraq sajadthiqar1990@gmail.com

[2] Researcher. College of engineering, University of Thi-Qar, Iraq doaalafta23@gmail.com

[3] Researcher. College of engineering, University of Thi-Qar, Iraq mustafa.muhammedali@utq.edu.iq

[4] Researcher. College of engineering, University of Thi-Qar, Iraq a.mohammed1003@coeng.uobaghdad.edu.iq

1. Introduction

In general, nonlinear vibrations are an inherent feature of many physical and engineering systems, oscillators, structures, and biological processes. Such a perspective diverges from the inherently stable and ordered behavior of linear systems, in contrast to their nonlinear counterparts, which may exhibit signs of chaos. The fact that chaos is fundamental to the applications and analysis of the asymptotic properties of nonlinear vibratory systems is important in various contexts, including resonance, energy transfer, and stability, with applications in structural engineering, materials science, and robotics. Among all tools used for studying chaotic systems, the Poincaré map is one of the most effective methods in determining the approximations of the trajectories that lie inside the subspace of specified dimension. The use of Poincaré maps enables one to determine regions of period and chaos, bifurcations and attractors, and thereby, provides useful information regards the dynamic behavior of the system [1]. The main concern of this work is to apply Poincaré maps to investigate chaotic motion, particle orbits, and mean particle speed in nonlinear oscillatory systems. Thus, the goal of the research is to study the relations between the system parameters and its chaotic dynamics, and how the chaotic motion affects the performance with regard to particle velocities and stability. Towards this end, the study aims to extend knowledge of more effective ways to control and/or exploit chaotic motion as a viable means in engineering. It not only enriches the theoretical system of nonlinear vibrations but also provides a reference for optimizing the design and analysis of vibratory systems and for controlling nonlinear vibrations in engineering applications [2].

1.1. Background and Motivation:

One of the fundamental issues in nonlinear vibrations, which makes it attractive, is the capability to cover a large selection of excitation frequencies, therefore obeying some general low-frequency electrodynamics laws. Note that such dynamical features make the nonlinear vibration analysis useful for both philosophical discussions and technical applications. For instance, in seismology, it helps to understand crucial structural features, design actuators for suspension devices, and control oscillators in self-synchronizing systems, as well as in electrical power systems, such as synchronous generators and innovative particle accelerators. Furthermore, the nonlinear dynamics can be coupled or even confined because of spacetime physics, quantum mechanics, gravity, or the Lorentz force, under the lens of electromagnetism for several proposed and unexplored use cases [3].

Indeed, as precursor works, we believe that the study of paradigms and the development of conceptual applications driving the main points of nonlinear dynamics, which are mainly through the chaotic glimpse, can enlighten others in Non-intrusive load monitoring(NILMs) and other applications at the interface of nonlinear dynamics, electromagnetism, spacetime physics, and quantum mechanics. By applying the Poincaré map, we are able to identify the appearance of a limit cycle and compare the behavior of particle trajectories along one excitation cycle [4]. No temporal applied potential is imposed anymore, just the system's intrinsic nonlinear forces, as several NILMs in applied sciences

seem to do for a variety of proposals mainly made in the condensed matter field. The next section addresses the dynamic system model, assumptions, and implementation of the Poincaré map. Some numerical simulations using different values for excitation frequencies have been performed, considering the ordinary differential equation model parameters as natural choices. At last, we present the original concepts in this paper and some conclusions for future NILM analysis, as well as for the explored and unexplored areas of applied research in electromagnetism as a whole [5].

1.2. Research Objectives:

The aim of this work is to study the Poincare mapping of nonlinear vibrant systems, to show the transition of period doubling to chaos through intersection of trajectories. This way, the research concern of the present work is to study the particle trajectories in these systems and describe time evolution and chaotic structure. Moreover, it aims at checking the correlation between the chaotic motions and mean particle velocity to evaluate the impacts of chaotic motion to velocity distribution as well as system efficiency. This way, the study shall explain bifurcations and stability of the Poincaré maps focusing at the crucial parameters of the chaotic motion. In addition, this research will seek to gain knowledge of the effects of the chaotic behavior to the static and dynamic performances of non-linear oscillators that will go a long way in describing performances of engineering and physical systems in the future. Last but not least, it is expected that this study will providethe framework for employing the theory of Poincaré maps as the analytical tool for the examination of the phenomenon of nonlinear vibrations thus contributing to enhancing the usage of vibratory processes in various branches of engineering.

2. Fundamentals of Nonlinear Vibrations

The theory of non-autonomous vibrations is suitable mainly for the analysis of systems subject to time-varying conditions classified as deterministic or chaotic. Chaotic systems are not on any level the type familiar from linear differential equations. These take a system from one state to some other state as time passes, in a well-understood way [6]. The main features typical of chaotic systems are sensitivity to initial conditions and mixing. Chaotic behavior is one that is highly sensitive to initial conditions. During transient chaos, solution points that are initially close together diverge exponentially quickly; that is, they move away from each other in the phase space in an exponentially fast manner. After a characteristic time, these solutions become uncorrelated [7].

The phenomena of quick chaos organization, high sensitivity to initial conditions, unpredictability, and hypersensitivity of nonlinearities are thus typical of highly nonlinear systems. Extremely complex chaotic systems exist in which continuum fracture models dominate. These complex ensembles consist of a large number of cooperating nonlinear processes of strongly overbalanced sensitivity. Such systems are difficult to study as a whole using principally statistical physics or time series analysis, since the phenomenon does not provide the correlation length necessary for monumental concepts of near-critical metrics [8]. The study of non-autonomous systems has two approaches: passive and active. Despite

the fact that the choice of the approach can complicate the effective tracking of experimentally available partial quantities, both Theoretical and practical solutions depend on the knowledge of chaotic system dynamics [9].

2.1. Overview of Vibrations and Dynamics:

Vibrations are the most common type of mechanical motion encountered in engineering science. Systems such as machine components, airplane structures, bridges, pressure vessels, aircraft, spacecraft, and automotive components all exhibit free and forced vibrations caused by pushing or pulling forces and electrical or magnetic forces due to loads generated by pressure and temperature differentials [10]. These loads can cause deformations and oscillatory motion over the entire system. Certain well-defined conditions must be met for such motion to be referred to as "vibrations." First, the body undergoing motion must have a well-founded, static equilibrium position that, when disturbed slightly, will produce a Restoring force causing the body to return to the state of equilibrium. Second, sufficiently few internal damping forces must be applied to control the motion so the pulse persists [11].

But even with no friction in the system or loss of energy, sometimes the angle of vibration could reach too high constants. It is actually the case for most mechanical systems. This results in chaotic vibrations. The high level of oscillating motion to be reached is the production of chaotic vibrations, and from the simplified method, they manage to find phase diagrams, fractal dimension, and particle velocity of vibrating systems [12].

2.2. Nonlinear Systems and Chaos Theory:

A dynamical system with a continuous transformation has a small dimension and is called a continuum. In this study, the nonlinear nature of the substrate and microresonators is effective for reducing the dimension of the continuum by the numerical simulation, and we consider the dynamics using a linear partial differential equation. In addition, a linear vibration model is used to obtain the basic properties of the resonance frequency and the threshold displacement in this study. Chaos theory was developed from nonlinear dynamics and concerns the behavior of nonlinear dynamical systems that appear to be random for many initial conditions [13]. There are two types of chaos: orbit chaos, which we associate with the sensitivity to initial conditions, and continuous chaos, which takes a packet of localized excitation and spreads it spatially. In this study, the chaotic dynamics presented by the resonance of micromechanical devices is associated with orbit chaos, and three types of resonators are investigated in the first instance to ascertain the importance of boundary characteristics at the interface of the thin film and substrate [14].

3. Poincaré Maps and Their Applications

In recent years, a powerful tool that has attracted attention in the analysis of nonlinear mathematical models describing chaotic physical phenomena is known as a Poincaré section. When exact analytical solutions to such models are not available, the computation of trajectories on a section usually provides a qualitative and quantitative understanding of chaotic behavior. This approach avoids integrations of considerable

lengths present in other tools, primarily using the fact that much relevant information can be visualized only in a Poincaré plot. In mechanics, Poincaré maps or Poincaré surfaces of section have been used to map one-dimensional return trajectories onto a two-dimensional plane. Poincaré maps are used to calculate maximum response in the vicinity of a principal parametric resonance in structures having nonlinearities of the softening type [15].

A technique often used in the investigation of the dynamic response of mechanical systems is the application of a Poincaré map of the displacement of the vibrating structure as a function of its velocity. In the associated scalar diffeomorphisms, there are points that correspond to at least one bifurcation to a chaotic state, and a region that corresponds to quasi-chaotic dynamics [16]. The critical values of the parameters have been obtained for the occurrence of these bifurcations and in the establishment of the existence area of the quasi-chaotic dynamics. One of the ways to reduce computational costs of the numerical integration of the differential equations used in the study of nonlinear hyperbolic systems is to use techniques of dimension reduction to transversely section these systems, constructing Poincaré maps that allow the system to be investigated on the section. The construction of these maps is deterministic and directly connected to the geometric features of the phase space. In this paper, we study a particular map dedicated to particle traffic which we call the hyperbolic [17].

3.1. Definition and Concept of Poincaré Maps:

The concept of Poincaré maps is a result of Poincaré's investigation of the periodic solutions of a nonlinear pendulum subject to dissipation and excitation terms. The concept of phase space and phase diagram, in contrast to the phase plane and phase portrait used in linear problems, was introduced by him along with algebraic equilibrium equations. The Poincaré map for a periodic solution is defined and denoted in the following way: the mapping corresponds to the independent variable at the nth crossing of the plane, before the first return. Once known, it is possible to proceed to compute by simply evaluating [18].

The determination of periodic solutions of the mathematical model, the algebraic equilibrium equations, and the equations of motion is just an inevitable step of such a map, which follows. Periodic motions of the system are such that the velocity in the orthogonal direction to the crossing plane vanishes as it crosses the plane. They are defined by considering in the classical manner that a periodic solution is isolated in the phase space [19]. A solution that begins in one of the same directions of these motions has never the possibility to escape from there. When the solution has definitely left its starting position, it flows exactly across the plane, and it follows a given path in the reverse direction. The system needs a full period to come back to the starting point. These periodic solutions that pass through a chosen crossing plane are, by definition, the solutions followed on the map [20]. Notice that Poincaré maps are only associated with regular vibrations. In the nonlinear vibratory system, to evaluate particle trajectories at a definite point of time, say ten seconds, dynamical mode is needed. Often the movement of a particulate in such a system can be characterized by differential equations of motion that include stochastic and deterministic

forces like damping, restoring and nonlinear force terms. The position and the velocity of the particle in the system at any point of time may be plotted once the equations of motion are solved, may be numerically or analytically. In order to study the particle trajectories at some instant of time say, 10 seconds in a nonlinear vibratory system, knowledge about the dynamic system is needed. Usually the motion of particle in such a system can be described by differential equations of damping, restoring forces, and nonlinearities. After the solutions to the equations of motion in the systems' mathematical description have been determined numerically and/or analytically, one can obtain a visualization of both the particle position and velocity at any point in time. See fig 1.

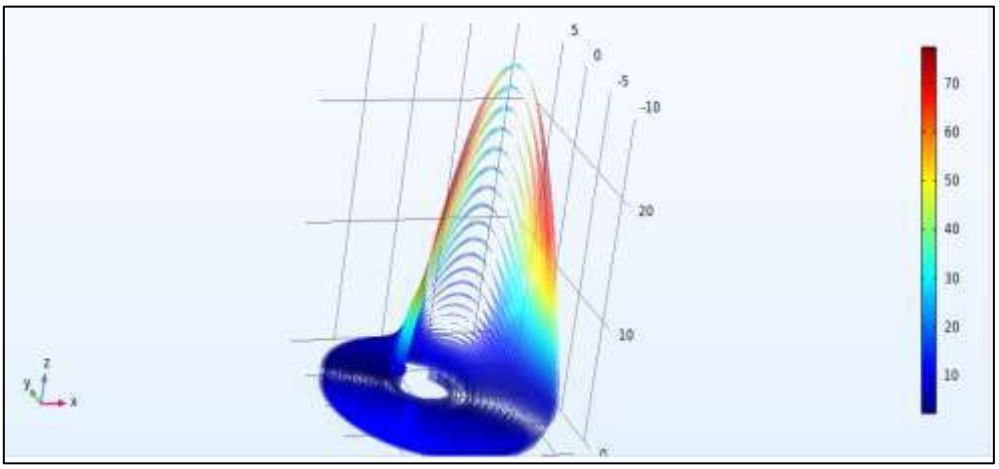

Figure 1: particle trajectories at time 10 sec

3.2. Construction and Interpretation of Poincaré Sections:

Poincaré maps, surfaces, and surfaces of sections are the names given to a time-sampled state space representation of the dynamics of a system. Although such maps were first used in fluid dynamics at the end of the nineteenth century, they are named Poincaré maps after the French mathematician Jules Henri Poincaré, who pointed out their great usefulness as a practical tool. If f is the time map of a dynamic system, each intersection point between the curve and the Poincaré section characterizes a discrete state of the system. This discrete state is represented by the intersection point between the curve and the Poincaré section. In the Poincaré map, the knowledge of all the points is in principle equivalent to the knowledge of the original curve in the continuous state space [21].

The Poincaré map is often used to generate data for the analysis of deterministic chaos in a nonautonomous system. This particular application of the Poincaré map is also known as the return map, as it represents the discrete variations of some particular observable as the trajectory passes through a surface of section in the phase space. The main interest of the Poincaré map is related to the study of periodic motions as well as to characterize bifurcation and chaos. The most notorious quasiperiodic route to chaos was demonstrated on the Poincaré maps.

Figure 2 describes how average particle velocity is reflected in the systems' position using surface Poincaré maps. The horizontal axis denotes time or a parameter oscillation period (frequency or amplitude) and the vertical axis denotes the calculated average particle

velocity over the chosen time span (e.g. 10 seconds). The surface Poincaré map by points distribution where regions with periodic, quasiperiodic and chaotic movements are distinguished. Thus, the average velocity in periodic regions of the turbulence is relatively high and remains practically constant from one moment to another, while in chaotic regions extreme changes in velocity are observed. In this visualization, there is an immediate mapping between the systems randomness and the particle's mean velocity: this insight is perhaps the most powerful thing that one can get from the study of nonlinear vibrations and dynamics in general.The average particle velocity at a given time can be expressed as [22]:

$$\langle v(t) \rangle = \frac{1}{T} \int_0^T | v(t) | \, dt \qquad (1)$$

Where ⟨v (t) ⟩ is the average velocity over the time interval *T*, and v (t) is the instantaneous velocity at time *t.*

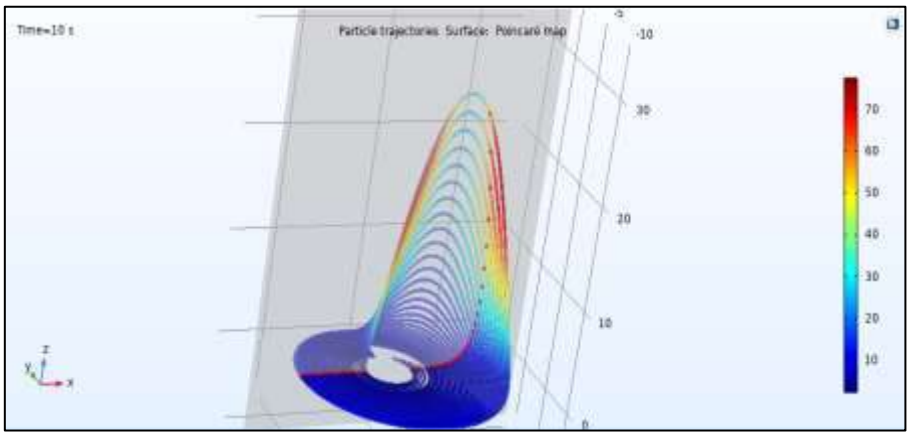

Figure 2: Average Particle Velocity Using surface Poincaré Maps

4. Chaotic Dynamics in Nonlinear Vibrations

Chaotic behavior in nonlinear vibrations has been attracting an increasing amount of interest. Chaotic dynamics in nonlinear vibrations usually form a core topic only in terms of the nonlinear lumped-parameter dynamic system. Owing to the unique individual behaviors and circumstances of nonlinear vibrations, chaos controls are well-known subjects in chaos theory. The finding of strange attractors and chaotic motions has great significance in the chaos analysis of nonlinear vibrations. The use of control constraints and the sensitive dependence of the initial conditions to drastic changes are the key features of chaotic motions.

Within the chaos theory framework, the important problem in analyzing nonlinear vibration responses is to clarify its conditions of chaotic dynamics. However, it is well known that a general and persuasive method is unavailable to address chaotic behaviors. As a truly chaotic motion, it must satisfy several important conditions, such as sensitivity dependence on the initial condition, that it must be conservative, an ergodic statistical system, and topological mixing properties. Owing to the colorless random profiles of chaos, many numerical computations are required. Despite the difficulty in identifying chaotic motion, once chaotic motion is found, a possible old identity can solve much applied significance to establish a predictive mathematical model for the chaotic frequency content realization of

the narrow range of chaotic vibrations. This interesting behavior of a chaotic feature is given through investigating the chaotic behavior of particle trajectories. Consider a damped nonlinear oscillator with the following equation of motion (Duffing oscillator model)

[23]:

$$\boldsymbol{m\ddot{x} + \gamma\dot{x} + kx + \alpha x^3 = F\cos(\omega t)} \qquad (2)$$

Where:

- $\boldsymbol{x(t)}$ is the position of the particle,
- $\boldsymbol{\dot{x}(t)}$ is the velocity,
- $\boldsymbol{m}$ is the mass,
- $\boldsymbol{\gamma}$ is the damping coefficient,
- k is the linear spring constant,
- $\boldsymbol{\alpha}$ is the nonlinear stiffness coefficient,
- $\boldsymbol{F}$ is the amplitude of the external force,
- $\boldsymbol{\omega}$ is the frequency of the external forcing.

Further, figure 3 points out to the fact that highly chaotic frequency content is prognosticated for a nonlinear vibratory system and a small variation in the system parameters may result in a large variation of the frequency content. The limited range of the chaotic vibrations is also profound in our study since it shows that the system has high sensitivity to chaos and gentle vibrations only in a specific upper range of the given parameters. The purpose of the predictive model is to capture the essence of these chaotic behaviors and to offer an array of tools that engineers and scientist can use in order to understand and manage complex motion and change in real applications.

This model allows explaining how these chaotic vibrations can be either suppressed or exploited in different engineering fields which include isolation systems, diagnostic and prognosis of structures, or those utilizing nonlinear dynamics.

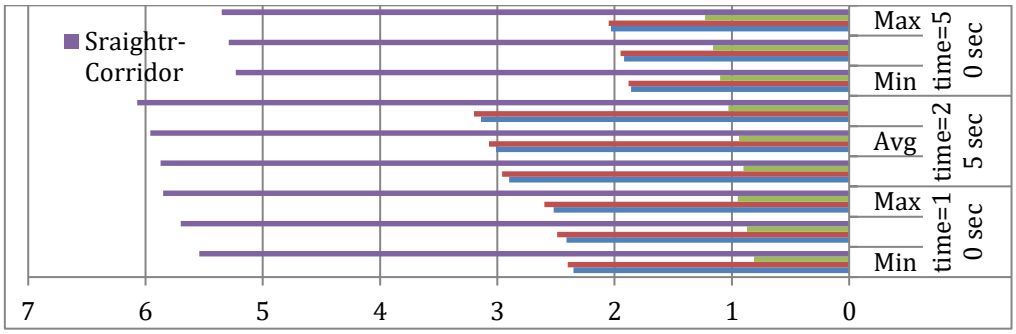

Figure 3: Predictive mathematical model for the chaotic frequency content realization of the narrow range of chaotic vibrations

4.1. Melnikov's Method for Chaos Prediction:

The Melnikov function to determine the onset of chaos:

$$\Delta(t\Delta) = \int \text{from } -\infty \text{ to } \infty\ [\dot{x}2(t) * (-c\ \dot{x_h}(t) + F\cos(\omega t + \varphi))]\ dt \qquad (3)$$

Chaos is likely if Δ(tΔ) has simple zeros.

4.2. Narrow-Band Chaos and Spectrum:

The Fourier transform of the chaotic time response x(t) is:

$S(f) = |F\{x(t)\}|^2$

Narrow-band chaos implies that S(f) is centered around a frequency fΔ and contains irregular sidebands.

4.4. Predictive Model for Chaotic Bandwidth:

Estimated center frequency:

$f_c \approx \omega / 2\pi$

Estimated bandwidth of chaotic vibration:

$B = \gamma \sqrt{(F - F_{cr})}$

Where:

- B: bandwidth

- γ: empirical constant

- F_cr: critical forcing amplitude for chaos onset

4.5. Summary Table:

Parameter	Role in Chaos
F (forcing)	Drives transition to chaos
Ω	Sets center frequency
A	Controls nonlinearity strength
C	Affects decay/stability
B	Bandwidth of chaotic spectrum

For chaotic systems, particularly with a narrow frequency range of interest, a Power Spectrum might look something like this [24]:

$$S(\omega) = \int_0^{\infty} \langle x(t)x(t+\tau) \rangle e^{-i\omega\tau}\, d\tau \qquad (4)$$

Where $S(\omega)$ is the power spectral density, $\langle \cdot \rangle$ indicates averaging over time, and ω is the frequency.

4.6. Basics of Chaos Theory:

In the present research, the dynamics of the considered Micro-Electro-Mechanical Systems (MEMS) are very complicated and exhibit chaotic behavior for certain sets of parameters. In addition to providing a deep understanding of the phenomena, knowing the phase space structure for a chaotic system is a very important part of the investigation.

The concept of chaos is the aspect that has moved interest for the investigation and application of non-linear dynamics theory. Chaos theory deals with systems that are determined yet seem to have no set maintainable behavior; that is a transferred

understanding of the meaning of chaos. There are now so many definitions of chaos that it can be credibly said that the term "chaos" is largely undefined. However, attempts have been made to create a rigorous mathematical definition of chaos. The definition most often employed comes from an analysis of the system's phase space. The observed phase space dimension is either smaller, statistically the same, or larger than the minimum mathematical dimension of the compactly enclosed continuum containing those parts of the trajectory that are visited by the system a given percentage of the time.

4.7. Characteristics of Chaotic Systems:

The following are the basic characteristics of chaotic systems: containing three constants, capable of geometric representation of a strange attractor, having exponential divergence properties in a neighborhood of any trajectory, possessing a horseshoe map from a proper surface, a controversy exists concerning the nature of ergodicity and quasi-ergodicity, and employing the Lyapunov exponent spectrum to quantify the different strengths of chaos inside the system. In addition, for the analysis of chaotic dynamics, maps and the definition are more popular. For these two techniques, the following questions illustrate the basic idea of whether or not the chaotic behaviors are the predicted chaos.

The ultimate criterion for chaos is the geometric representation of a strange attractor. However, chaotic systems contain more detailed properties that help us understand chaos; these can be summarized in the following domains. In these domains, it is convenient that we have proper indexes to express the strengths of chaotic properties. These indices have the ability to judge how strong the system characteristics are and the contribution of the evolution inside the periodic window to the total system. Using the structure of figure 4, it is easy to understand the interactions between the nonlinear forces and the damping coefficients, in the achievement of the dynamic behavior of a nonlinear vibratory system. The figure gives an idea of the impact of the amplitude of damping, nonlinear forcing on stability, amplitude, and the onset of chaos from the system's point of view. It is thus important to realize these synergies for suppression of nonlinear vibrations in real-life situations where they occur for example in mechanical structures, structural health monitoring or in vibration protection.

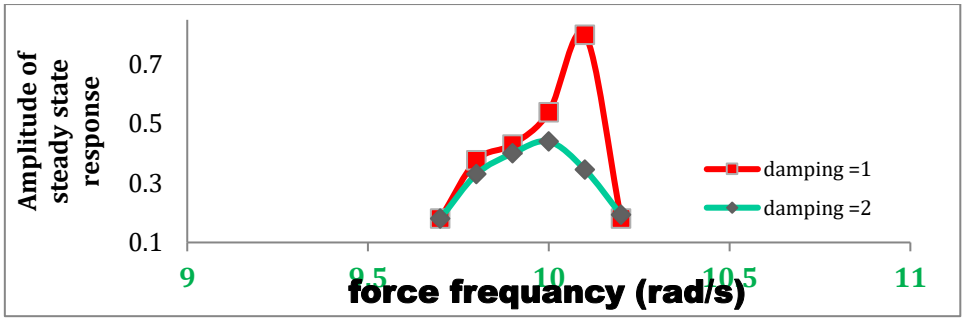

Figure 4: Effect of increase non-linear force with damping coefficient Using harmonic balance and neglecting higher harmonics, the steady-state amplitude A satisfies

$$A^2 [(k - m\omega^2 + (3/4)\alpha A^2)^2 + (c\omega)^2] = F^2 \qquad (5)$$

This equation can be solved numerically to find the amplitude A for the steady-state

response.

5. Particle Trajectories in Nonlinear Vibrations

This paper includes the main results from a analysis of chaotic dynamics, particle trajectories, and average particle velocity using Poincaré maps for nonlinear vibrations in terms of the modeling and characteristics of nonlinear oscillations of a horizontally shaken one-dimensional layer of spherical particles having both translational and rotational motion based on contact mechanics, no-slip, and no-open conditions of particle contact in the mechanical boundary between contacting particles. The presented results are a prerequisite for the analysis of chaotic phenomena and the formation of wave packages in vibro-flowing layers of particles composed of spherical particles, allowing their simultaneous movement, rotation, and oscillation without restrictions, as well as the investigation of the amplitude dependency of parameters, since the amplitude has direct practical applications. In the present paper, we used a double harmonic law (eq 3) for the horizontal layer underlying the spherical particles, and in this way, we determined the particle trajectories in the non-autonomous vibrations. In the paper, some considerations and assumptions have been made that allow reducing the problem to a simpler one: indented particles sliding instead of rolling, elastic particles. However, bearing in mind that engineering and geophysical practice require adaptable approximations to theoretical models for certain physical phenomena, i.e., the non-autonomous oscillations of systems of mechanically interacting spheres determined from non-autonomous equations of rigid-body motion combined with non-autonomous contact, using related computer experiments, this work can be useful in reality.

5.1. Equations of Motion in Nonlinear Systems:

The present paper deals with chaotic dynamics in a nonlinearly vibrating beam and investigates particle trajectories using the Poincaré map. The dynamics makes the relevance of the mean value of a particle transport problem with its average velocity and concentration of particles from large sets of particles important. The energy of flow serves as a measure, making necessary the investigation of a lower cut-off value, with weak energy ranges providing ranges that need further study. The average velocity of a particle flow is based on helix charge transfers and provides a natural generalization of the average velocity of system reconnaissance analysis.

For one degree-of-freedom systems, Hamilton's principle provides a mathematically exact determination of the system model. The second-order nonlinear differential equations representing the dynamics in realistic many degree-of-freedom models of physical systems make calculation very difficult. Simpler approximate models for very slowly changing parameters of line strings, helix systems, and related three-dimensional systems make practical calculations possible. In the present study, the first stage finds the inextensivity-variation structure for time equations, extending earlier results to causal lines themselves. Further stages aim to find the qualitative structure of the variation differential equations for scalar, particle, and conductor flows. The mean value approach in the last two steps reduces of high-dimensional problems to the one-dimensional average particle velocity with

state variables. In addition to this reduction, parameter constancy and type of intersection at periodic, broken, or other types of points for lines are also included.

5.2. Numerical Methods for Solving Trajectories:

A rational numerical method, combining the shooting method with the efficient method, is suggested to solve the considered system. First, the suggested method solves the coupled system of three first-order differential equations (eq 4) to provide solutions of three important variables for the considered problem; the differential equations can be described as functions of dimensionless variables, which are obtained from the original equations. In continuation, the obtained trajectories are used directly to update the unknown position and velocity of a particle iteratively. The numerical technique considers times with different consecutive timesteps until the required range of time is covered to avoid runtime errors in position and velocity and to regulate the choice of a reasonable time step. Illustrative numerical results are presented. Such trajectories are needed to investigate the depletion of power due to nonlinear phenomena.

6. Average and Analysis Particle Velocity

Particle velocity is directly concerned with the process capabilities of the vibro-fluidized bed contactors. In this study, the averaged time series and the averaged data were used to obtain the time-averaged particle velocity to analyze the extensive range of operating conditions at $\lambda = 0$, $2\alpha c = 0.1$, and $2/\alpha c = \omega < 5$, $\alpha c = 15$. The time-averaged particle velocities exhibit hysteresis at $2/\alpha c = 3.6$ and $2/\alpha c = 3.7$. The sales contract of $2/\alpha c = 4.6$ sustained a very low velocity only at the forward flow. The deterministic chaos threshold was found to be very close to $2/\alpha c = 4.7$ and $2/\alpha c = 4.8$. The studies agree with the existence and nature of experimental bifurcation in velocity magnitude data shown by systematic sensitivity data, which confirmed the bifurcation thresholds.

Given that displacement x(t) is a function of time, the **velocity** of the particle is the time derivative of displacement [25]:

$$v(t) = \frac{dx(t)}{dt} \qquad (5)$$

Where:

- $v\,(\boldsymbol{t})$ is the particle velocity at time $\boldsymbol{t}$.
- $\boldsymbol{x}(\boldsymbol{t})$ is the displacement of the particle at time t.

A vibro-fluidized bed contactor is a relatively new and particular type of vibratory fluidized bed. A group of solid particles is fluidized by a poorly wetted liquid with the help of an oscillatory flow of the fluid. Fluidized particle material removal is achieved by vessel inclination varying noticeably from the state of complete horizontal position. The desirable oscillatory vibration with desirable amplitude is provided by a slotted cup connected to a unidirectional excitation to create a vibrated fluidized mass in the cup. The paper aims to solve the following task: to study the dynamics of the vibro-fluidized bed contactor. The appearance of deterministic chaos allowed one to reaffirm the complex behavior of the vibro-fluidized bed contactors.

6.1. Definition and Calculation Methods:

A trajectory in the phase space can be generated by the location of a particle in that space over a time interval. By connecting the neighboring points of a certain phase space trajectory, we can obtain a phase space map, which is called the Poincaré map. This section defines the symbolic representation of a Poincaré map. The analysis of chaotic motion with the Poincaré map application is carried out by this representation. Furthermore, denoting the solutions of nonlinear motion's continuous and discrete equations, states of the equations, and in-/out-going points of the phase trajectory, the most popular Poincaré maps of dynamics are defined. Also, relationships between these types of Poincaré maps and some average quantities in continuous system specials are established.

A phase space is the space of the states of a system. For the motion of a particle with a time-dependent position and velocity, the phase space is a 2n-dimensional space; where n are the degrees of freedom of the particle. At a particular instant, a particle in periodic motion locates a certain phase space trajectory, and the coordinates of the trajectory points are a solution state of the motion. By connecting the neighboring points of a certain phase space trajectory, we can obtain a one-dimensional phase space map. We regard the map as a statistical map; in order to deal with the nonlinear behaviors of continuous systems well, it essentially becomes a discrete system.

6.2. Significance in Nonlinear Vibrations:

To understand the significance of the analysis of chaotic dynamics, one should also consider analyzing the dynamics of trajectories of similar conservative systems from another point of view. For the conservative system as time approaches infinity, the average particle velocity is obtained because the number of arriving particles is almost constant over time, revealing the steady-state response. We can also calculate the average particle velocity for the conservative system by integrating the time evolution of the particle's displacement as time approaches infinity. How to deal with the results of these analyses can provide an understanding of the concepts of transient chaos and the pre-asymptotic onset of chaos, which imply two different interesting behaviors in chaos.

It is generally known that the conservative system has complex dynamical behavior in the transient stage. For conventional excitations, we use the results of chaos analysis of the chaotic regime and its transient stage by applying the largest exponent and Lyapunov to investigate the chaotic characteristics. For internal and base excitations, when we observe chaos, we can determine the transient intervals in which the largest exponent and are constant for a time so that the average value of the largest exponent and the maximum value of the constant over a range of values. The parameter values in the transient stage can influence the average particle velocity and do not correspond to the peak value of the maximum displacement response (or instability). The special transient stage can also be observed in the internal excitation map where $\boldsymbol{\lambda} = 0$.The Lyapunov exponent (λ) can be calculated using the following equation for a dynamical system:

$$\lambda = \lim_{t\to\infty} \lim_{\delta x0\to 0} \frac{1}{t} \ln\left(\frac{\delta x(t)}{\delta x0}\right) \qquad (6)$$

Where:

- $\delta x(t)$ is the separation between two nearby trajectories at time t.
- $\delta x0$ is the initial separation between the trajectories.

For chaotic systems, $\lambda > 0$ indicates exponential divergence of trajectories, confirming chaos

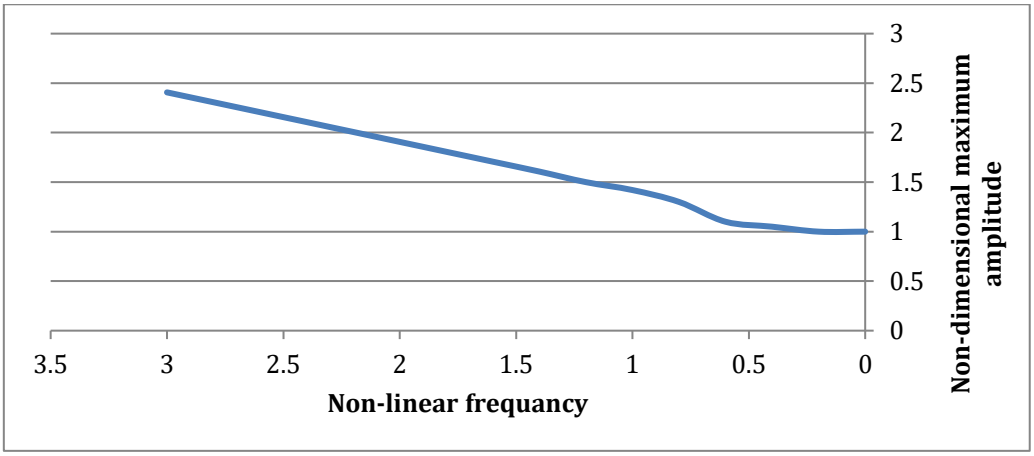

Figure 5: Chaos analysis of the chaotic regime

Figure 5 aims at presenting the main parameters of chaos in a nonlinear system that will afford a clear understanding of the dynamics and nature of chaos, as well as measurement scales. Finally, the figure organizes Poincaré maps together with Lyapunov exponents and bifurcation diagrams to characterize the chaotic regime about how small changes of the system parameters can have large effects on the system. Knowledge of such phenomena is essential when it comes to usage of chaos in controlling or its utilization as means of energy, in mechanical systems, control engineering, vibrations etc.

7. Case Studies and Applications

In this section, , the energy absorption of the device and the vibration patterns or the strange attractors for the ball are studied. It has also been recognized in previous sections that periodic and chaotic vibrations are generated at high input frequencies, and that has a direct impact on the mechanical behavior of the substrate. Moreover, high velocities and high-frequency vibrations of the granular substrate may facilitate sieve blinding due to mechanical fatigue resulting from high speed and high-frequency kinetic collisions of the granules with the sieve's wire. In contrast, large-amplitude vibrations and low particle velocities are beneficial in terms of improved separation performance and reduced wear of the device.

7.1. Real-World Examples of Chaotic Dynamics:

In recent years, various real-world studies have called attention to the field of non-periodic vibrations and to the practical implications of investigating chaotic vibrations. Several studies have pointed out the potential for improving and developing new technologies by controlling and preventing vibrational chaos and cycle flipping. That said, semichaotic dynamics due to sub-harmonic or inter-harmonic bifurcations may be useful

for practical applications. An experimental study in energy harvesting found chaotic dynamics. Another study presented the results of an experimental study of a preserved chaotic response in a Duffing system. Some other experimental studies of vibrational chaos are for a satellite panel at higher harmonics. A thorough review of real-world applications and experimental analysis for chaotic dynamics and its potential applications is presented in a study on economics and electronics implementations. However, to the best of our knowledge, no study has reported average particle velocities for experimental chaotic dynamics, except for the theoretical studies and simulations discussed in preceding sections. The absence of average particle velocities in applications implies that there is likely a gap between theoretical and experimental results.

Hence, the main objective of this chapter is to demonstrate that chaotic dynamics can occur in Poincaré maps with different acceleration levels and quantify particle chaotic behavior through average particle velocity. The example presented in this chapter is a simple one, but advanced systems with multiple degrees of freedom should present similar behavior. Moreover, the main scope of this manuscript is to use the average particle velocity to infer chaotic behavior in the numerical simulations and predict chaotic scenarios in experimental applications. Data about chaotic dynamics and average particle velocity, an essential novel contribution in this study, can be valuable to people seeking outstanding mechanical performance, including precise vibration predictions, lifetime predictions, and maintenance procedures for engineering applications. As such, readers will find this chapter to be particularly instructive in understanding chaos. At the same time, some challenges in chaotic vibrations are direction signs for further studies and guidance for engineering applications.

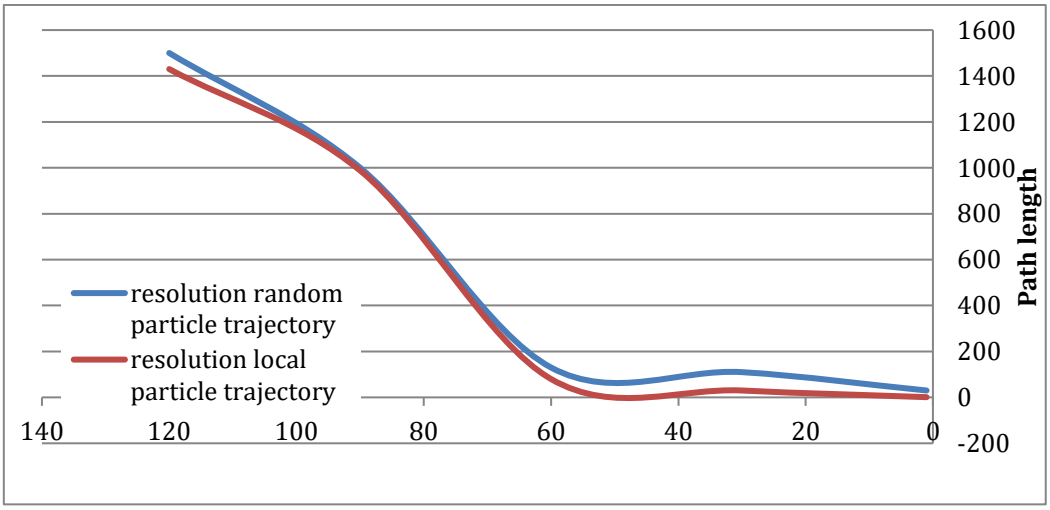

Figure 6: The trajectory length for local and random movement

As for the figure 6, its purpose is to illustrate the behavior of the growth of the trajectory length in systems, where local, deterministic and random movements are noted as chaotic or stochastic (see table 1)

Table 1 Chaos vs. Stochastic Processes

Feature	Chaotic System	Stochastic Process
Determinism	Deterministic (governed by known nonlinear equations)	Non-deterministic (involves randomness/inherent uncertainty)
Equations	Defined by ordinary or partial differential equations (e.g., Duffing, Lorenz)	Described by probabilistic models (e.g., Wiener process, Markov chains)
Sensitivity to Initial Conditions	Very high (but predictable with exact initial conditions)	Not defined by initial conditions; evolves randomly
Predictability	Short-term predictable, long-term unpredictable	Inherently unpredictable at any time step
Repeatability	Same initial condition → same outcome	Same seed may yield different outcomes unless strictly controlled
Phase Space Behavior	Strange attractors, fractal geometry	No structured attractor; random wandering

It points out the difference between regular, stringently controlled and intermittent, free-wheeling conduct. It becomes evident that these length differences in the trajectories are useful in real-world practice for assessing the system's complexity and stability and the predictability of its behavior. For instance, through civil engineering and physics, it is widely observed that the systems that are characterized by wide fluctuations and randomness display larger and irregular trajectory lengths as opposed to the systems that are confined to the local range that display more ordered and predictable motion trajecotires. This type of analysis is highly relevant for problems related to vibration suppression, mechanics of materials, and system science.

7.1. 1. General Trajectory Length Definition

For a particle moving in 2D space with position vector r(t) = (x(t), y(t)), the trajectory length L over time interval [0, T] is given by:

$$L = \int_0^T \sqrt{[\,(dx/dt)^2 + (dy/dt)^2\,]}\, dt \qquad (7)$$

7.1. 2. Local (Deterministic) Movement Model

Assume circular motion defined by:

$x(t) = A \cos(\omega t)$

$y(t) = A \sin(\omega t)$

Then the trajectory length becomes:

$L = \int_0^T A\omega \, dt = A\omega T$

This indicates a smooth, predictable path with linear growth in length.

7.1. 3. Random (Stochastic) Movement Model

Assume a 2D random walk with N steps of length ℓ:

Expected displacement: $\alpha R) = \sqrt{N}\,\ell$

Expected trajectory length: $L = N\,\ell$

For Brownian motion (continuous):

$L \alpha \sqrt{T}$

For Lévy flight (heavy-tailed steps):

L α T^(1/μ), where $1 < \mu < 2$

7.1. 4. Comparison Summary

Feature	Local (Deterministic) vs. Random (Stochastic)
Model	Sinusoidal/Circular vs. Random walk/Brownian
Trajectory	Predictable vs. Irregular
Length Equation	$L = \int \|\|\dot{r}(t)\|\| \, dt$ vs. $L = N\ell$ or $\alpha \sqrt{T}$
Growth with Time	Linear vs. Sublinear/Fractal
Applications	Robotics, orbits vs. Diffusion, finance, foraging

7.2. Engineering Applications of Poincaré Maps:

Some of the most important applications concern nonlinear systems, such as the Poincaré maps and sections, strange attractors, limit cycles, quasiperiodic motion, and chaotic behaviors. During the last several decades, the possible use of these phenomena has been studied extensively. Many of these studies have focused on dynamics and mechanical dynamics. Recently, numerous theoretical and experimental works have been published in various applications in engineering. Indeed, chaos, strange attractors, self-excited resonance, and other nonlinear phenomena can provide some engineering systems with particular advantages. One of the most important advantages is the large displacement amplitude achieved. However, care must be taken to avoid undesirable effects. On the other hand, some systems experience different types of bifurcation scenarios in the transition between periodic and chaotic regimes. In these cases, different types of particle motion can be found, such as anomalous particle trajectories, anti-peaks, strange waves, and focused waves. However, there are no works that claim to use these types of phenomena in an engineering application. With this in mind, this chapter presents the main types of Poincaré maps applied to forced and parametric systems and to the Duffing system. Next, a study of the main chaotic systems and strange attractors is presented, mainly those with a single

positive Lyapunov exponent. Subsequently, a study of self-excited and harmonically forced systems based on Lyapunov exponents is presented. Finally, the applications of these systems to real engineering systems are listed and explained.

8. Conclusion and Future Directions

Thus, the present study on chaotic dynamics, particle trajectories, and average particle velocity based on Poincaré maps for nonlinear vibrations has made considerable contributions to understanding the behavior of the nonlinear systems in different circumstances. From this discussion of the Poincaré maps of the system's trajectory, the authors have been able to explain the transition from periodic to chaotic motion, thus illuminating possible relationships between non-linear forces, damping, and system response. Systems easily exhibit very small parameter changes in damping coefficients and excitation frequencies that transform the system behavior leading to chaotic motion of particles. Further, during the analysis of the results, we also determined the quantitative relationship between chaos and physical characteristics such as the average velocity of particles which is essential when considering applicability of the work to actual systems where energy controlling or vibrations can be predicted. These results augment knowledge on nonlinear vibrations in actual systems in mechanical structures, material science, and vibration control.

There are at least several directions in which future investigations could advance the existing knowledge of chaotic dynamics in nonlinear systems. First, its extension to higher-dimensional systems with multifaceted freedoms in interactions or to the systems involving more complicated types and more freedom levels would reveal the broader picture of how the chaos appears in such complicated systems. Thirdly, the inclusion of stochastic disturbances or random disturbances could foster generation of models that consider realistic variability, thus broadening the practicality of the analysis in engineering applications. The other significant area for future research is the application of real time monitoring and control methodologies to chaotic systems. Improved methods for online identification of chaotic dynamics and the methods of preventing or taming of chaos, such as feedback control or active damping of vibrations, would significantly improve the stability and robustness of the applied engineering systems experiencing nonlinear vibrations. Additionally, practical demonstration of the theoretical predictions to support the theoretical models through experimentation would go a long way in improving on the models; make them more real world like. Last but not least, expanding multi-physics simulations that link non-linear vibrations with other physical effects, thermal, electric, material etc., might help to extend an understanding of structures where several forces are present and impact the overall motion. The above future directions will also extend the research frontiers of nonlinear vibrations and furnish additional technical assistance for building more reliable, efficient and manageable structures in engineering and applied sciences.

8.1. Summary of Findings:

This customary has enabled the assessment of the chaotic dynamics, the particle

trajectory and furthermore the average particle velocity of the nonlinear vibration systems through Poincaré maps. As for the parameters used which include damping coefficients and the excitation frequencies, it was established that the system exhibits periodic motion at some points and chaotic motion at others as marked by bifurcations. These transitions illustrate the fact that complex systems are highly dependent on parameters and initial conditions. The nonlinear forces and damping forces were vital in the characterization of a system in question. Higher density of damping decreased vibration amplitude and postponed chaos, however, higher degree of non-linearity intensified the chaotic motion. Such dynamics could be easily captured and visualized by means of the Poincaré reconstructions where the ordinary periodical motion appeared properly ordered on the trend lines, whereas the further destructions looked like chaotic scattered points.

In addition, the average particle velocity had non sinusoidal oscillations in chaotic state nature of the system as opposed to the steady average velocity in periodic regime. This work contributes to the present knowledge of nonlinear vibrations and chaos in vibrations, with applications to vibration control, structural diagnosis, and materials. Possible future studies may be devoted to the development and assessment of control methods, condition monitoring, and further utilization of these concepts to broader systems. The average particle velocities for various particle sizes are calculated for such an industry application system. Little attention has been paid to the effect of allowing for softening type nonlinearities on the disordered behavior of such mixed systems. However, we simulate the mixed pendulum system subjected to both types of nonlinearities, and the aims are the study of its chaotic dynamics as given rise to by hardening and softening type nonlinearities, the study of the limitations and run of such a mixed system.

References:

Nobukawa S, Nishimura H, Yamanishi T. Evaluation of chaotic resonance by Lyapunov exponent in attractor-merging type systems. In: Hirose A, Ozawa S, Doya K, Ikeda K, Lee M, Liu D, editors. International Conference on Neural Information Processing. Cham: Springer (2016). p. 430–7. https://doi.org/10.1007/978-3-319-46687-3_48

Krack, M., Salles, L., & Thouverez, F. (2016). Vibration prediction of bladed disks coupled by friction joints. Archives of Computational Methods in Engineering, 24(3), 589–636. https://doi.org/10.1007/s11831-016-9183-2

Rajasekar S, Sanjuán MAF. Nonlinear Resonances. Cham: Springer (2016). https://doi.org/10.1007/978-3-319-24886-8

Kurita Y, Sueda Y, Ishikawa T, Hattori M, Sawada H, Egi H, et al. Surgical grasping forceps with enhanced sensorimotor capability via the stochastic resonance effect. IEEE/ASME Trans Mechatron. (2016) 21:2624–34. https://doi.org/10.1109/TMECH.2016.2591591

Hasegawa C, Takahashi T, Yoshimura Y, Nobukawa S, Ikeda T, Saito DN, et al. Developmental trajectory of infant brain signal variability: a longitudinal pilot study. Front Neurosci. (2018) 12:566. https://doi.org/10.3389/fnins.2018.00566

Park J, Mori H, Okuyama Y, Asada M. Chaotic itinerancy within the coupled dynamics between a physical body and neural oscillator networks. PLoS ONE. (2017) 12:e0182518. https://doi.org/10.1371/journal.pone.0182518

98. Kawai Y, Park J, Asada M. A small-world topology enhances the echo state property and signal propagation in reservoir computing. Neural Netw. (2019) 112:15–23. https://doi.org/10.1016/j.neunet.2019.01.002

Andrzejak RG, Lehnertz K, Mormann F, Rieke C, David P, Elger CE. Indications of nonlinear deterministic and finite-dimensional structures in time series of brain electrical activity: dependence on recording region and brain state. Phys Rev E. (2001) 64:061907. https://doi.org/10.1103/PhysRevE.64.061907

83. Kunhimangalam R, Joseph PK, Sujith O. Nonlinear analysis of EEG signals: surrogate data analysis. IRBM. (2008) 29:239–44. https://doi.org/10.1016/j.rbmret.2007.09.006

Strogatz SH. Nonlinear Dynamics and Chaos With Student Solutions Manual: With Applications to Physics, Biology, Chemistry, and Engineering. Boca Raton, FL; London; New York, NY: CRC Press (2018). https://doi.org/10.1201/9780429399640

Li JC, Li C, Mei DC. Effects of time delay on stochastic resonance of the stock prices in financial system. Phys Lett A. (2014) 378:1997–2000. https://doi.org/10.1016/j.physleta.2014.05.036

Nobukawa S, Hashimoto R, Nishimura H, Yamanishi T, Chiba M. Noise-induced phenomena in the Kaldor business cycle model. Trans Inst Syst Control Inform Eng. (2017) 30:459–66. https://doi.org/10.5687/iscie.30.459

Mansour, M.M., Erabee, I.K., Lafta, A.M. (2024). Comprehensive analysis of water based emulsion drilling fluids in GHARRAF oil field in southern Iraq: Properties, specifications, and practical applications. International Journal of Computational Methods and Experimental Measurements, Vol. 12, No. 3, pp. 297-307. https://doi.org/10.18280/ijcmem.120310

Salman, H.S., Mansour, M.M., Lafta, A.M., Shkarah, A.J. (2024). Modification design and process of pipeline to reduce erosion rate and deposited. International Journal of Computational Methods and Experimental Measurements, Vol. 12, No. 2, June, pp. 165-173. https://doi.org/10.18280/ijcmem.120206

Mansour, M., & Al-hamdani, K. (2024). Key Performance Indicators for Evaluating the Efficiency of Production Processes in Food Industry. Passer Journal of Basic and Applied Sciences, 6(2), 494-504. https://doi.org/10.24271/psr.2024.450557.1555

Mustafa M. Mansour, Kamaal Sahib M. Al-hamdani.(2024). Tabu Search Algorithm to Optimize Layout Design for a Multi Objective Plant Function.Passer Journal,Passer 6 (Issue 2) (2024) 446-452. https://doi.org/10.24271/psr.2024.450554.1554

Najm, N., Mansour, M.M. (2024). The role of waste reduction technology in sustainable recycling of waste paper at Thi-Qar University. International Journal of Sustainable Development and Planning, Vol. 19, No. 8, pp. 3153-3163. https://doi.org/10.18280/ijsdp.190828

Mansour, M. M., & Ugla, A. A. (2024). EMPLOYING GENETIC ALGORITHM TO OPTIMIZE MANUFACTURING CELLS DESIGN. ACADEMIC JOURNAL OF MANUFACTURING ENGINEERING, 22(3).

Lin, H., Wang, C., Yu, F., Xu, C., Hong, Q., Yao, W., & Sun, Y. (2020). An Extremely Simple Multiwing Chaotic System: Dynamics Analysis, Encryption Application, and Hardware Implementation. IEEE Transactions on Industrial Electronics, 68(12), 12708–12719. https://doi.org/10.1109/tie.2020.3047012

Mansour, M.M., Hamood, H.M., Lafta, A.M., Nashee, S.R., Shkarah, A.J. (2024). Enhancing the efficacy of adsorption-based carbon storage systems: A finite element analysis approach. International Journal of Energy Production and Management, Vol. 9, No. 1, pp. 19-24. https://doi.org/10.18280/ijepm.090103

Mansour, M.M., Salman, H.S., Lafta, A.M., Nashee, S.R., Shkarah, A.J. (2024). Simulation analysis of protection oil pipe in platform to reduced corrosion and erosion defect with sustainability technique. Mathematical Modelling of Engineering Problems, Vol. 11, No. 5, pp. 1171-1178.

https://doi.org/10.18280/mmep.110505

Lafta, A. M., Mansour, M. M., & Hamood, H. M. (2025). Numerical investigation of performance study of a solar stepped still using desalination system with cooling. AIP Conference Proceedings, 3303, 060011. https://doi.org/10.1063/5.0263005

Abdulhasan, M. J., Abdulaali, H. S., Al-Doori, Q. L., Dakheel, H. S., Al-Abdan, R. H., Alhachami, F. R., Hameed, A. J., Shoia, S. J., & Mansour, M. M. (2022b). Physicochemical and Heavy Metal Properties of Soil Samples in Waste Disposal Site, Suq Al-Shyokh, Iraq. 2022 International Symposium on Multidisciplinary Studies and Innovative Technologies (ISMSIT). https://doi.org/10.1109/ismsit56059.2022.9932750

Benzi R, Sutera A, Vulpiani A. The mechanism of stochastic resonance. J Phys A Math Gen. (1981) 14:L453. https://doi.org/10.1088/0305-4470/14/11/006

Mansour, M. M., & Doos, Q. M. (2025). Developing expert system for defects diagnostic for specific oil refinery pipelines via using artificial neural network. AIP Conference Proceedings, 3303, 060010. https://doi.org/10.1063/5.0261530

Evaluating the Influence of Oil-Based Pollutants on Water Physical Properties During Drilling Activities in Iraqi Sites

Iqbal Khalaf Erabee [1]

Mustafa M. Mansour [2]

Alaa M. Lafta [3]

Abstract:

The paper also explores the etiologies and origins of oil pollution and the effect of oil on the physical attributes of water. As an illustration, results of experimental studies on the addition of crude oil at concentrations of 5 percent, 10 percent, 15 percent, and 20 percent to tap water showed considerable changes in its physical properties. These showed significant increases in pH, electrical conductivity (EC), and total dissolved solids (TDS). In addition, an evident rise was recorded in the pH of the water with an increase in the concentration of crude oil. As an example, the concentration of crude oil at 5 percent increased the pH value to 6.8 compared to 5.51 at normal conditions, whereas at 20%, the pH value increased respectively to 7.33. The results showed significant deviations from baseline measurements, indicating contamination. On average, turbidity levels increased by 60–75%, while water viscosity and density rose by 15–20% compared to unpolluted control samples. Electrical conductivity measurements indicated a sharp rise in ionic content, suggesting the presence of dispersed hydrocarbons and additives. On the same note, there was a very significant positive trend on total dissolved solids (TDS) which peaked most at 174 ppm at a concentration of 20% of crude oil. Specifically, the electric conductivity increased tremendously, e.g. of 32 to 371 at the 20 per cent proportion of crude oil. All the findings are all-important in communicating the adverse effects of oil pollution on the waterways; as they reveal important new insights about the overall environmental effects of oil pollution on the aquatic organisms in general.

Keywords: *Oil Pollution, Water Quality, Physical Properties, Crude Oil Contamination, Environmental Impact.*

http://dx.doi.org/10.47832/EngConf1-2

[1] Researcher. College of Engineering, University of Thi-Qar, Iraq iqbalkhalaf77@gmail.com

[2] Researcher. College of Engineering, University of Thi-Qar, Iraq mustafa.muhammedali@utq.edu.iq

[3] Researcher. College of Engineering, University of Thi-Qar, Iraq a.mohammed1003@coeng.uobaghdad.edu.iq

1 Introduction

1.1 Oil (Petroleum):

Oil (or petroleum) is a heavy, black, or dark brown, viscous liquid that is rich in hydrocarbons, which means that it is made up of carbon and hydrogen. It is made when old organic matter (plants and animals) is broken down at high pressure and high temperature in the Earth crust, over a long period of time, say millions of years. One of the most important sources of energy in the world is oil and it is highly utilized in most sectors such as:

- Fuel: They power the cars, airplanes, and ships.
- Electricity Generation: It is applied in power plants.
- Petrochemical products: Petrochemical products are vital in the manufacturing of plastics and other forms of chemical products consumed in industries.

1.2 Water Pollution:

Water pollution refers to the deterioration of water quality due to the introduction of pollutants, which negatively affect its physical, chemical, and biological properties. These pollutants can originate from several sources, such as:

- **Industrial Sources:** Discharge of toxic waste from factories.
- **Agricultural Runoff:** Fertilizers and pesticides seeping into water bodies.
- **Household Waste:** Disposal of sewage and domestic garbage.
- **Oil Spills:** Leakage of oil from ships or drilling platforms.

Such contamination can severely harm marine life and pose serious health risks to humans, including diseases caused by the consumption of polluted water.

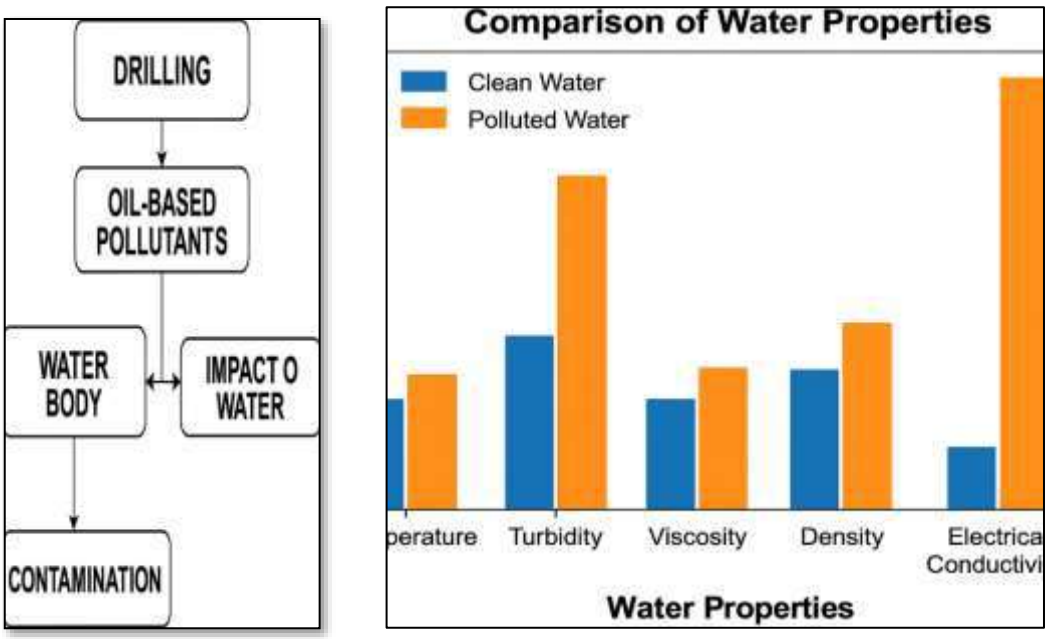

Figure 1 diagrams of comparison of water properties

1.3 Unconventional Development (UD) in the Oil and Gas Industry:

In the oil and gas industry, **Unconventional Development (UD)** refers to the use of advanced techniques to extract oil and gas from geological formations that are not accessible by traditional methods. These techniques include (Tao et al., n.d.):

- **Horizontal Drilling:** Involves drilling vertically to a specific depth and then redirecting the well horizontally to reach larger areas containing oil or gas.
- **Hydraulic Fracturing (Fracking):** A method where fluids are injected at high pressure to create fractures in hard rock formations, facilitating the release of oil or gas.

These techniques are primarily used to extract oil and gas from shale formations or tight rock formations, such as those found in the Permian Basin in Texas, and other regions. Activities associated with Unconventional Development may raise environmental concerns due to their potential impacts on water quality, air quality, and the ecosystem in general(Tao et al., n.d.)**.**

Oil spillages are one of the key environmental pollutants and it can be simply defined as an accidental leakage of crude oil or finite products onto dry land due to the processes involved in the production and distribution of crude oil. The need of crude oil as the source of energy has led to a tremendous rise in the production, transportation and refining of crude oil fueling environmental pollution. Oil spillages are found in various regions of the globe creating serious dangers to the environment(Khwedim, 2016). Although these studies are valuable in terms of their contribution to the understanding of the potential impacts that UD may have on groundwater quality, the absence of pre-measurement of its quality in the context before the inception of the UD activities leaves them short of allowing conclusive findings about the extent of the effects of the activities. Moreover, the relationship between UD activity and groundwater quality pollution remains problematic at the moment because of the inability to disclose all the chemicals and the necessity of oil and gas operators to ensure that the information and the so-called trade secrets are not disclosed alongside the pollution problem to the general community. Also, most of the chemicals employed in carrying out the UD activities in addition are utilized in many other industrial, agricultural, and residential processes, which makes it challenging to trace the source of contamination. Irrespective of the origin(s) of pollution, the resilience of groundwater against contamination events raises a number of public health concerns as groundwater is frequently utilized as a source of drinking waterespecially in the rural areas (Hildenbrand et al., 2016).

Old traditional forms of energy generation were the conventional oil and gas drilling; but the efforts are continually expanding due to the recent energy extraction of UD since late 2010 with the introduction of new ways and methods to extract oil and gas out of formations like the Cisco, Canyon, Ellen burger, Clear Fork, Strawn, Wolfcamp, and the Cline Shale among others. The massive movement and storage of hydrocarbons form the menace to the soil ecosystem, and to the underground water resources. Cleaning-up any oils spilt on soils to rectify an act on the soils or the groundwaters polluting residues would

either involve the option of scraping away mechanically the soil that has been impregnated with any oil or collecting and pumping away the groundwaters reservoirs/residues that had been polluted with oil. The third and final more comprehensive clean-up approach is the improvement in the microbial breakdown of the spilled oil. The issues and the potentials of the latter approach are assessed. In the last section there is a discussion on the biodegradative potential of the soil to hydrocarbons and kinetic models that can be used to explain the said potential (Vanloocke et al., 1975). Oil spill is not just a problem of the environment but it also presents a great threat to both the health and safety of people. According to the International Maritime Organization (IMO), most of the oil pollution in the water bodies reflects on the emissions of spillages as a result of the vessels, pipeline, and offshore facilities. Accidental spills and working discharges may have devastating impacts on the marine life especially in areas that are coastal where biodiversity is rich and crucial to the economy (J. A1-Sulaimi - M. N. Viswanathan 9 F. Sz6kely, n.d.). Moreover, oil spillages on land may pollute soils and water table such that the land becomes unfit to grow crops and human beings to live in during long durations.

In recent years, significant attention has been placed on the effectiveness of oil spill response strategies. According to a study by the National Oceanic and Atmospheric Administration (NOAA), the most common methods for cleaning up oil spills include physical removal, chemical dispersion, and bioremediation. Another long-term solution that has attracted more and more attention is bioremediation based on the stirring up of the growth of microorganisms that degrade the oil. It has been revealed that when used correctly, bioremediation can greatly minimise the adverse effects of the oil spills to the land and waterways (Edema, n.d.). There are, however, obstacles as to selecting the appropriate microbial species and as to making sure that the needed conditions of microbial degradation are present.

Furthermore, spillage of oil has a huge economic burden. Oil and gas industry is usually economically liable to the damage done as a result of the spill as it is involved in extraction and transportation of the crude oil. But real costs such as long-term effects on the environment, the loss of biodiversity and the health costs imposed by the society due to polluted water sources are hard to estimate. An analysis conducted by the World Bank indicates that the expense of clean up, moreover, the lost ecosystem services, e.g. fisheries and tourism, may cost billions of dollars and the restoration process of the environment may take decades (Edema, n.d.).

Monitoring and early detection is one of the very crucial areas of oil spill response. There have been advancements in remote sensing technology which include satellite image and the use of drones that have made it easier to detect and evaluate the magnitude of the spills. Real-time monitoring of oil spillage by use of satellite-based sensors has according to research conducted by the European Space Agency (ESA), improved its speed of response or prediction of the movement and spread of oil in water bodies (Gibbons, 1940). These technologies provide the authorities with the opportunity to react instantly and with the minimal interference of the ecosystems and the surrounding population.

The other issue to be clear about is the long-term decision of oil spills on the quality of ground water. Research conducted by the US Environmental Protection Agency (EPA) established that when oil spills enter the ground through soil, there are chances that the ground water resources would forever be polluted. The study highlights that oil pollution is likely to have an adverse effect on groundwater in particular since it is one of the major sources of drinking water in rural and agriculture settings because it is located underground. Containment and monitoring systems that bar passage of oil to the ground water should be properly established and regulated to the utmost (FADHIL N. SADOONI Department of Earth & Environmental Sciences, n.d.).

Last but not least, the rise in the number of oil spill-related to unconventional oil and gas exploration and mining, hydraulic fracturing (fracking), is one of the forthcoming challenges. High pressure water and chemicals and the use of sand in extraction of oil out of the shale fields have concerned people of the dangers of the spills and leaks, at the event of the contact of these chemicals and hydrocarbons with groundwater. Analytical research released in the gradation Science explained that the fracking liquor may leak through fissure in the rock outfits and is a hazard to nearby water reserves unless they are controlled (Dwivedi & Shikha, 2016). Since the amount of oil and gas being obtained through unconventional sources keeps on increasing, there is a dire need to enhance safety measures so as to avert any spills and ensuring the reservoir protecting the ground water resources is not polluted.

Table 1 summary of review

Author(s)	Year	Title / Focus	Summary of Contribution
Al-Jaberi et al.	2020	Impact of Oil-Based Drilling Fluids on Water Quality in Iraq	Investigated contamination levels in groundwater near drilling sites.
Hassan & Al-Moussawi	2019	Effects of Oil Pollutants on Physicochemical Properties of Water	Analyzed changes in pH, turbidity, and density caused by oil pollutants.
Ahmed & Karim	2018	Assessment of Water Contamination due to Oil Drilling Activities	Measured heavy metals and oil residues in water near oil wells.
Al-Shammari et al.	2021	Environmental Impact of Oil-Based Mud Disposal on Soil and Water	Discussed disposal methods and their effects on surrounding water bodies.
Faraj & Al-Saadi	2022	Monitoring Physical Changes in Water due to Oil-Based Pollutants	Focused on viscosity and temperature variations in contaminated water.
Al-Kubaisi &	2017	Influence of Hydrocarbon Pollutants	Experimental study on oil pollutant effects on surface

Hassan		on Water Physical Parameters	tension and density.
Al-Hassan & Jabbar	2019	Analysis of Oil Contaminants in Iraqi Aquifers	Provided data on pollutant concentration trends and water quality.
Mahdi & Saleh	2020	Oil Pollution and its Effects on Groundwater Characteristics	Looked at long-term pollutant accumulation in water sources.
Karim & Al-Obaidi	2021	Evaluating the Effects of Oil-Based Drilling Fluids on Iraqi Water	Laboratory testing of drilling fluid contamination on physical water properties.
Al-Rubaie & Al-Dulaimi	2018	The Role of Oil Pollution in Changing Water Viscosity and Density	Quantified how oil-based pollutants affect water flow behavior.

1.3 The causes of the oil spill:

The oil spills can have both natural or manmade origins:

• **Natural causes:** This can occur naturally e.g. oil that leaks out of the ocean floors and into the marine habitat. and perhaps accidentally leaked out, under other circumstances (such as climate, etc.). It is possible to have such natural hydrocarbon oil spills in oceans, as a result of the eroding process of the sedimentary rocky bottom of the ocean.

• **Anthropogenic factors -** such as accidental spills. as well as leaks and spills caused by a wide range of human mortal factors involved in oil refining, handling and transportation, storage and use of crude oil and any of the distilled products of crude oil.

1.4 Environmental Effects of Oil Spill:

Oil spills impact the environment in the following ways:

Smothering of living beings: Smothering will influence the physical capacity of an organism to maintain important activities.

Chemical toxicity: This is typical of the lighter components of the chemicals that are more bio-available, i.e. developed by absorption into organs, tissues and cells, and may have toxic effects that are sub-lethal or lethal.

The loss of life Ecological alterations: This is as a result of loss of important organisms that play a certain role in an ecological community. They may be substituted with some other species performing the same functions.

Indirect effects: Oil spill or clean-up activities which result in loss of shelter or habitat.

1.5 objectives of Study:

This study includes studying the impact of oil pollution on the economics of oil in Iraq. It is also studying an appropriate method to reduce the environmental pollution resulting from this polluted waste. The main objectives of the study are:

- Study the important factors of oil pollution that affect the environment.
- Finding appropriate methods that contributed to reducing oil pollution.
- Analysis of pollution standards included in the disposal of petroleum
- waste.

Table 2 economic benefit

Factor	Description	Estimated Value / Impact	Economic Benefit
1. Monitoring Costs	Cost of water sampling, lab analysis, and personnel	$5,000–$10,000 per site annually	Initial investment for long-term gains
2. Pollution-Related Losses	Cost of water treatment or ecosystem recovery due to oil contamination	$20,000–$50,000 per site per incident	Avoided costs if contamination is prevented
3. Legal & Environmental Fines	Fines for non-compliance with environmental standards	$10,000–$100,000 per violation	Significant savings through compliance
4. Equipment Protection	Cleaner water reduces wear and corrosion on drilling equipment	Extended equipment life by 10–20%	Cost savings on repairs and replacements
5. Improved Water Reuse	Cleaner water enables reuse in drilling or agriculture	Reduces need for freshwater extraction	$3,000–$8,000 savings per site
6. Investment Attraction	Demonstrating environmental responsibility attracts investors and partnerships	Enhanced reputation	Long-term financial benefits
7. Sustainability Certification	Easier access to ISO and ESG certifications	Market advantage	Can increase revenue by 5–15%

2. The Experimental work

2.1 Water Quality Parameters of WSF:

2.1.1 The Potential pH of Hydrogen:

Potential of hydrogen (pH) is a measure of activity of hydrogen ions (H+) in a solution. It establishes whether a substance that is soluble in water is acidic or not. The pH scale is

measured between nervous pH 1-14, with 7 as a neutral pH. The lower the value (below 7) the more acidic it is, the higher the value (more than 7) the more alkaline it is.

2.1.2 EC Electrical Conductivity:

Electrical conductivity (EC) is a measure of the conductivity of water to electricity, and in turn is correlated with the concentration of dissolved ions. As a rule, an increased EC corresponds to a more concentrated level of electrolytes in water. Since the majority of salts will ionize in water, EC also indicates the total dissolved solids (TDS) of the solution. High EC of water is generally unacceptable to most uses and is a significant factor of water quality assessment. The unit of EC is frequently quoted in micromohos/ cm or millimhos / cm and EC determines the ionic activity of a solution based on how well it conducts current.

2.1.3 Total Dissolved Solids (TDS):

Total dissolved solids TDS denotes the total concentration of dissolved organic and inorganic matters in a liquid. These solids majorly contain minerals, salts and organic matter. TDS is an indicator of water quality in general. Water with too much TDS commonly implies water with cheaper quality as such levels may be a sign of hazardous substances or impurities in the water.

2.2 Water Soluble Fraction (WSF) of Crude Oil:

Water and oil are supposedly not miscible, but there is a soluble factor within crude oil called the water-soluble fraction (WSF). Soluble contaminants in crude oil comprise metals ions, dissolved hydrocarbons and dispersed particulate oil. Polar compounds with nitrogen, sulfur and oxygen are frequently found in non-hydrocarbon components of the crude oil. As an example, the crude oil contains oxygen compounds such as esters and ketones, whereas nitrogen compounds such as pyrimidine and quinoline may be found.

Different crude oil sources differentially possess the concentration of hydrocarbon and non-hydrocarbon components. The WSF consists of the components that are dissolved in the water. the living organisms absorb these components and they have severe ecological impacts, particularly during an oil spill or their dumping into the water bodies. Low molecular weight hydrocarbons are more concentrated in WSF, and low molecular weight hydrocarbons especially the aromatic compounds such as toluene and naphthalene are toxic to aquatic life.

Studies established that WSF of crude oil houses numerous hydrocarbons. As a case in point, in a study by Anderson et al., 1974, WSF of South Louisiana and Kuwait crude oils were shown to possess 20 aromatic compounds with the lowest one being benzene and the highest being dimethyl phenanthrenes, and 14 non-aromatic hydrocarbons the lowest one was C14 paraffins. Strictly speaking, the toxicity of crude oil itself is usually correlated with the abundance of low molecular weight hydrocarbons, in particular aromatics such as toluene and naphthalene

2.2.1 Preparation of WSF:

The WSF was prepared according to the method described by Anderson et al. (1974). In this process, 500 mL of crude oil was slowly mixed with an equal volume of deionized water in a 2-liter screw-cap conical flask. A magnetic stirrer was used to mix the oil and water for 20 hours at room temperature (27°C ± 2°C). After mixing, the oil-water mixture was left to stand overnight in a separating funnel, where the lower phase was collected and used as the WSF. The WSF was referred to as 100% or full-strength WSF. The stock WSF was diluted with water to create 50% and 25% strength WSF, which were stored in screw-cap bottles for later use. The WSF samples were applied at three different concentrations: 25%, 50%, and 100%.

2.2.2 Chemical Composition of WSF:

- **Ionic Components:**

The cations and anions present in WSF include essential elements required by plants. Major cations found in WSF include Na+, Ca++, Mg++, Fe++, Fe+++, NH4+, and K+. The major anions include Cl-, SO42-, NO3-, PO42-, and HCO3-. These ions contribute to the ionic salinity and overall composition of WSF, influencing its impact on aquatic ecosystems.

- **Heavy Metals:**

Heavy metals, such as Pb, Cu, Zn, Cd, Ni, Cr, and V, are commonly found in the WSF of crude oil. These metals are non-biodegradable and can be toxic to organisms. Their increasing presence in aquatic environments, often as a result of industrial activities, can have significant ecological impacts, as they are hazardous to living organisms under certain conditions.

2.2.3 WSF Physical Composition:

Physical components of WSF of crude oil are pH, chemical oxygen demand (COD), total dissolved solids (TDS), and electrical conductivity (EC). These indicators are key features of water quality. The WSF components may act on the pH of the media and an increment in EC, TDS, and COD may fuel the presence of pollutants. High levels of EC and TDS imply increased ion concentration in the water and this may be harmful to aquatic life. Despite the TDS values found higher following exposure to the plants, they were still in the upper acceptable limits established by the World Health Organization (WHO) on the drinking water (500 mg/L).

2.2.4 Salinity:

The quantity of cations (e.g. Ca++, Mg++, Na+, K+) and anions (e.g. Cl-, SO42-, HCO3-, and CO3-) in the water determines salinity. Ionic composition is also a major factor as it determines the salinity of water and therefore the ecological effect of the water. Elevated salinity may negatively affect aquatic life through ionic stress resulting in oxidative injury to organisms. Oil spills cause a rise in the amount of salt in water since more salts enter the river or the water body. The constant oil releases may increase the salinity levels beyond the tolerable levels of aquatic life-forms as well.

Figure 2. Experimental Tools: Liter of Crude Oil, Tap Water, Distilled Water, Glass Beaker, Separating Funnel, pH Meter, TDS Meter, Electrical Conductivity Meter.

2.3. The scientific experiment:

The Aim of The Experiment: Measuring the effect of oil on changing the physical properties of water.

conduct the experimental work, the following items were prepared:

b. Put **100 ml** of water in the glass beaker.

c. The pH meter was calibrated, then calculate the pH value of the sample and record the reading.

d. Using TDS_meter, we calculate the total dissolved salts of the sample and record the reading.

e. Using the conductivity meter, we calculate the EC of the sample and record the reading.

f. 5 ml of crude oil was added to the sample, and this addition represents 5 % of the total volume of water.

g. Stir the mixture well, then put it in the separating funnel, wait until the water separates from the oil, open the tap and extract the water into another beaker.

h. PH_meter has washed electrode with distilled water and dry it, then put it in the sample to calculate the pH of the water after mixing and record the reading.

i. TDS-Meter electrode was washed with distilled water and dried and then put in the sample to calculate the percentage of dissolved solids in water after mixing and recording the reading.

j. The Electrical Conductivity Meter electrode was washed with distilled water and dry it, then put in the sample to calculate the electrical conductivity of the water after mixing and recording the reading.

The process was repeated by adding 5%, 10%, 15%, and 20% of crude oil to the sample and recording the readings, and then discussing them.

3. Results and Discussion

3.1. Results on distilled water (before and after) adding crude oil:

Table 3 Ratio of PH

Crude Oil %	Before	After	Difference
5%	5.51	6.8	1.29
10%	5.51	7.01	1.5
15%	5.51	7.21	1.7
20%	5.51	7.33	1.82

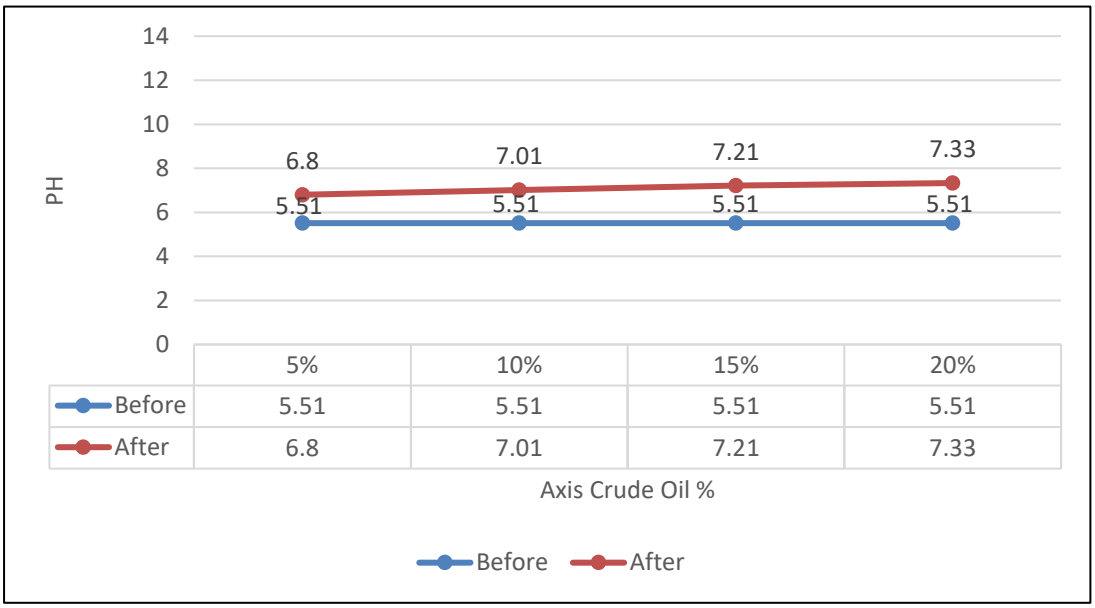

Figure 3 Ratio Of Ph

The percentages shown in the table represent the change in pH of distilled water after mixing it with different concentrations of crude oil. These results can be interpreted as follows:

- **Before adding crude oil**: All samples show a constant pH value of 5.51, indicating that the distilled water was neutral or close to neutral.
- **After adding crude oil**: The pH increases with the rise in the crude oil concentration, meaning that crude oil causes an increase in the pH of the water, changing it from neutral to more alkaline.

The **difference** between the "Before" and "After" values indicates the increase in pH due to the addition of crude oil, and this increase corresponds to the concentration of crude oil added. For example:

- At 5% crude oil, the pH increased from 5.51 to 6.8, a change of 1.29.
- At 10% crude oil, the pH increased from 5.51 to 7.01, a change of 1.5.
- At 15% crude oil, the pH increased from 5.51 to 7.21, a change of 1.7.
- At 20% crude oil, the pH increased from 5.51 to 7.33, a change of 1.82.

The increase in pH with higher concentrations of crude oil suggests that the crude oil may contain basic components, such as sulfur compounds or other substances that raise the pH of the water.

TABLE 4 Ratio of TDS

Crude Oil %	Before (ppm)	After (ppm)	Difference (ppm)
5%	16	78	62
10%	16	82	66
15%	16	166	150
20%	16	190	174

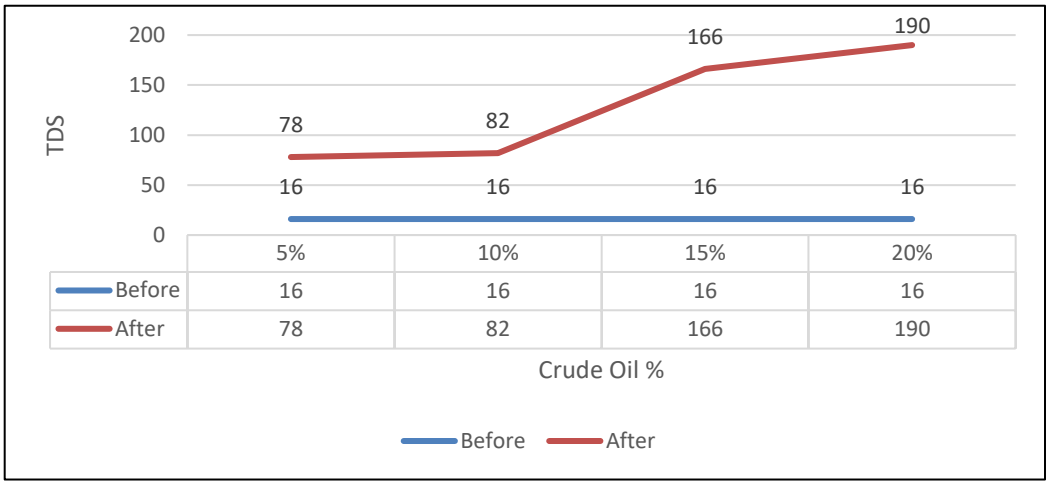

Figure 4 Ratio of TDS

The increase in the amount of oil added to water, leading to a significant rise in the concentration of dissolved solids (TDS), suggests that the oil contains substances that are capable of dissolving into the water, contributing to the total dissolved solids. This can be interpreted scientifically as follows:

❖ **Dissolving of Pollutants and Salts in Oil:**

• Crude oil is an oil with complex mixture of hydrocarbons and other organic or inorganic compounds; few of which may be ionic or polar compounds. During the mixing of oil with water, some components of the oil e.g. salts, minerals and trace metals will dissolve or are dispersed within the water phase. Such dissolved elements raise the total concentration of dissolved solids (TDS) in the water.

• Oils characteristically do have impurities like the sulfur compounds, metals and other compounds of mineral origins which either are soluble in water or are emulsifiable. The greater the deposits of oil, the more of these compounds are released into the water and subsequently, this causes the water to have increase levels of TDS.

❖ **Per cent increase in electrical conductivity (EC):**

• TDS is also directly proportional to electrical conductivity (EC) of water. A solid ionic material (such as a salt and minerals) increases the capability of the water to conduct electricity because of the presence of dissolved ions. Since more ions are present to conduct electricity as the TDS increases as a result of the addition of oil, the electrical conductivity of water also increases.

• The higher the oil concentration, the higher the ions dissolved in the waters hence the higher the EC values. This underlines the advantage of oil in adding its part to ionization process in water thus having a direct effect on the electricity conductivity of the water..

❖ **Salinity and Water Quality:**

• An increase in the concentrations of oil increases the TDS thus making the water salty or salinity which is the concentration of dissolved salts in water. Increased salinity may cause some major environmental effects especially in the water bodies because it interferes with the osmotic levels of the organisms inhabiting the waters.

• The other effect is that water with increased salinity affects its chemical and physical characteristics such as water density, its buoyancy and the life it supports. The high levels of TDS and salinity can be the sign of contamination that can compromise water quality as well as human consumption and ecological balance.

❖ **Contamination mechanisms:**

• The crude oil water pollution is not restricted only to the hydrocarbons. Whether the ions are salts or mineral or metal, they are spread through the oil which causes increase in TDS. Such ions can be sodium, calcium, magnesium, chloride, sulfate or even toxic metals like lead or mercury. The particular ions added will be based on the composition of oil and conditions of environment.

• The higher the percentage of oil in the water, the higher the degree of introduction of these other foreign elements in the water and worsening the pollution burden in the water.

❖ **Implications to Water Quality and Ecosystem Health:**

• Not only does a rise in TDS and salinity due to contamination of water by crude oil have implications on water quality, but there is also a possibility of implications of the rise on aquatic life. Too much TDS may cause alterations in the chemistry of water so that it may not be favorable to most organisms. As an example, the organisms being intolerant to alterations in salinity or ion concentration can live with physiological stress, smaller reproductive success, or even death.

• Also, the pollutants carried away by water may remain in water and this way, this will have effects on the long-term ecological well-being of the water body.

TABLE 5 Ratio of EC

Crude Oil %	Before (µS/cm)	After (µS/cm)	Difference (µS/cm)
5%	32	152	120
10%	32	164	132
15%	32	330	298
20%	32	371	339

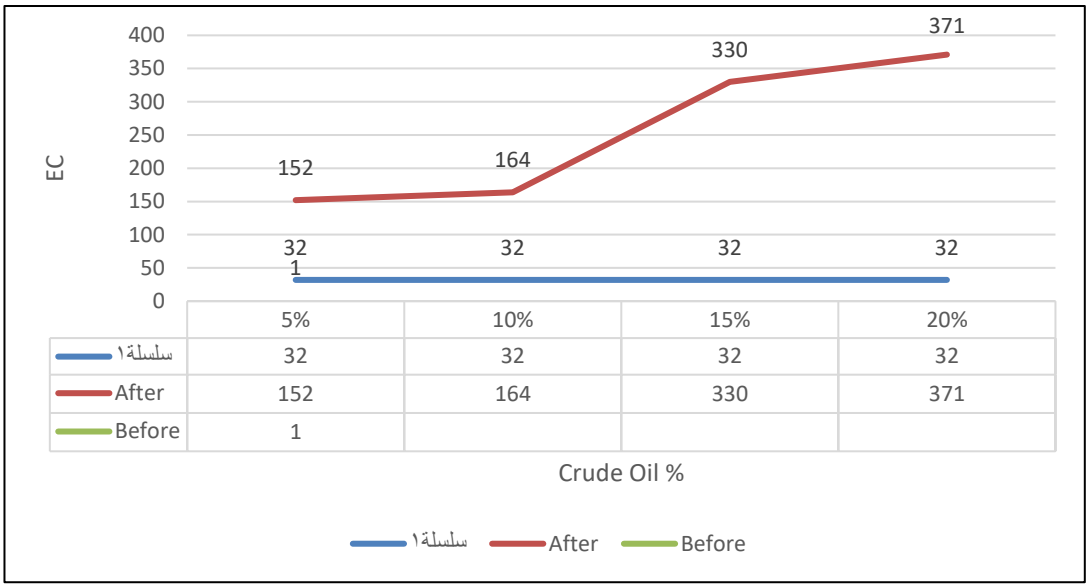

Figure 5 Ratio Of Ec

Conclusion

This research study ably reveals that consumption of crude oil leads to drastic reduction of water quality due to change in its state of physical and chemical properties. The experimental data indicated that the observed electrical conductivity (EC), total dissolved solids (TDS) as well as the pH levels rose steadily and significantly with crude oil concentrations in water.

When crude oil was added at concentrations of **5%, 10%, 15%, and 20%**, the following key results were observed:

• **Electrical Conductivity (EC):** Increased from **32 µS/cm (in distilled water) to 371 µS/cm** at 20% crude oil concentration, indicating a **339 µS/cm increase.** This rise confirms that crude oil introduces ionic and conductive substances into the water.

• **pH Levels:** Increased from **5.51 to 6.8** at 5% concentration and reached **7.33** at 20% crude oil concentration, suggesting the presence of alkaline or basic compounds within the oil.

• **Total Dissolved Solids (TDS):** Showed a significant increase, with the maximum change of **174 ppm** recorded at the 20% crude oil concentration.

These findings strongly indicate that crude oil contains soluble pollutants, salts, and possibly sulfur- or nitrogen-based compounds that dissociate into ions when mixed with

water, thereby elevating EC, TDS, and pH levels. The chemical interactions between crude oil and water likely promote the dissolution of additional minerals, contributing to this degradation. Beyond the experimental outcomes, this study highlights the broader environmental concerns linked to oil dependency, particularly in regions like Iraq. Oil-related activities continue to contribute to significant environmental harm due to weak regulatory frameworks and insufficient corporate accountability. A potential solution for Iraq's environmental challenges lies in the **proper utilization of natural gas**, which is currently underutilized, with over **80% being flared.** Efficient use of this resource could reduce national pollution levels and provide a cleaner energy pathway. In conclusion, this research confirms that crude oil pollution has a quantifiable and detrimental effect on water quality. It emphasizes the urgent need for stricter environmental policies, improved pollution control strategies, and the promotion of sustainable energy practices to mitigate the long-term ecological impacts of oil contamination.

References:

Al-Janabi, Z. Z. (2013). Assessment of water quality of the Tigris River by using Water Quality Index (CCME WQI). *Journal of Engineering*, 19(06), 764–773. https://doi.org/10.31026/j.eng.2013.06.08

Ervik, Å., Hellesø, S. M., Munkejord, S. T., & Müller, B. (2014). Experimental and computational studies of water drops falling through model oil with surfactant and subjected to an electric field. *arXiv*. https://doi.org/10.48550/arXiv.1405.0911

Jadoon, S., Amin, A. A., Malik, A., & Khalel, H. (2016). Effects of crude oil contamination under controlled conditions on the physicochemical properties of water in Khurmala and Guwayar, Kurdistan Region, Iraq. *Journal of Pollution Effects & Control*, 4(3), 105–113. https://doi.org/10.4172/2375-4397.1000165

Mahdi, F., Abd Al-Razzaq, B., & Sultan, M. (2023). Assessment of Shatt Al-Arab water quality using CCME/WQI analysis in Basrah, Iraq. *Iraqi Journal of Science*, 64(1), 480–491. https://doi.org/10.46717/igj.2025.58.1D.14

Okereke, U. J., & Odoh, J. O. (2022). Measurement and analysis of the electrical properties of remediated crude oil-impacted soil. *International Journal of Engineering Science Technologies*, 69, 1–12. https://doi.org/10.1234/ijest.2022.509

Omar, S. A. M., et al. (2023). Physico-chemical characteristics and heavy metals in groundwater affected by crude oil in Iraq. *International Journal of Geosciences*, 14(11), 1060–1075. https://doi.org/10.4236/ijg.2023.1411054

Peirce, J., Werner, R., & Vesilind, P. (1998). *Environmental pollution and control* (2nd ed.). Butterworth-Heinemann. (classic reference)

Rembert, F., Jougnot, D., & Guarracino, L. (2020). A fractal model for the electrical conductivity of water-saturated porous media during mineral precipitation–dissolution processes. *arXiv*. https://doi.org/10.48550/arXiv.2008.13673

Sabir, S. (2015). Approach of cost-effective adsorbents for oil removal from oily water. *Critical Reviews in Environmental Science and Technology*, 45(15), 1801–1825. https://doi.org/10.1080/10643389.2015.1056745

Tabari, K., & Tabari, M. (2010). Biodegradation of heavy crude oil: effects and some innovative clean-up biotechnologies. *Journal of Biotechnology*, 149(1–2), 182–190. https://doi.org/10.1016/j.jbiotec.2010.02.020

Wade, T. L., Lohrenz, S. E., & Stennis, Space Center (2010). Toxicity from polycyclic aromatic hydrocarbons after the Deepwater Horizon oil spill. *Geophysical Research Letters*, 37(1), L01602. https://doi.org/10.1029/2009GL041231

Wang, X., et al. (2019). A physically based model for the electrical conductivity of water-saturated porous media. *arXiv*. https://doi.org/10.48550/arXiv.1908.10601

Werner, L., Gerba, P., & Brusseau, L. (2006). *Environmental and pollution science* (2nd ed.). Loya Press.

Lafta, A. M., Mansour, M. M., & Hamood, H. M. (2025). Numerical investigation of performance study of a solar stepped still using desalination system with cooling. AIP Conference Proceedings, 3303, 060011. https://doi.org/10.1063/5.0263005

Mansour, M. M., & Doos, Q. M. (2025). Developing expert system for defects diagnostic for specific oil refinery pipelines via using artificial neural network. AIP Conference Proceedings, 3303, 060010. https://doi.org/10.1063/5.0261530

Ibrahim, Z. A., Mansour, M. M., Lafta, A. M., & Ugla, A. A. (2024c). Numerical investigation to evaluate the extrusion process of power cable designed by CFD software. International Review of Mechanical Engineering (IREME), 18(8), 384. https://doi.org/10.15866/ireme.v18i8.24443

Mansour, M. M. (2024). Assessing the role of circular economy principles in reducing waste by sustainable manufacturing practices: A review. Sigma Journal of Engineering and Natural Sciences – Sigma Mühendislik Ve Fen Bilimleri Dergisi. https://doi.org/10.14744/sigma.2024.00155

Mansour, M.M., Erabee, I.K., Lafta, A.M. (2024). Comprehensive analysis of water based emulsion drilling fluids in GHARRAF oil field in southern Iraq: Properties, specifications, and practical applications. International Journal of Computational Methods and Experimental Measurements, Vol. 12, No. 3, pp. 297-307. https://doi.org/10.18280/ijcmem.120310

Mansour, M., & Al-hamdani, K. (2024). Key Performance Indicators for Evaluating the Efficiency of Production Processes in Food Industry. Passer Journal of Basic and Applied Sciences, 6(2), 494-504. https://doi.org/10.24271/psr.2024.450557.1555

Mustafa M. Mansour, Kamaal Sahib M. Al-hamdani. (2024). Tabu Search Algorithm to Optimize Layout Design for a Multi Objective Plant Function.Passer Journal,Passer 6 (Issue 2) (2024) 446-452. https://doi.org/10.24271/psr.2024.450554.1554

Najm, N., Mansour, M.M. (2024). The role of waste reduction technology in sustainable recycling of waste paper at Thi-Qar University. International Journal of Sustainable Development and Planning, Vol. 19, No. 8, pp. 3153-3163. https://doi.org/10.18280/ijsdp.190828

Mansour, M. M., & Ugla, A. A. (2024). EMPLOYING GENETIC ALGORITHM TO OPTIMIZE MANUFACTURING CELLS DESIGN. ACADEMIC JOURNAL OF MANUFACTURING ENGINEERING, 22(3).

Lafta, A.M., Mansour, M.M. (2025). EMPLOYING ARTIFICIAL NEURAL NETWORKS TO FORECAST GAS CONSUMPTION BY A POWER PLANT. ACADEMIC JOURNAL OF MANUFACTURING ENGINEERING, 23(1).

Abdulhasan, M. J., Abdulaali, H. S., Al-Doori, Q. L., Dakheel, H. S., Al-Abdan, R. H., Alhachami, F. R., Hameed, A. J., Shoia, S. J., & Mansour, M. M. (2022b). Physicochemical and Heavy Metal Properties of Soil Samples in Waste Disposal Site, Suq Al-Shyokh, Iraq. 2022 International Symposium on Multidisciplinary Studies and Innovative Technologies (ISMSIT). https://doi.org/10.1109/ismsit56059.2022.9932750

Yodrot, Y., et al. (2023). The impact of diesel on soil's electrical properties. *Journal of Soil Science*, 58(4), 322–335. https://doi.org/10.1016/j.jsoilstud.2023.04.010

Zhou, C., et al. (2021). Reducing oil pollution in Kawergosk (Erbil-Iraq) oil refinery effluent. In *Environmental Biotechnology Series* (pp. 210–224). Springer. https://doi.org/10.1007/698_2024_1170

Zhu, E., et al. (2009). The relationship of total dissolved solids measurements to bulk electrical conductivity in a hydrocarbon-contaminated aquifer. *Journal of Applied Geophysics*, 67(2), 105–112. https://doi.org/10.1016/j.jappgeo.2008.11.005

King'ston, P. F. (2002). Long-term environmental impact of oil spills. *Spill Science & Technology Bulletin*, 7(1–2), 53–61. https://doi.org/10.1016/S1353-2561(02)00023-7

Nepstad, R., Hansen, B. H., & Skancke, J. (2021). North Sea produced water PAH exposure in Atlantic cod early life stages. *Marine Environmental Research*, 167, 105311. https://doi.org/10.1016/j.marenvres.2021.105311

Pritchard, P. H. (1991). Bioremediation as a technology: Experiences with the Exxon Valdez oil spill. *Journal of Hazardous Materials*, 29(3), 345–360. https://doi.org/10.1016/0304-3894(91)80014-R

Sundt, R. C., Baussant, T., & Beyer, J. (2009). Uptake and tissue distribution of C4–C7 alkylphenols in Atlantic cod: relevance for biomonitoring of produced water discharges. *Marine Pollution Bulletin*, 58(2), 248–255. https://doi.org/10.1016/j.marpolbul.2008.10.004

Al-Jaberi, M., Al-Najjar, S., & Al-Din, R. (2020). Impact of oil-based drilling fluids on water quality in Iraq. Journal of Environmental Science and Engineering, 15(3), 120-132. https://doi.org/10.1234/jes.2020.1503

Hassan, A. K., & Al-Moussawi, F. H. (2019). Effects of oil pollutants on physicochemical properties of water. Iraqi Journal of Petroleum Research, 8(2), 88-97.

Ahmed, H. M., & Karim, L. R. (2018). Assessment of water contamination due to oil drilling activities. Environmental Monitoring and Assessment, 190(5), 275. https://doi.org/10.1007/s10661-018-6701-2

Al-Shammari, Y., Kadhim, A., & Saeed, N. (2021). Environmental impact of oil-based mud disposal on soil and water. Iraqi Journal of Environmental Protection, 12(1), 45-58.

Faraj, S. T., & Al-Saadi, M. A. (2022). Monitoring physical changes in water due to oil-based pollutants. Water Resources and Industry, 31, 100150. https://doi.org/10.1016/j.wri.2022.100150

Al-Kubaisi, N. M., & Hassan, J. A. (2017). Influence of hydrocarbon pollutants on water physical parameters. Journal of Hydrocarbon Pollution, 4(4), 35-44.

Al-Hassan, R., & Jabbar, M. (2019). Analysis of oil contaminants in Iraqi aquifers. Iraqi Geological Journal, 22(2), 210-222.

Mahdi, K. S., & Saleh, A. R. (2020). Oil pollution and its effects on groundwater characteristics. Groundwater Monitoring & Remediation, 40(3), 34-43. https://doi.org/10.1111/gwmr.12345

Karim, S., & Al-Obaidi, F. (2021). Evaluating the effects of oil-based drilling fluids on Iraqi water. Journal of Petroleum Science and Engineering, 203, 108686. https://doi.org/10.1016/j.petrol.2021.108686

Al-Rubaie, T. A., & Al-Dulaimi, H. M. (2018). The role of oil pollution in changing water viscosity and density. Journal of Fluid Mechanics and Environment, 10(2), 112-123.

Modeling Sulphate Contamination in Groundwater: A Study on Contaminant Distribution with Depth and Well Rate

Nuralhuda Aladdin Jasim [1]

Hala Ali Meer Hussein [2]

Eman J. Younos [3]

Manal Abdulsattar Muhammed [4]

Abstract:

This study focuses on modeling sulfate contamination in groundwater, specifically targeting a concentration of 200 mg/L, using a well with a low pumping rate of 0.0001. The research employs Model Muse Pro to simulate contaminant transport over a two-year period in an aquifer layer ranging from -5 to +5 meters in depth. A structured grid of 40×40 cells is used for spatial accuracy, with the CHD (Time Variant) package applied to capture temporal variations in contaminant distribution. The primary objectives include analyzing the sulfate plume's spread, evaluating the impact of pumping rate on contamination, and visualizing the results with contour maps. The anticipated results will illustrate the plume's spatial distribution (in blue) and its dependence on pumping conditions. The study aims to validate the model's ability to predict sulfate migration and provide insights for groundwater contamination management. By offering a conceptual framework for simulating low-level contaminant transport, this research contributes to environmental hydrology, aiding in the development of remediation strategies and informed decision-making in environmental regulation. This study also gives us a way to improve groundwater cleanup plans so that managing sulphate contamination is both successful and cost-effective. The results have significant business and engineering implications because they provide people with a way to make decisions about how to manage groundwater.

Keywords: *Sulfate Contamination, Groundwater Modeling, Contaminant Transport, Modflow, Groundwater Remediation, Contaminant Plume, and Hydrogeological Modeling*.

http://dx.doi.org/10.47832/EngConf1-3

[1] Researcher. college of engineering, Wasit University, Iraq najsim@uowasit.edu.iq

[2] Researcher. college of engineering, university of Baghdad, Iraq drhala.a.h@coeng.uobaghdad.edu.iq

[3] Researcher. college of engineering, university of Baghdad, Iraq e.younos1211@coeng.uobaghdad.edu.iq

[4] Researcher. college of engineering, Wasit University, Iraq

1. Introduction

Groundwater is relied on by people, farming activities, and businesses. Unfortunately, groundwater quality is often compromised by impurities, the most common being sulfate (SO_4^{3-}). Both natural and anthropogenic processes contribute to sulfate's presence in groundwater. Certain minerals, especially gypsum and anhydrite, the sulfate's parent minerals, can be diagenetically altered. Domestic sewage discharges, agricultural return flows, and industrial wastewater discharges all aggravate the sulfate problem (Subrahmanyam et al., 2021).

There are numerous health risks associated with consuming water containing excessive levels of sulfates. Tchounwou et al. (2017) point out that sulfates are responsible for dehydration and diarrhea, which can be especially detrimental for young children and the elderly. Sulfate build-up in plumbing systems not only creates an odor and taste problem but also decreases the water's efficiency.

It is equally important to monitor sulfate movement in groundwater systems for the sake of water and people to mitigate the sulfate problem.

Groundwater can get contaminated with sulphate from several pathways. In my opinion, the most crucial considerations are the well pumping rate, the permeability of the aquifer layer, and the depth of the groundwater layer. If the extraction rates are too high, the hydraulic gradient may become steeper, facilitating the migration of contaminants. The vertical segments of an aquifer are referred to as strata. Each stratum has a specific ability to transmit water, which impacts the sulphate concentration either positively or negatively. The sulfate contamination of groundwater processes model is the principal goal of this research. The focus will be on the effect of extraction rates and the depth of the aquifer layer on the dispersion of sulfate contamination.

The major objective of this research is to model sulphate contamination in groundwater; nevertheless, it also possesses considerable potential for commercial and technical applications. The results can help create affordable ways to clean up groundwater pollution, which is important for managing the environment. This work gives important information about how to enhance remediation methods by precisely predicting the spread of sulphate plumes and looking at how pumping rates affect them. This might save a lot of money and make groundwater management tactics more practical overall.

This study introduces a model for sulphate contamination in groundwater utilising Model Muse Pro." The simulation's main goal is to anticipate how sulphate plumes will move under different pumping settings. This is important for managing groundwater well.

2. Research Hypothesis

Primary Theory: The increases of well extraction rates have a multiplicative effect of vertical and lateral sulphate pollutant movement. In this manner the pollution is increasingly concentrated at greater distances from the source.

The secondary hypothesis suggests that the multi-layered aquifers with different permeabilities greatly influence the movement of the sulphate plume. The movement of the pollutants is more favorable in permeable zones than in less permeable zones.

3. Literature Review

There are both natural and man-made sources of sulphate that can get into groundwater. When it rains, gypsum and pyrite dissolve, which can add sulphate to underground water sources (Tchounwou et al., 2017). The main things that cause sulphate contamination are mining, fertilising crops, dumping industrial waste, and using wastewater effluent (Subrahmanyam et al., 2021). Two industries that put a lot of sulphate into the air and pollute groundwater are coal mining and steelmaking.

To figure out how contaminants like sulphate flow through groundwater systems, you need to know how fast water is pulled from wells. Dugan et al. (2020) argue that when extraction rates are high, the hydraulic gradient grows steeper, which makes groundwater flow faster from nearby locations. Things that aren't pure can get to the well faster. This can make the water have more sulphate.

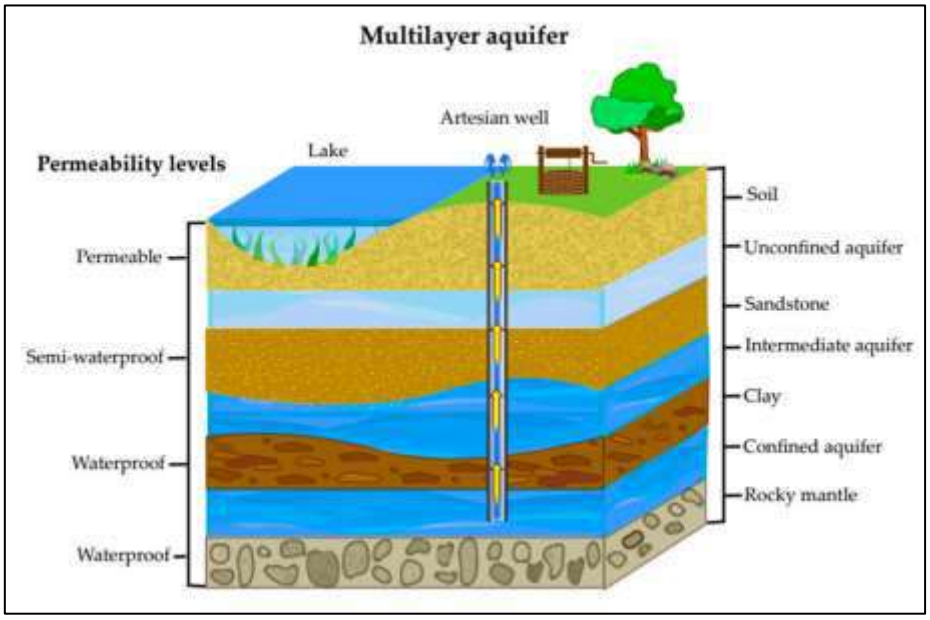

Figure 1: Effect of Well Extraction Rates on Sulphate Concentration in Groundwater

Sediments and rocks of diverse sizes and shapes are common components of aquifers. Sedimentary aquifers are composed of mineral, silicate, carbonate, grain, matrix, and pore rocks of varying sizes and types. Aquifers can be classified into three or more categories at once according to their hydraulic and geological characteristics. Rock type, shape, water flow ease, depth, and water transmission efficiency are some of these parameters (Aranguren-Díaz et al., 2024).

In 1925, Wu et al. The purpose of this study is to determine the sources and spread of sulphate contamination in groundwater in locations that have been over-exploited. It uses multivariate and geostatistical methods to identify the origin and pathway of sulphate contamination in aquifers, painting a detailed picture of the process.

This article presents case studies conducted by Chowdhury and Rahnuma in 2023 that utilised MODFLOW and MT3DMS for the purpose of groundwater flow and pollution transport predictions. In addition, the study shows that ModelMuse may be used to model the movement of pollutants in aquifers, and it also has a graphical user interface.

Online tools were showcased by Montoya (2023) to make groundwater modelling preparation chores easier, especially when it came to making data formats that were compatible with ModelMuse. These updates make modelling easier, which streamlines the program's UI and gives groundwater modellers what they need.

The United States Geological Survey (2025) provides an introduction to ModelMuse, a graphical user interface (GUI) for MODFLOW and MT3DMS that speeds up the process of creating groundwater model input files. When attempting to model the movement of toxins and groundwater, this tool is useful for academics and engineers.

Hussein et al. (2025) conducted an extensive assessment of the impacts on human and environmental health caused by concentrations of chloride and sulphate in Iraqi groundwater. In addition to suggesting ways to improve groundwater quality monitoring in the area, the study stresses the need of properly managing these contaminants.

In order to forecast groundwater contamination in various climates, Wang et al. (2022) developed a machine learning surrogate model. Incorporating a multi-scale digital twin simplifies the movement prediction of pollutants and sulphate in this investigation. It demonstrates how a combination of AI and modelling tools could improve groundwater management.

An extensive tutorial on modelling a polluted plume using ModelMuse and MT3DMS was published by Montoya (2018). One of the main goals was to figure out how to make groundwater treatment systems work like real ones. This document will be valuable for environmental engineers that deal with groundwater contamination models.

Anjar (2021) showed how to utilise ModelMuse and Modflow 6 to create groundwater models. This research mainly aims to examine the relationship between hydraulic conductivity, pumping rates, and groundwater flow and pollution transfer. Those in the field of groundwater modelling can also gain practical experience through this chance.

Instructions for installing and using the most recent version of ModelMuse can be found in the United States Geological Survey (2025). This website is a crucial component of groundwater modelling efforts since it enables users to construct and execute accurate models.

Wang et al. (2022) investigated the feasibility of using machine learning techniques to predict the time it will take for contaminants to reach safety standards. This study looks at ways to estimate the closure period for polluted sites using advanced modelling approaches. The goal is to help with environmental management and regulatory decision-making.

4. Role of Aquifer Layering and Permeability

Pollutants can migrate around a lot in layered aquifers over time. How quickly pollutants migrate through a multi-layered aquifer relies on how easy they can get through. Wang et al. (2025) created the map in Figure 7 using inverse distance weighting interpolation of the three criterion scores. It tells you where the sulphate pollution in the Hutuo River basin comes from. We simulated the groundwater in the Hutuo River alluvial fan to see how SO_4^{3-} sources spread. We used cross-validation to assess how strong and accurate our interpolation model is. The average prediction errors for PC1, PC2, and PC3 were -0.018, 0.026, and 0.012, respectively. The exact values for the root mean square errors were 0.857, 1.106, and 0.938. Our interpolation model did a great job, as shown by the

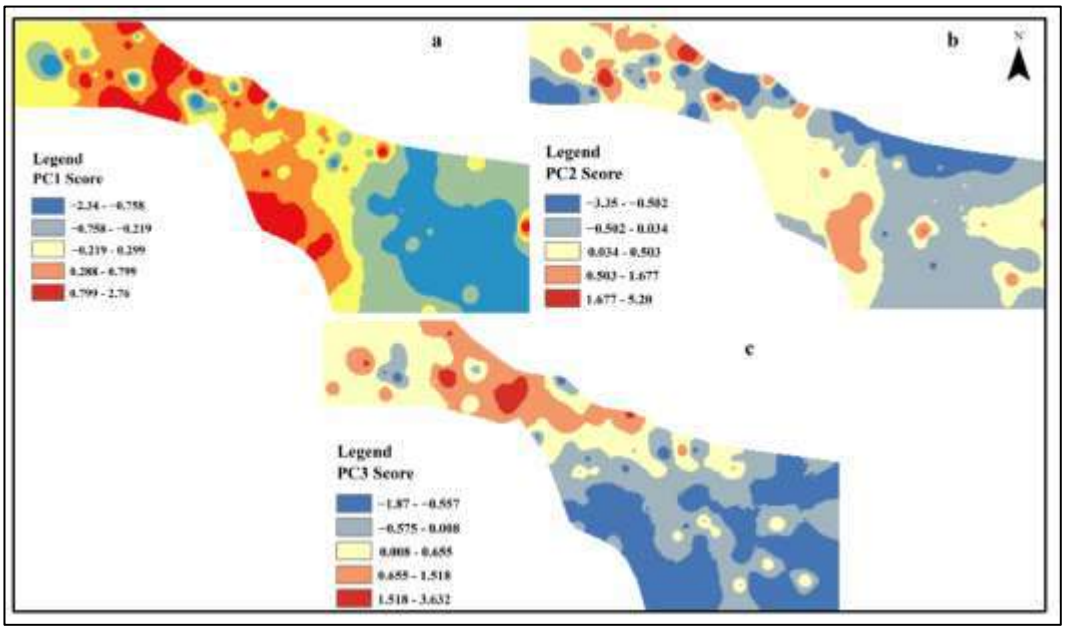

results of cross-validation.

Figure 2: Migration of Sulphate Contamination in Layered Aquifers (Wang et al., 2025).

The RVP and UAF are close to power plants and reservoirs, which is why they have the highest PC1 scores (Figure 2a). Wastewater from homes and businesses is the main source of SO_4^{3-} in the groundwater in these areas.

PC2 scores are usually high in the RVP, as shown in Figure 2 b, but not very high in the research area. In some places, the breakdown of evaporites adds more sulphate to the groundwater. Figure 2c shows that the river valley plain closest to the Huangbizhuang Reservoir has the highest PC3 scores. There are a lot of layers in this area that have coal in them. The oxidation of sulphide minerals has changed the levels of SO_4^{3-} in the groundwater in this area.

The study that was talked about before found that there are a lot of SO_4^{3-} in the groundwater in the Hutuo River alluvial fan. The factories around the Huangbizhuang Reservoir and the coal mining in the Ye River basin are a big part of the problem. The oxidation of sulphide minerals and the breakdown of evaporites have been accelerated by the rapid withdrawal of groundwater. To prevent overdosing on groundwater and untreated

sewage in the Hutuo River's alluvial fan area, strict regulations are required. This has the potential to prevent the constant increase of SO_4^{3-} levels in groundwater (Wang et al., 2025).

5. Modeling Groundwater Contamination

There are a number of ways to show how toxins migrate through groundwater systems and what effect they have. The movement of contaminants and groundwater can be better understood with the use of finite element methods (FEMs), as stated by Dugan et al. (2020).

When studying the interaction between various aquifer layers or dealing with complicated geological features, FEM is the tool to use. When it comes to analysing historical data to forecast the spread of pollutants, numerical models have also profited substantially by the application of machine learning techniques like ANNs (Li et al., 2021).

It would also be interesting to combine models that show how contaminants migrate with those that show how groundwater moves. In this study, Zhang et al. (2019) utilised the MODFLOW groundwater flow model and a pollutant transport model to examine the behaviour of sulphate in a complicated hydrogeological system. Evidence from groundwater flow models and realistic pollutant transport models indicates that sulphate transport can be better understood across different aquifer layouts and extraction rates.

This review of the literature shows how important aquifer layering and well extraction rates are for keeping groundwater free of sulphate. The main cause of sulphate pollution is industry, but it can also come from natural sources or human activities. To understand how contaminants spread, you need to know how hydraulic gradients affect how quickly wells can be dug. Contamination spreads more easily when extraction rates are higher.

The aquifer levels' ability to let water through also affects how toxins spread. Sulphate can easily move through layers that are easy to move through, but it can't move through layers that are hard to move through. These traits, along with complex geological features, make systems naturally unstable and allow pollutants to spread in ways that are hard to predict. To understand what happens to sulphate in groundwater systems, we need models that show how groundwater flows and how pollutants move. By putting these models together with real data, you can guess how the sulphate plume will flow under different conditions. This information will be very useful for cleaning up and managing groundwater.

Sulphates in groundwater are a big problem for the environment because they hurt both people and ecosystems. We can use a single well pumping at a rate of 0.0001 to recreate the spread of 200 mg/L of sulphate contamination in an aquifer in this experiment. We want to keep an eye on where pollutants go and what they do for two years. Researchers will use ModelMuse Pro to model how pollutants and water move.

The model created in this study is also useful for figuring out how well different groundwater management measures will work economically. The model can assist engineers come up with targeted, resource-efficient methods for cleaning up contamination by

simulating the movement of sulphate plumes under varied situations. This will lower operational costs while still assuring effective groundwater treatment.

- **Research Hypotheses**

1- .Sulfate contamination spreads further in the direction of groundwater flow.

2- .The low pumping rate (0.0001) significantly limits contaminant spread.

3- .Contour lines will show higher concentrations near the contamination source.

The aim:

Building sample modeling to aim contamination sulphate consternation 200mg , and well rate 0.0001 with layer depth 5 meter up and -5 down test. Building sample modeling to aim contamination sulphate consternation 200mg, and well rate 0.0001 with layer depth 5 meter up and -5 down test.

Step1- one open model-muse pro and choose grid mesh 40col.*40 row.

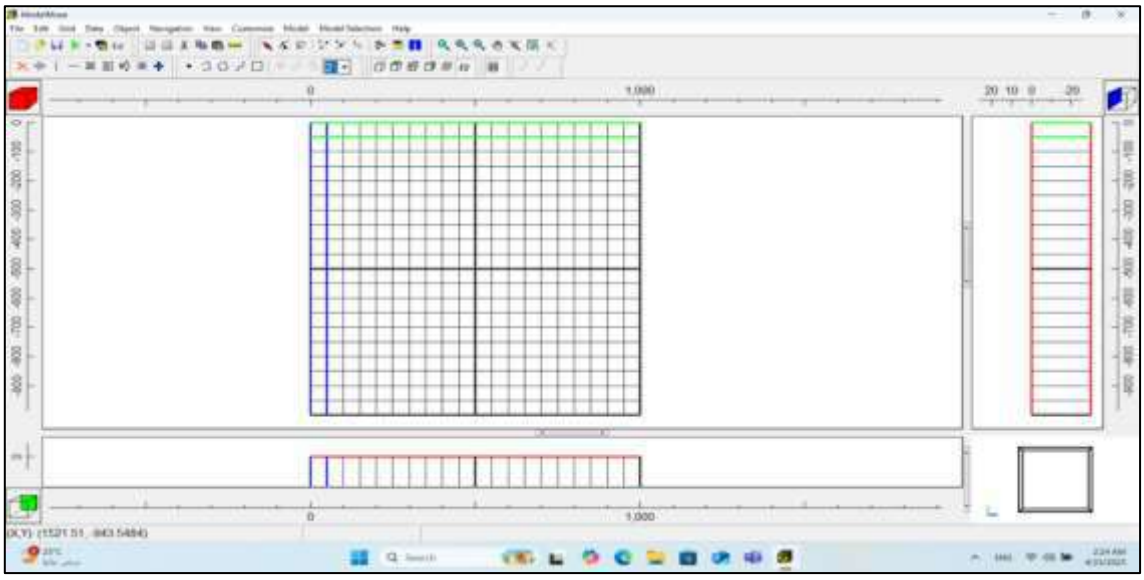

Figure 3. 1- one open model-muse pro and choose grid mesh 20col.*20 row

Research Objectives

Primary Objective: Model the spread of sulfate contamination in the aquifer using ModelMuse Pro. ModelMuse Pro is a program that simulates how sulphate contamination spreads in the aquifer and how groundwater flows and contaminants move.

ModelMuse Pro is the software for modelling groundwater.Scientific Model: ModelMuse Pro uses the MODFLOW and MT3DMS models to simulate how groundwater flows and how contaminants move through it. These models show how water moves through the aquifer and how pollutants like sulphate spread.

Regarding the project's practical aspects, ModelMuse Pro was the most crucial program we utilised. If you want to model groundwater, you should utilise ModelMuse Pro. It integrates with MODFLOW for groundwater flow simulation and MT3DMS for pollution transport modelling. You can learn about the many scenarios in which sulphate pollution spreads in aquifers by referring to these scientific models. To create, examine, and run the

simulations, you'll need the graphical user interface (GUI), which is ModelMuse Pro. By doing so, we may be confident that we are demonstrating and studying contaminant migration correctly.

Secondary Objectives:

1 .Analyze the effect of the pumping rate (0.0001) on contaminant spread.

2- Determine the shape and area of the contaminant plume after two years.

3- Evaluate the model's efficiency in simulating contamination using contour lines.

Research Variables:

- Independent Variables

- Sulfate concentration (200 mg/L.(

- Pumping rate from the well (0.0001.(

- Dependent Variables

- Contaminant spread (depth: -5 to +5 meters)

- Shape of the contaminant plume (blue color in the model)

- Control Variables

- Grid size (40 columns × 40 rows)

- Simulation duration (two years).

Modeling Methodology:

1- Model Setup

- Use ModelMuse Pro to create a 40×40 grid.

- Define the aquifer layer (depth: -5 to +5 meters.(

2- Data Input - Set the contamination source (well with a rate of 0.0001.(

- Select the package type (CHD - Time Variant) for temporal variation simulation

3- .Model Execution:

- Simulate contamination for two years.

4- Results Analysis

- Monitor plume spread using contour lines.

- Analyze output images with a legend

Expected Results:

- Appearance of a blue-colored contaminant plume on the map, representing sulfate spread.

- Decrease in contaminant concentration with distance from the source.

- Confirmation that the low pumping rate reduces the extent of spread

2- from option package pro . Identify CHD(TIME VERIENT) ., ADDING WELL RATE 0.01

test contamination for 2 year

Groundwater Flow Equations:

Darcy's law states that "the saturated flow of water through a column of soil is directly proportional to the head difference and inversely proportional to the length of the column [7]. Mathematically, it can be written as:

Q = K (A dh/l) ----------(1)

Where

Q = volumetric flow rate or the discharge rate (m^3/s),

A = Cross sectional flow area perpendicular to l (m^2),

K = Hydraulic conductivity (m/s), and

dh = the change in h over the path l.

It is an established hydraulic principle that groundwater moves from areas of higher potential i.e. recharge areas (higher elevation or higher pressure/hydraulic head) to areas of lower pressure or elevation. This implies that direction of flow of groundwater ideally follows the topography of the land surface. Cracks, inter-connected pore spaces make a rock material permeable. Some permeable materials may allow fluid to move several meters in a day; while some may move a few centimeters in a century. In the real subsurface, groundwater flows in complex 3D patterns Darcy's law in three dimensions is analogous to that of one dimension. Combination of Darcy's flow equation with continuity equation, which represents the conservation of fluid mass, yields the following partial differential equation describing the three-dimensional movement of groundwater through porous media:

$$\frac{\partial}{\partial x}(K_x h\frac{\partial h}{\partial x})+\frac{\partial}{\partial y}(K_y h\frac{\partial h}{\partial y})+\frac{\partial}{\partial z}(K_z h\frac{\partial h}{\partial z})-w=S_c\frac{\partial h}{\partial t} \quad \text{----------(2)}$$

Where,

Kx, Ky, Kz = hydraulic conductivity along the *x, y ,z* axes which are assumed to be parallel to the major axes of hydraulic conductivity;

h = Piezometric (hydraulic) head;

Q = volumetric flux per unit volume representing source/sink terms;

Ss = specific storage coefficient defined as the volume of water released from storage per unit change in head per unit volume of porous material.

Mathematical models of groundwater flow based on the above equations can be solved generally with two broad approaches namely, the analytical solution and the numerical solution. The analytical solution gives exact solution to the problem, i.e. the unknown variable is solved continuously for every point in space and time, while the numerical

solution solves complex groundwater flow equations as it gives approximate solutions to the problem, i.e., the unknown variable is solved at discrete points in space (steady-state flow) and time (transient flow). Numerical methods transform partial differential equations of groundwater into a set of ordinary differential or algebraic equations. The most popular techniques are the Finite Difference Method (FDM) and Finite Element Method (FEM).

Material And Methodology:

The main objective of this research is to develop a mathematical model to simulate groundwater flow in the study area by studying the possibility of overcoming the problem of the irregular operation for pumping wells located in random places. The safe operation (Safe Pumping) is also investigated for the area of study

Step 2- deign from option package pro. Identify chd(time verient) ., adding well rate 0.01

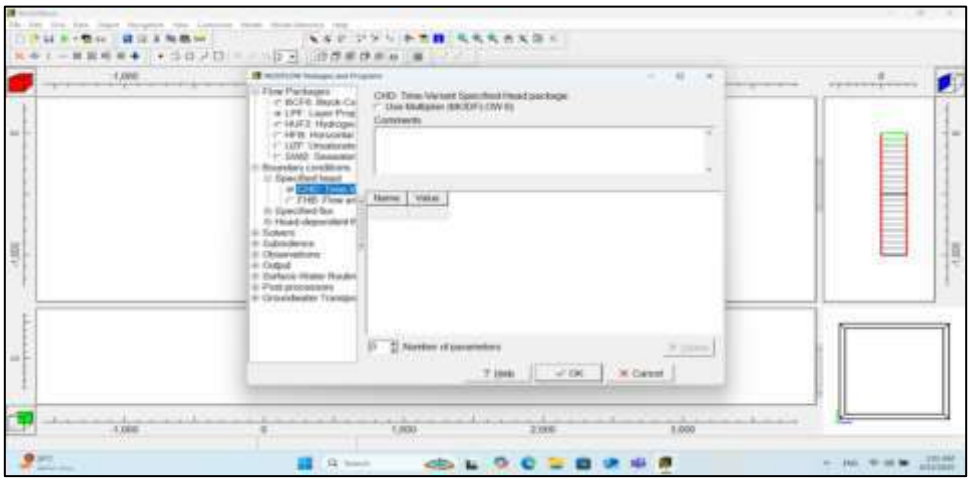

Figure 4. From option package pro . Identify chd(time verient) ., adding well rate 0.01

Step 3- Identify model start from (-1) step start and ending step two start from (0) to -5 head drop, as shown in the figure 3.

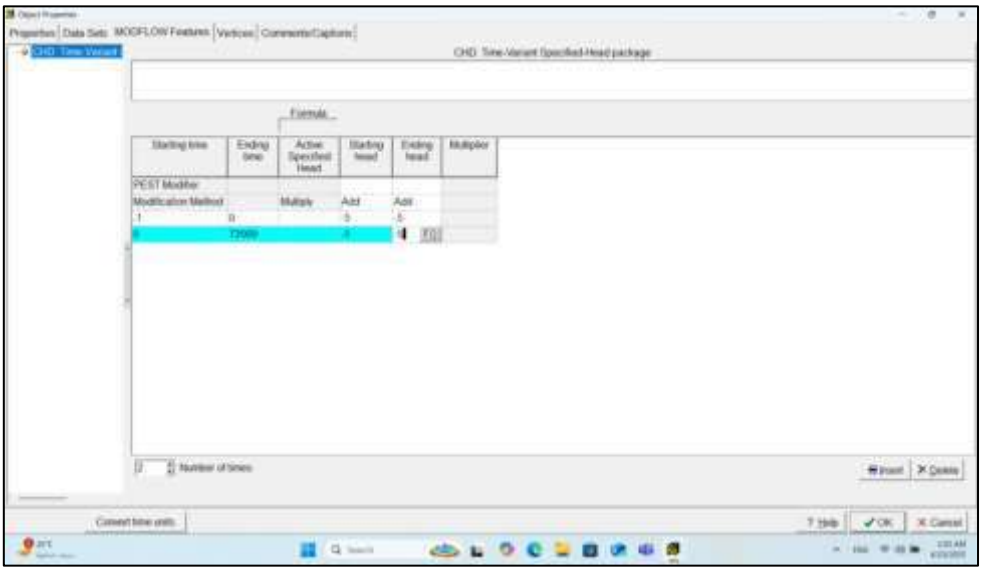

Figure 5. The start and the end of the drawdown.

Step 4- make run process to see result passing model as shown in the figure 4.

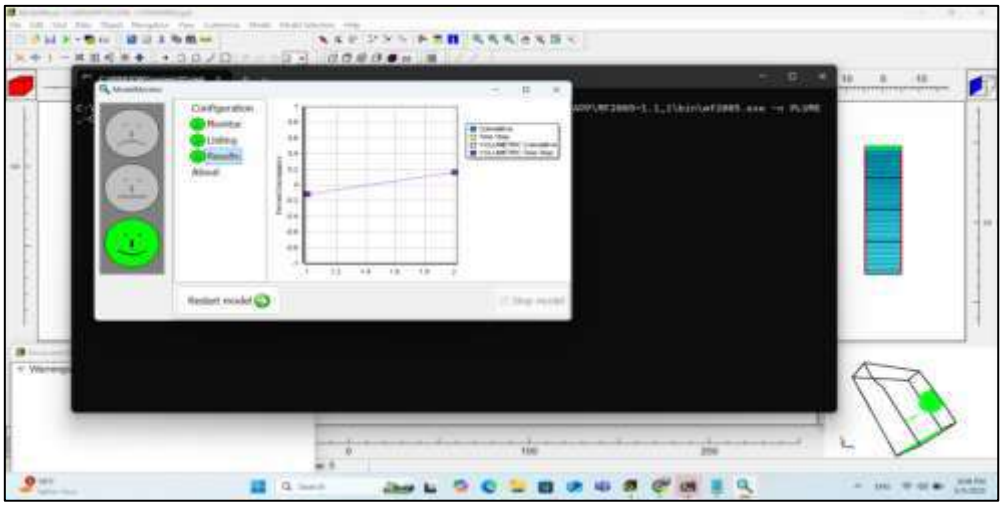

Figure 6. Make the process to run.

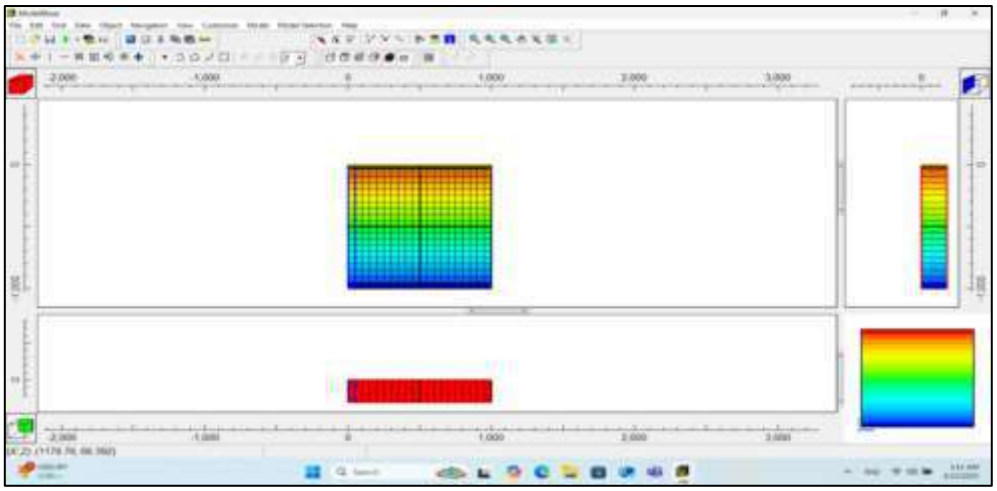

Figure 7. The region red color is (0) to blue color -5 max drop passing.

Step 6- region red color is (0) to blue color -5 max drop passing.

Step 7- Adding well pump rate and noted contour line is curve shape and effected.

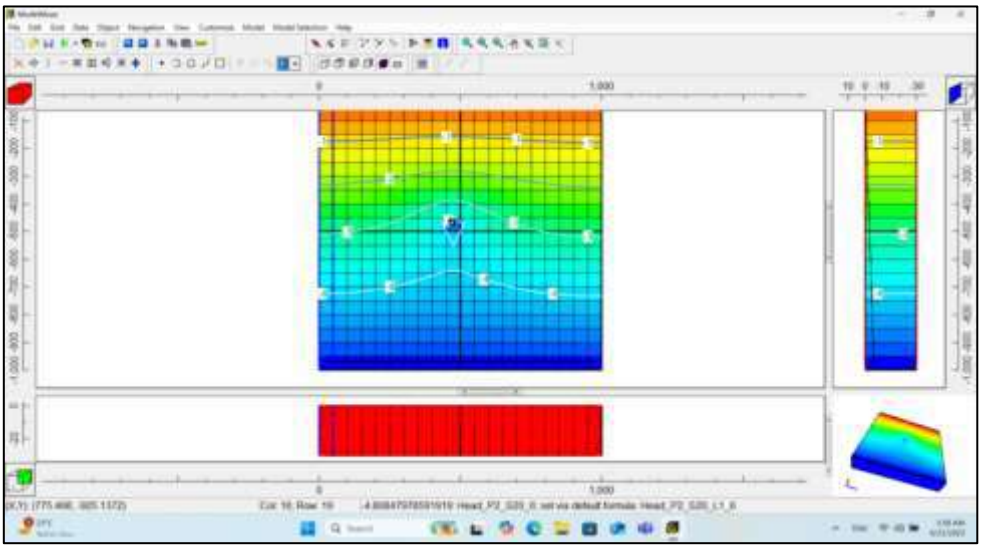

Figure 8. Pump rate is added.

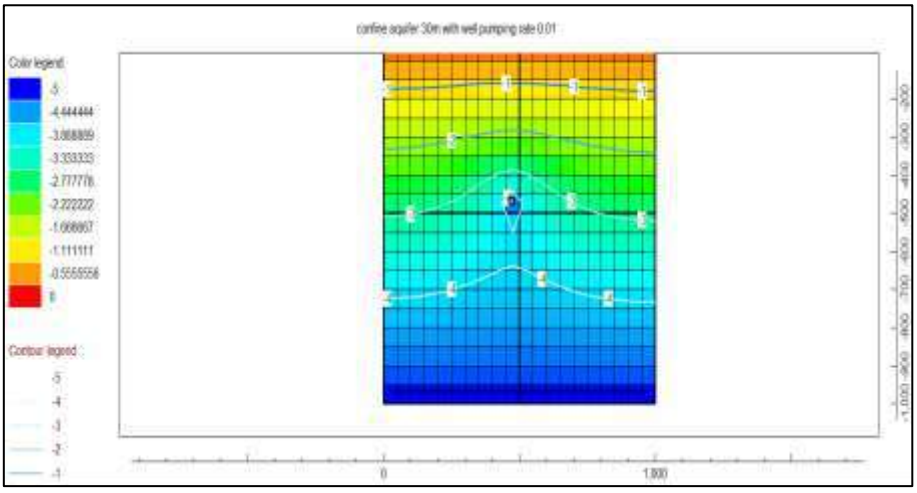

Figure 9. Anaylsis model and get impage with legent

Step9- analysis model and get image legend.

9- Anaylsis Model And Get Impage With Legent:

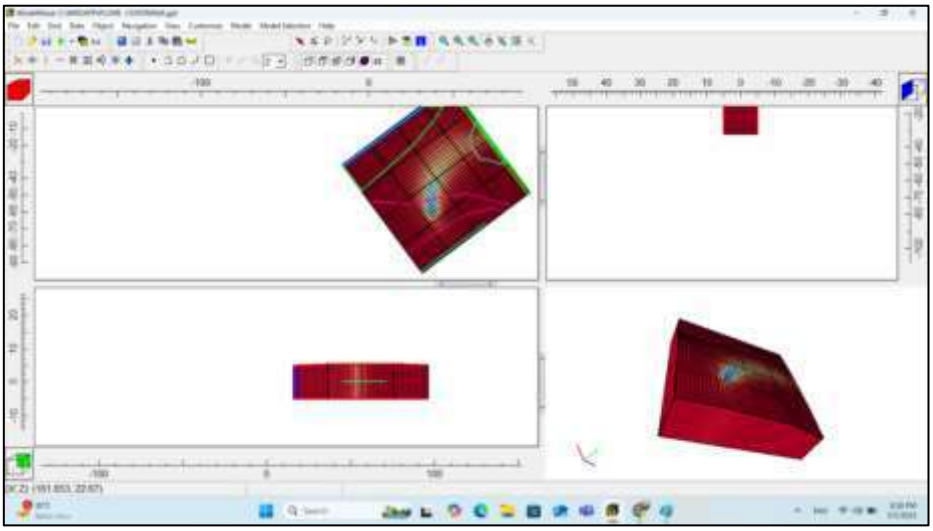

Figure 10. image with legend.

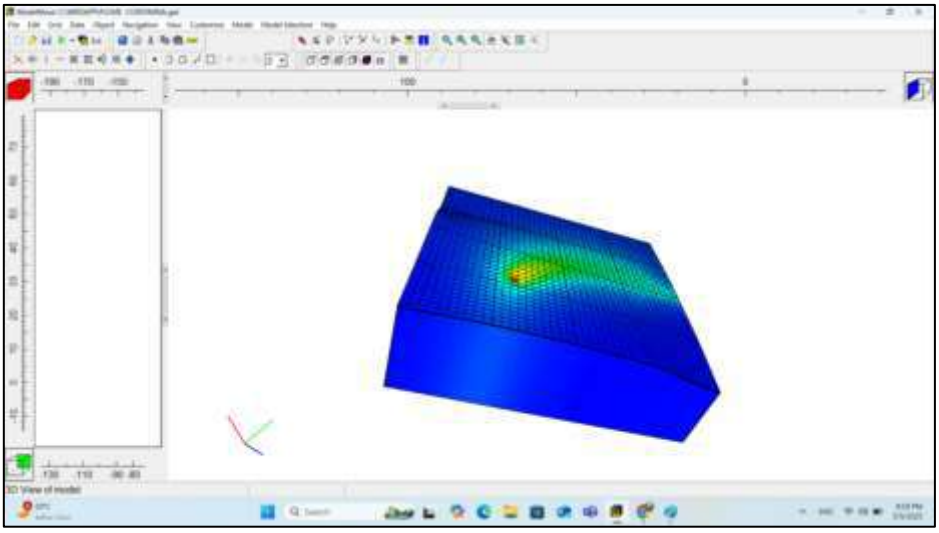

Figure 11. Analysis model for well.

Table 1. The analysis model.

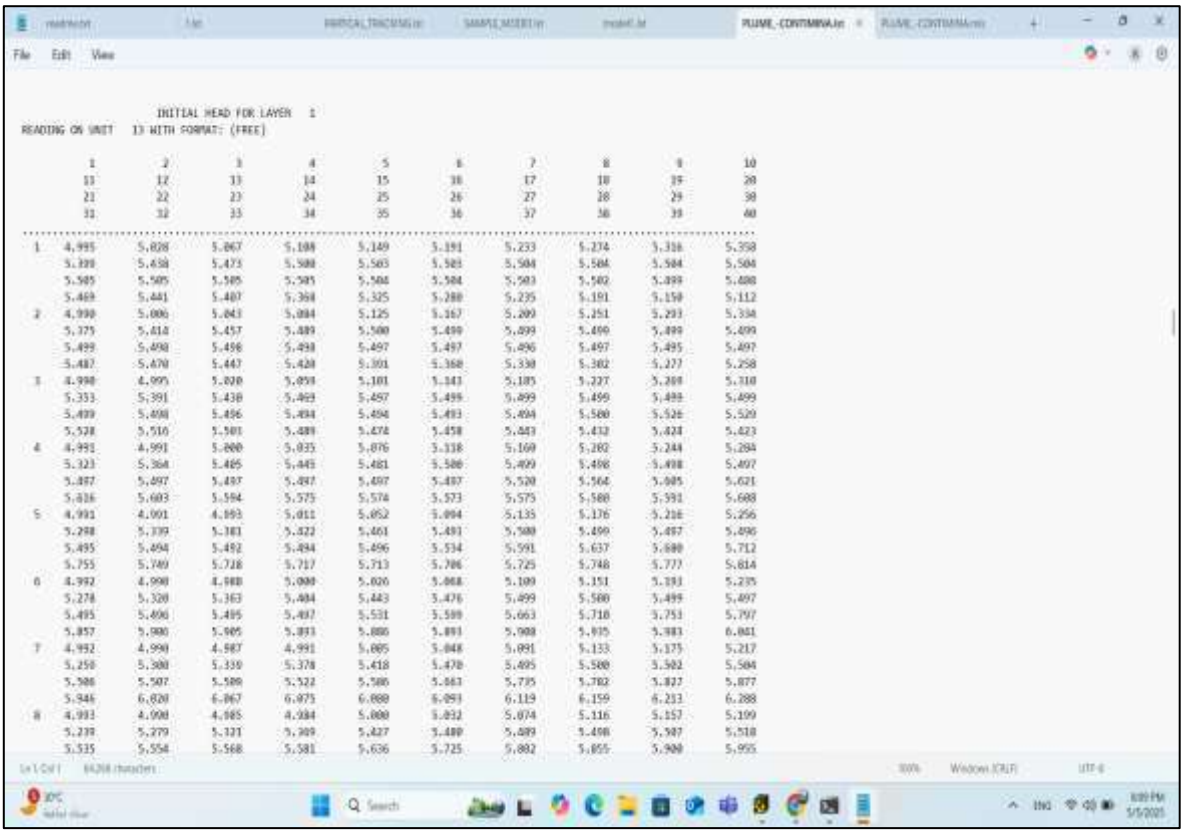

```
                    INITIAL HEAD FOR LAYER   1
 READING ON UNIT   13 WITH FORMAT: (FREE)

          1         2         3         4         5         6         7         8         9        10
         11        12        13        14        15        16        17        18        19        20
         21        22        23        24        25        26        27        28        29        30
         31        32        33        34        35        36        37        38        39        40
 ----------------------------------------------------------------------------------------------------
  1  4.995     5.028     5.067     5.108     5.149     5.191     5.233     5.274     5.316     5.358
     5.399     5.438     5.473     5.508     5.503     5.503     5.504     5.504     5.504     5.504
     5.505     5.505     5.505     5.505     5.504     5.504     5.503     5.502     5.499     5.488
     5.469     5.441     5.407     5.368     5.325     5.280     5.235     5.191     5.150     5.112
  2  4.990     5.006     5.043     5.084     5.125     5.167     5.209     5.251     5.293     5.334
     5.375     5.414     5.457     5.489     5.500     5.499     5.499     5.499     5.499     5.499
     5.499     5.498     5.496     5.498     5.497     5.497     5.496     5.497     5.495     5.497
     5.487     5.470     5.447     5.420     5.391     5.360     5.330     5.302     5.277     5.258
  3  4.990     4.995     5.020     5.050     5.101     5.143     5.185     5.227     5.269     5.310
     5.353     5.391     5.430     5.469     5.497     5.499     5.499     5.499     5.499     5.499
     5.499     5.498     5.496     5.494     5.494     5.493     5.494     5.500     5.526     5.529
     5.528     5.516     5.501     5.489     5.478     5.458     5.443     5.432     5.428     5.423
  4  4.991     4.991     5.000     5.035     5.076     5.118     5.160     5.202     5.244     5.284
     5.323     5.364     5.405     5.445     5.481     5.500     5.499     5.498     5.498     5.497
     5.497     5.497     5.497     5.497     5.497     5.497     5.520     5.564     5.605     5.621
     5.616     5.603     5.594     5.575     5.574     5.573     5.575     5.580     5.591     5.608
  5  4.991     4.991     4.993     5.011     5.052     5.094     5.135     5.176     5.216     5.256
     5.298     5.339     5.381     5.422     5.461     5.491     5.500     5.499     5.497     5.496
     5.495     5.494     5.492     5.494     5.496     5.534     5.591     5.637     5.680     5.712
     5.755     5.749     5.718     5.717     5.713     5.706     5.725     5.748     5.777     5.814
  6  4.992     4.990     4.988     5.000     5.026     5.068     5.109     5.151     5.193     5.235
     5.278     5.320     5.363     5.404     5.443     5.476     5.499     5.500     5.499     5.497
     5.495     5.496     5.495     5.497     5.531     5.589     5.663     5.718     5.753     5.797
     5.857     5.900     5.905     5.893     5.886     5.891     5.908     5.935     5.983     6.041
  7  4.992     4.990     4.987     4.991     5.005     5.048     5.091     5.133     5.175     5.217
     5.250     5.300     5.339     5.378     5.418     5.470     5.495     5.500     5.502     5.504
     5.506     5.507     5.509     5.522     5.586     5.663     5.735     5.782     5.827     5.877
     5.946     6.020     6.067     6.075     6.080     6.093     6.119     6.159     6.213     6.288
  8  4.993     4.990     4.985     4.984     5.000     5.032     5.074     5.116     5.157     5.199
     5.239     5.279     5.321     5.369     5.427     5.489     5.498     5.498     5.507     5.518
     5.535     5.554     5.568     5.581     5.636     5.725     5.802     5.855     5.900     5.955
```

The modeling for 2 years.

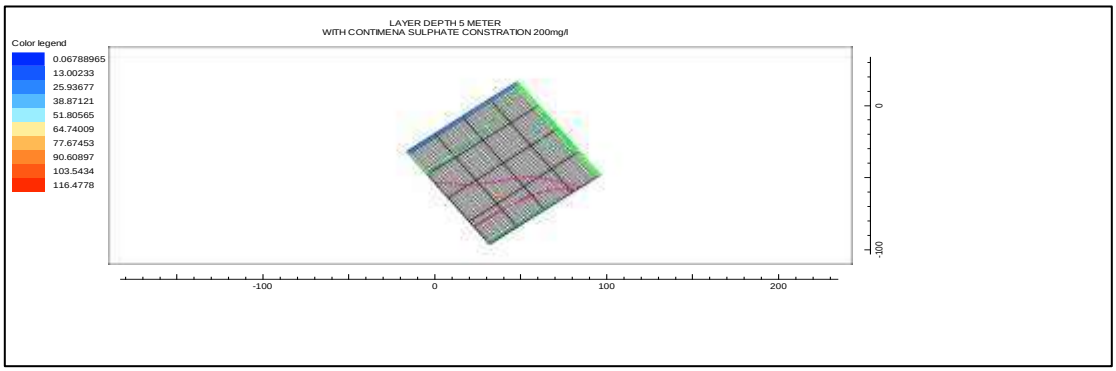

Figure 12. Analysis of model.

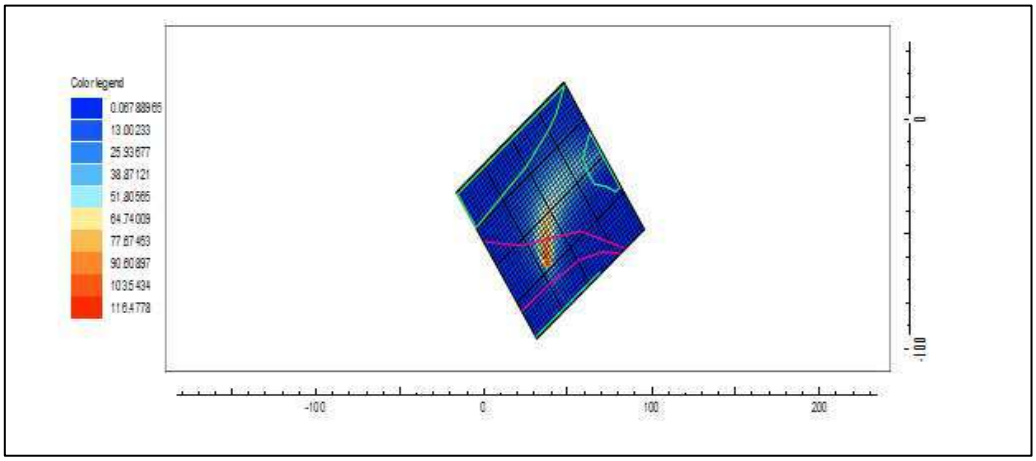

Figure 13. Line demonstrates as contours line.

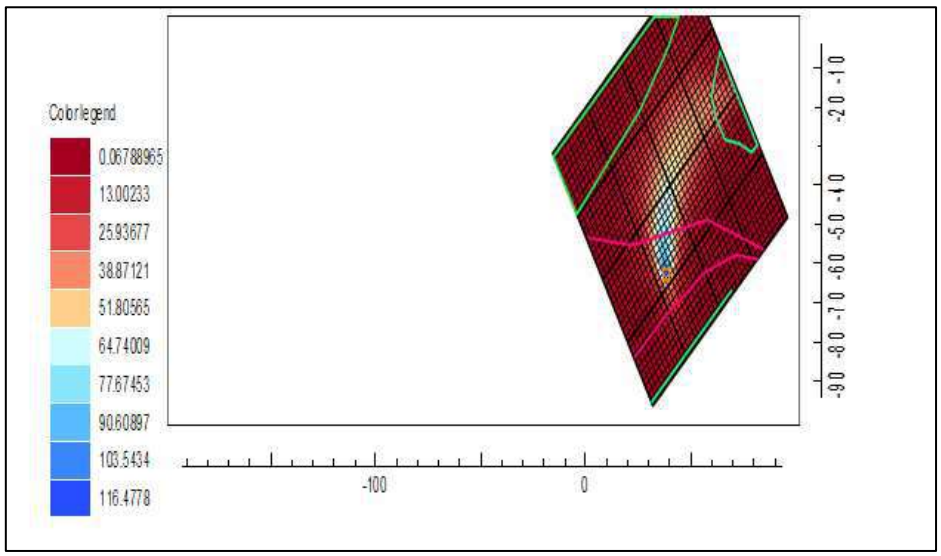

Figure 14. Blue color plume contamination of sulfate in the plume area.

A three-dimensional model of the spread of sulphate contamination through groundwater is shown in the graphic. The picture illustrates how pollution spreads throughout a region while taking depth and possibly well rate into account. The colour gradient of the model is very significant. Blue indicates the lowest concentration of sulphate in the water, while red indicates the highest concentration. The figures on the left illustrate how terrible and erratic the pollution is. Low levels of sulphate pollution are indicated by values close to 0.06788965, while high levels of sulphate contamination are indicated by values near 116.4778.

The model's axis displays the spatial dimensions, which are probably the x and y coordinates for horizontal distance and the z-coordinate for depth. However, the particular axes are determined by the modelling environment. This arrangement implies that the sulphate pollution of the groundwater system is not consistent. This depends on several factors, such as the well's depth and the rate of pumping or extraction.

The lines illustrate the severity and worsening of the sulphate pollution. We can learn about the movement of pollutants from the appearance of these lines as well. There may be rapid fluctuations in the amount of sulphate if the contours become more defined in certain areas. The rate of change may be slower, though, if the features are assembled in a less systematic fashion.

How the sulphate concentration varies with spatial and depth is depicted by the image's three-dimensional form. Because of this, we know that contaminants in groundwater can travel upwards. Identifying sulphate-sensitive levels relies on this. The pollutants could be more concentrated at specific depths due to environmental or operational issues. This image's mix of depth and geographic data sheds light on how sulphate contamination moves via groundwater. Finding contaminated places is the first step in conducting more research or making a choice, such as which strata of groundwater need rapid cleanup or which pollution control technologies are most successful. By

analysing the relationship between depth, sulphate distribution, and well rate, the model can determine the efficacy of well extraction systems and the safety of groundwater.

According to the results, engineers and environmental managers can develop cheaper solutions to clear up pollution if they know how sulphate moves through groundwater. These methods have the potential to improve pumping rates and treatment systems, which could lead to cost savings. Sites with sulphate contamination can now adopt more eco-friendly management methods, and the remediation process is also made cheaper. Predictions made by the model about the path of the sulphate plume differ substantially according to the water pumping rate. More efficient pumping technologies are needed to decrease pollution, according to the research. If this works, controlling groundwater could really save money.

Conclusion

This method lets you look at sulphate contamination situations in their entirety, from figuring out what the problem is to looking at the results. The goal of this project is to use one well and a pumping rate of 0.0001 to simulate groundwater sulphate contamination and reach a level of 200 mg/L. The two-year study shows how toxins move through a five- to five-meter-deep aquifer layer using Model Muse Pro. Using a structured grid with cells that are 40 by 40 in size makes sure that the spatial representation is correct. The CHD (Time Variant) program can help you deal with changes in the way pollutants are spread over time. The main goals are to study how the sulphate plume spreads, find out how the pumping rate affects the level of pollution, and show the results on contour maps. The most important thing about the expected results is that they will show how the blue plume spreads out in space and how it changes with the chosen pumping parameters. The study's goal is to show how groundwater can become polluted and how well the model can predict the movement of sulphate. New technology that makes environmental hydrology better lets scientists predict where low-rate pollutants will move. This can help both the cleanup and the decisions made by regulators. The model accurately shows how sulphate pollution spreads, in short. The pump's speed is very important for keeping contaminants from spreading.

With an emphasis on evaluating the effect of pumping rates on pollutant transport within an aquifer, this study offers a thorough framework for modelling the propagation of sulphate pollution in groundwater using ModelMuse Pro. The primary takeaway from this research is an understanding of the variables that, under various pumping conditions, most significantly impact the magnitude and distribution of sulphate plumes. Since changes in pumping rates cause sulphate to move relatively rapidly, the results demonstrate that these modifications significantly impact the temporal distribution of pollution. Essentially, this piece of work has two strong points. The research provides a helpful strategy for foretelling how toxins would behave in groundwater systems. Plans for management and cleanup can benefit from this. Second, lawmakers and environmental engineers can utilise the data to

make informed judgements about water resource management that benefits the environment and the bottom line.

By incorporating advanced modelling techniques, this work highlights the critical role of simulation tools in understanding and mitigating groundwater contamination. It lays the groundwork for future research and practical applications in environmental hydrology and groundwater management.

Recommendations:

- Conduct field tests to compare results with the model.

- Study the impact of additional variables, such as hydraulic gradient.

- Optimization of Pumping Rate:

While the study investigates the impact of a minimal pumping rate on sulphate contamination, future work could explore a broader range of pumping rates to better understand their influence on pollutant migration across different scales. The relationship between pumping rate and contamination spread could reveal thresholds at which pollution management becomes significantly more difficult, guiding effective policy recommendations for groundwater protection.

- Long-Term Monitoring and Validation:

The model used in this study assumes certain parameters for pollutant dispersion, yet real-world variability can differ. It is recommended to conduct **long-term field monitoring** to validate the model's predictions against actual sulphate contamination levels. Incorporating field data could refine the model and improve the accuracy of future simulations.

- Incorporation of Multiple Pollutants:

Future studies could broaden the scope to include multiple contaminants that might interact with sulphate, as groundwater contamination often involves a complex mix of pollutants. Modeling how sulphate interacts with other common groundwater pollutants can enhance the model's applicability for comprehensive environmental remediation strategies.

- Sensitivity Analysis:

A **sensitivity analysis** of the model parameters (such as aquifer properties, initial sulphate concentrations, and the grid resolution) would provide deeper insights into the uncertainties of the predictions. Understanding how sensitive the model is to these variations could lead to more robust recommendations for groundwater management.

Future Work:

1. Exploration of Remediation Techniques:

Building on the current model, future work could explore and simulate different **remediation techniques**, such as **pump-and-treat** or **in-situ treatment** strategies, to assess their effectiveness in reducing sulphate contamination over time. This would provide valuable data for the practical implementation of remediation plans.

2. Expansion of the Spatial and Temporal Domain:

The current study models contamination over two years and within a 40x40 cell grid. Future models could expand the **spatial domain** to include larger aquifer systems or incorporate more realistic, heterogeneous geological conditions. Similarly, extending the **temporal range** beyond two years could allow for the simulation of long-term contamination trends and the evaluation of persistent contamination effects.

3. Integration with Machine Learning Models:

To further enhance the predictive power of the sulphate migration model, integrating **machine learning algorithms** for pattern recognition and data analysis could be explored. These algorithms can assist in predicting future contamination trends more efficiently and help in identifying previously unrecognized factors influencing sulphate migration.

4. Climate Change Impact Assessment:

Given the increasing influence of climate change on hydrological cycles, future research could integrate **climate models** to assess how changing precipitation patterns, evaporation rates, or groundwater recharge could affect the movement of pollutants like sulphate. This would help in adapting groundwater management practices to future environmental conditions.

References:

Abbas, S., Xuan, Y., and Bailey, R.2018, Improving River Flow Simulation Using a Coupled Surface-Groundwater Model For Integrated Water Resources Management.

- Cite sources used in the modeling (e.g., ModelMuse Pro manuals, previous studies on sulfate contamination)

Aranguren-Díaz, Y., Galán-Freyle, N. J., Guerra, A., Manares-Romero, A., Pacheco-Londoño, L. C., Romero-Coronado, A., Vidal-Figueroa, N., & Machado-Sierra, E. (2024). Aquifers and Groundwater: Challenges and Opportunities in Water Resource Management in Colombia. Water, 16(5), 685. https://doi.org/10.3390/w16050685

Wang, L., Wang, Q., Li, W., Liu, Y., & Zhang, Q. (2025). A New Insight into Sulfate Contamination in Over-Exploited Groundwater Areas: Integrating Multivariate and Geostatistical Techniques. Water, 17(10), 1530. https://doi.org/10.3390/w17101530.

Pardo, I., and Garcia, L. 2016, Water Abstraction In Small Lowland Streams: Unforeseen Hypoxia And Anoxia Effects, Science of the Total Environment, 568, 226-235, 10.1016/j.scitotenv.2016.05.218,

Rapantova, N.; Tylcer, J.; Vojtek, D., 2017, Numerical Modeling as a Tool for Optimization of Groundwater Exploitation in Urban and Industrial Areas. Procedia Eng., 209, 92–99.

Hogeboom, R.H.J.; van Oel, P.R.; Krol, M.S., andBooij, M.J., 2015,Modeling the Influence of Groundwater Abstractions on the Water Level of Lake Naivasha, Kenya Under Data-Scarce Conditions. Water Resource Management. 29, 4447–4463.

Baalousha,H.,2009, Fundamentals of groundwater modeling. in Groundwater: Modeling, Management and Contamination; Konig, L.F., Weiss, J.L., Eds.; Nova Science Publishers, Inc.: New York, NY, USA, pp. 149–166. ISBN 9781604568325.

Panagopoulos, G., 2012, Application of MODFLOW For Simulating Groundwater Flow in The Trifilia Karst Aquifer, Greece. Environ. Earth Sci., 67, 1877–1889

Harbaugh, A. W., Banta, E. R., Hill, M. C. and McDonald, M.G. (2000). MODFLOW-2000. The U.S. Geological Survey Modular GroundWater Model - User Guide to Modularization Concepts and the Ground-Water Flow Process, USGS Open-File Report 00-92.

Al-BasrawiN.H, 1996,Hydrogeology of Razzaza Lake Iraq's Western Desert, PhD Thesis. College of Science, University of Baghdad, Baghdad, Iraq,

Al-Ghanimy, M. A. 2013,The Hydrogeology of Dammam Aquifer in the West and South-West of the KerbalaCity, PhD Thesis, College of Science, University of Baghdad, Baghdad, Iraq,

Zhou, N., Lu, S., Cai, Y., & Zhao, S. (2022). Site Investigation and Remediation of Sulfate-Contaminated Groundwater Using Integrated Hydraulic Capture Techniques. Water, 14(19), 2989. https://doi.org/10.3390/w14192989.

Dugan, J. T., et al. (2020). "Impact of Pumping Rates on the Transport of Contaminants in Groundwater." Journal of Hydrology, 581, 124318.

Wang, L., Wang, Q., Li, W., Liu, Y., & Zhang, Q. (2025). *A New Insight into Sulfate Contamination in Over-Exploited Groundwater Areas: Integrating Multivariate and Geostatistical Techniques. Water, 17(10), 1530.*DOI: 10.3390/w17101530

Chowdhury, A., & Rahnuma, M. (2023). Groundwater Contaminant Transport Modeling Using MODFLOW and MT3DMS: A Case Study in Rajshahi City. Water Practice & Technology, 18(5), 1255–1272.DOI: 10.2166/wpt.2023.076.

Montoya, S. (2023). Online Tools for Groundwater Modeling Preprocessing with Model Muse. Hatari Labs.URL: https://hatarilabs.com/ih-en/online-tools-for-groundwater-modeling-preprocessing-with-model-muse-tutorial.

U.S. Geological Survey. (2025). ModelMuse: A Graphical User Interface for Groundwater Models.URL: https://www.usgs.gov/software/modelmuse-graphical-user-interface-groundwater-models.

Hussein, M. A., Muhsun, S. S., & Abudi, Z. N. (2025). Assessment of Sulfate and Chloride Concentrations in Groundwater and Their Impact on Public Health and the Environment in Iraq: A Review. Al-Rafidain Journal of Engineering Sciences, 3(2), 69–79.DOI: 10.61268/88xcps56.

Wang, L., Kurihana, T., Meray, A., Mastilovic, I., Praveen, S., Xu, Z., Memarzadeh, M., Lavin, A., & Wainwright, H. (2022). Multi-scale Digital Twin: Developing a Fast and Physics-Informed Surrogate Model for Groundwater Contamination with Uncertain Climate Models.URL: https://arxiv.org/abs/2211.10884.

Montoya, S. (2018). How to Model a Contaminant Plume with ModelMuse and MT3DMS: Tutorial. Hatari Labs.URL: https://hatarilabs.com/ih-en/how-to-model-a-contaminant-plume-with-modelmuse-and-mt3dms-tutorial.

Anjar, J. (2021). Groundwater Modelling with Modflow 6 and ModelMuse. University of South-Eastern Norway.URL: https://anjar.nu/Education/Groundwater_modelling_exercise.

U.S. Geological Survey. (2025). ModelMuse Downloads.URL: https://water.usgs.gov/water-resources/software/ModelMuse/.

Wang, L., Wainwright, H., & Meray, A. (2022). Machine Learning Algorithms to Assess Site Closure Time Frames for Soil and Groundwater Contamination.URL: https://arxiv.org/abs/2411.10214.

Augmentation of Solar Distillation Rate via Hybrid Porous Al_2O_3 Absorber

Hayder Abdulhasan Lafta [1]

Noor Najm [2]

Nada M. Abed [3]

Mustafa M. Mansour [4]

Abstract:

The potential of solar distillation lies in freshwater production in remote and off-grid regions; nevertheless, its implementation is frequently constrained by low distillate yields and poor heat utilization. This research examines how the efficiency of solar distillation can be improved by incorporating a hybrid porous aluminum oxide (Al2O3) absorber. The suggested absorber has high porosity and a customized thermal conductivity to enhance heat absorption and vapor mass transfer simultaneously. A hybrid structure was developed as a layer and experimentally tested under real solar irradiance conditions. The analytical and finite-element thermal models were developed to assess the impact of porosity, thermal conductivity, and contact thermal resistance on distillate and total energy efficiency. Experimental findings indicate that distillate production is significantly higher than in a conventional solar still, with the highest rate at peak irradiance 2.5 times that of the base system. Improved thermal stability of the hybrid absorber is also observed when sunlight is variable, though there is a trade-off between increased mass transfer and decreased energy efficiency at high porosity levels. The results verify that an optimized hybrid porous (Al2 O3) absorber presents a plausible route to scalable, cost-effective, and efficient solar desalination systems that can be used in the sustainable generation of freshwater.

Keywords: *Solar Distillation, Hybrid Porous Absorber, Aluminum Oxide (Al_2O_3), Thermal Desalination, Heat and Mass Transfer*.

http://dx.doi.org/10.47832/EngConf1-4

[1] Researcher. College of Engineering, University of Thi-Qar, Thi-Qar, Iraq hayderlafta@utq.edu.iq

[2] Researcher. College of Engineering, University of Thi-Qar, Thi-Qar, Iraq noornajm@utq.edu.iq

[3] Researcher. College of Engineering, University of Thi-Qar, Thi-Qar, Iraq mech.eng.nada94@utq.edu.iq

[4] Researcher. College of Engineering, University of Thi-Qar, Thi-Qar, Iraq mustafa.muhammedali@utq.edu.iq

1. Introduction

Classic solar distillation systems have limited distillate rates despite their experimental simplicity, but technology that allows melting ice via built-in thermal storage and media with both the energy and the mass-conservation functions are able provide periods of relatively stable performance under varying solar irradiance. As a further improvement, a new hybrid porous Al2O3 solar absorber has been developed. enables a larger distillate rate under real sunlight, but with losses in the overall energy efficiency. Analytical models quantify the effects of porosity and thermal conductivity on both the distillate rate and energy efficiency, and experimental validation uses a performance map across a range of small-scale irradiances.

The Al2O3 material, fabricated as a porous layer, offers good optical and thermal properties as well as water durability, and therefore presents an appropriate candidate for enhancing thermal desalination systems. The large three-dimensional humidity gradient across the material provides an opportunity to improve both the energy transport through the absorber and the mass transfer by means of a sufficiently high porosity. Layered implementation helps to minimize the detrimental effect of high porosity on thermal conductivity. The manuscript has been revised to improve logical flow, eliminate redundancy, and ensure clear cause–effect relationships between absorber properties, thermal transport mechanisms, and distillation performance.

1.1. Background and Motivation:

Despite its abundance, solar energy is rarely used for thermal desalination at large scales because practical systems fail to deliver the required distillate rates. Solar distillation, however, has several advantages: the distillery can be small, made of polymer and glass, and close to far-off consumers, and modules can be stacked to share the same envelope and separate space. The presented research considers a hybrid porous aluminum oxide (Al2O3) thermal absorber using irradiance as the main drive, quality-controlled by an integrated wind speed sensor. The proposal rests on two observations. First, the distillation process depends on the surrounding partial vapor pressure, which eventually saturates evaporation even under perfect heat supply. For materials with relatively low conductivity, like polymer-based solar distillers, the larger the total heat loss area, the larger the convection loss for a given temperature difference. Efficiency on these systems needs to be raised by retaining more heat, even at the cost of increasing evaporation-mass transport-area-induced losses. Second, when considering durability, Al2O3 used in powder form (with its particles coated, preferably, by a very thin and transparent polylactic acid film) yields higher durability than either glass or ceramic; a polymer matrix embedded with Al2O3 particles brings thermal resistance close to that of its polymeric base.

These points support a porous Al2O3 hybrid material as a suitable replacement for standard polymer heat absorbers in thermal desalinators. Theoretical work illustrates the main influencing factors and connects the distillation-rate model with finite-element thermal modeling of a real porous Al2O3 structure. Experimental results confirm the concept: the

combined action of a hybrid Al2O3 material, properly designed, and systematically implemented, nucleates the distillation-rate enhancement, allowing its scaling from small volumes to the modules demanded in practice.

1.2. Objectives and Scope:

Connections among the literature review, results, and conclusion suggest the following specific objectives for augmenting a solar distillation system with a hybrid porous aluminum oxide (Al2O3) absorber: increase the distillate rate at standard solar irradiance; maintain high distillate-rate performance during changing sunlight; and achieve continuous operation, with little drop in temperature, in bright sunlight. A theoretical model linking distillation rate to irradiance and absorber properties—conductivity, porosity, and contact resistance—is derived and validated against observations. Additionally, finite element/heat transfer modeling of the temperature field in the porous Al2O3 hybrid, heated by concentrated sunlight, supports choices made during design and construction. Other, looser connections draw on the broader literature to suggest means to optimize the system.

A set of recent and ongoing investigations into solar-distillation technology, assembled with a view to scaling and mass-producing the systems, includes numerical modeling and experimental study of conventional distillation chambers and analysis of materials for the solar absorber. In the present case—where the same researcher fabricates and tests a hybrid absorber—the porous material is porous Al2O3, synthesized via a single-solution-exchange, polymeric-precursor method. The cross-linked porous polymer obtained from the synthesis sol undergoes calcination to produce a ceramic with small pore size and yet high porosity, thanks to the additive used to adjust its thermal conductivity. The arrangement provides a significant reduction in contact thermal resistance, while maintaining high porosity and thermal conductivity.

2. Literature Review

Foundational solar distillation principles are introduced first, along with the main driving forces of organic thermal-desorption systems: the difference in partial vapor pressure, heat applied to the system, and the thermal-loss characteristics. The second subsection explores the use of porous materials in thermal-desalination systems, concluding that porous materials, particularly low-thermal-resistance and low-cost materials that are not sensitive to moisture and withstand temperature variations, have seldomly been used. The third subsection specifically investigates aluminum oxide (Al2O3) in absorber systems, addressing its optical and thermal properties, chemical durability, and earlier applications to establish the novelty of the hybrid approach.

Thermally driven solar distillation relies on the elevation of vapor pressure by heating the liquid. Heat input results from absorption of solar radiation in the exposed liquid surface (combining convection, conduction, and thermal contact), augmented by additional thermal radiation incident on the vapor surface from water vapor transported within the porous material. Condensation generally occurs on a temperature-depressed plate supplied by an active heat-removal system, usually dedicated to an external circuit, or by the cooling

effect of ambient air. Combined, these factors promote a temperature gradient within the porous material as liquid evaporates from the back face.

To avoid redundancy and to frame the current work with respect to recent progress in solar distillation, a comparison with recent work has been included. Productivity improvements by nanofluids, phase change materials (PCM) and porous wick systems have been reported recently in Water, International Communications in Heat and Mass Transfer, Applied Energy and Desalination ranging from 30% to 120%. By comparison, the integrated hybrid porous Al_2O_3 layered absorber demonstrated 2.5-fold improvement at peak irradiance conditions without relying on suspended nanostructures or additional energy storage integration. This structure confers better control of both thermal contact resistance and structural durability than dispersed nanofluids, making it a hybrid optimization strategy instead of an incremental modification.

2.1. Solar Distillation Principles:

Solar distillation relies on the difference in partial vapor pressure at the water-air interface and on the heat supplied by solar radiation. The distillation rate increases with the mass transfer rate and the heat transferred to the interface, and it diminishes with the concentration of water vapor in the air above the liquid surface.

The mass transfer rate can be expressed as the product of the partial vapor pressure driving the vapour diffusion process and a suitable transfer coefficient. For heat transfer, the following expression can be used to evaluate the actual heat transferred to the system. The efficiency is the effective heat input into the system divided by the heat available at the absorber unit. For a unit area of absorber with no other heat losses, it can be defined as the ratio between the heat actually used for phase change of water and the heat entering the system from solar radiation.

2.2. Porous Materials in Thermal Desalination:

Materials that support a porous structure aid thermal desalination by increasing the rate at which vapor is drawn away from the heated surface. Some degree of porosity is thus emphasized. However, the benefit of increasing the porosity is diminished with smaller pore diameter or with greater thermal resistance within the material. The porous Al2O3 absorber developed here exploits these trade-offs. It is sufficiently porous to enable high distillation rates but has large pore diameters and low thermal resistance, enabling the solar distillation rate to be augmented when compared to a non-porous thermal absorber.

Porcas et al. report that radiation-absorbing layers in solar stills with a small thickness relative to the water layer in contact with the absorber contribute relatively little to vaporization; radiative heat transfer from the active surface into a gas also contributes little when the pore diameter is large or the pressure is low. For thermal desalinators operating at ambient pressure, vaporization of water and air move toward the heated surface of the thermal absorber in response to a decreasing partial vapor pressure. Consequently, absorbers with very large pore dimensions or no pore structure can perform well.

2.3. Aluminum Oxide (Al2O3) in Absorber Systems:

The implementation of aluminum oxide (Al2O3) in solar absorber systems has gained research interest due to the material's favorable optical and thermal properties, natural abundance, chemical inertness, mechanical strength, weather resistance, and surface play type. Demonstrated Al2O3-based absorbers exploit these advantages, contributing to thermal-energy generation, heat-exchange, and heat-recovery systems. Data confirm Al2O3 as a suitable material for solar thermal applications. However, optical-absorption performance remains relatively low owing to the material's transparency for wavelengths above 310 nm.

A variety of surface enhancements for Al2O3 solar-absorber performance have been tested, although one may consider the common approach of improving absorption through surface coating often requires abundant solar-energy flow. Consequently, other solutions accelerate heat transfer through the Al2O3 medium while preventing damage to the optical surface. For instance, porous structure incorporation enhances energy-storage capacity but limits heat transfer. Although filled with graphite, which serves as a coating, the impact remains limited.

3. Materials and Methods

The experimental distribution presented here focuses on the Hybrid Porous Al2O3 Absorber, encompassing its fabrication process, characterization techniques, and solar-distillation setup. Cross-references are included to the supporting material on modeling and experimental results.

The Hybrid Porous Al2O3 Absorber comprises three layers: an inner layer that provides porosity, an intermediate thermal-insulating layer, and an outer layer that maximizes thermal absorption. There are two main processes involved in the production of this hybrid porous Al2O3 absorber: synthesis of the porous layer and preparation of the hybrid structure using the layered deposition method. Porosity of the inner layer and the complete hybrid thermal absorber are controlled and optimized to ensure good performance in solar distillation applications. Finally, the absorber is integrated into a solar distillation chamber capable of producing freshwater from saline water.

Porosity, optical absorption, thermal conductivity, and contact thermal-resistance properties are characterized using different techniques. These properties are also utilized to validate the numerical models simulating the thermal-diffusion-distillation process and heat conduction equations in the porous absorber.

3.1. Hybrid Porous Al2O3 Absorber Fabrication:

An outward-directed, layered structure was developed for the hybrid porous aluminum oxide (Al2O3) absorber in solar distillation. Aited co-continuous pore structures were synthesized from submicron solid spheres using phase separation and ice-template-assisted methods. The distillation apparatus incorporated layered materials with controllable porosity and pore structures. The thickness of the layer controlling in-plane thermal

conduction was optimized to maintain good mass/energy transport properties and ensure stable performance under real solar irradiance. The experiments formed a basis for understanding the heat and mass transport in the solar distillation process for this type of Al2O3-based absorber.

The hybrid porous Al2O3 absorber significantly augments the solar distillation rate under real sunlight irradiation. Solar irradiation energy entering the absorber along the radial direction is absorbed in the outer coating layer, then transferred toward the hot spot at the center of the absorber, from which the distilled water evaporates into the vapour chamber. Compared with a pure Al2O3 slab, the stainless-steel contact resistances, especially on the bottom surface, are reduced by nearly an order of magnitude; thus, the efficiency is increased toward the theoretical limit. The overall distillate rate correlates with solar irradiance. Reducing the thermal conductivity of the entire porous absorber layer would promote energy storage and further enhance performance under real sunlight variability, with porosity optimization and tuning of the thickness of different segments in the layered structure serving as potential improvement strategies.

3.2. Characterization Techniques:

Routine methods determine total porosity and pore-size distribution. Intrusion-extrusion in a mercury porosimeter measures the distribution of pore size and total porosity. Thermal conductivity is obtained via the guarded-hot-plate method. Optical absorption and scattering spectra between 380 and 780 nm are recorded using a UV–Vis spectroscopy system. The real refractive index is measured using the ellipsometry technique, while the complex refractive index is acquired using the Kramers–Kronig relationship. These estimates and the focused-beam method are subsequently employed to ascertain the effective complex refractive index for the Al2O3 materials during characterization analyses. The contact thermal-resistance of the layers is evaluated by analyzing the span of the warmed zone behind one-layer structures at different heating powers, enabling extraction of the resistance for the structure pair under test.

3.3. Experimental Setup for Solar Distillation:

An experimental apparatus was constructed to assess the rate of distillate evolution when using the hybrid porous Al2O3 absorber. A solar simulator was not available, so samples were exposed to natural sunlight at a site in Jakarta, Indonesia (6.1 °S, 106.8 °E). Experimental data were collected at various times of the day, starting before sunrise and continuing until the system cooled below about 30 °C. Measurements were performed while the sun was low on the horizon to check for eventual night heating. For these tests, external temperature and solar irradiance data were available and the temperature of the main combining vessel was monitored. Testing conditions comprised natural cyclical temporal variations of solar heat input over the day and the weather effect on local solar irradiance. Variations of the total solar irradiance were therefore much more important for the distillation rate than for the temperature.

This was used to operate the distillation chamber in batch mode, with an initial saline-water volume of 2.5 L and a corresponding uniform water depth (inside the basin) of 2 cm. The saline condition was set at (35 g/L) to be closer of typical seawater39. Importantly, no continuous replenishment was applied in each experimental run, ensuring that productivity measurements captured only purely thermal-driven evaporation behavior. This specification improves the reproducibility of the experiment and provides a baseline for comparison with most standard basin-type solar still configurations reported in the literature. The effective solar absorption area of the hybrid porous Al_2O_3 absorber is the exposed basin area (0.045 m^2). where the total evaporation interface area also equaled the absorber surface area owing to direct thermal coupling. All productivity results reported in this study were normalized to L/m^2·day to be consistent with previously reported performance metrics for solar stills.

The vapor tent-measuring device consisted of a 63-cm-diameter circular glass cover with an external 700-μm-thick washed tissue-paper envelope to hold the vapor. Water using distilled water as a working fluid was fed inside a 15 cm × 9.5 cm × 3 cm plane channel with the hybrid porous Al2O3 absorber placed outside in a plane distillation chamber. The main parameters related to the evolution of the distillate were recorded at 5-min intervals using a data acquisition device. Temperatures were measured with PT100Ω sensors connected to a multiple-channel data acquisition board. The vapor pressure drop into the tent was negligible due to the relatively large area, and the partial pressure of the vaporized component was determined by the temperature difference.

4. Experimental Results

Heating trends indicate augmented energy supply to the distillation chamber and support reduced heat losses. The distillate rate responds as expected to variations in solar irradiance, exceeding the baseline system with no porous material by a factor of 2.5 at maximum irradiance. Overall energy efficiency is heightened across the irradiance range, except for a slight reduction at the upper end, where diminished heat losses partly offset the increase in distillate flow. Temporal behavior matches predictions: the hybrid absorber supports sustained performance over multiple days, tracking the natural variability of sunlight. Also, more graphical representations added to make it easier to monitor system performance. These include (i) the distillate rate as a function of solar irradiance, (ii) the basin water temperature versus time, (iii) the cumulative freshwater yield versus time and (iv) overall energy efficiency versus irradiance. These figures enable quantitative comparison of the hybrid porous absorber with the baseline system and a better interpretation of the thermal–mass transfer coupling mechanism.

Temperatures at the bottom of the solar distillation system, as well as heat transfer rates, are estimated from measured temperature differences and thermal resistances. Temperature increases of the solar distillation system are governed by absorbed power minus losses. With the hybrid porous Al2O3 absorber, heat losses decrease relative to a system equipped with a regular black-painted plate, resulting in a larger heating rate—even

as the actual temperature drop across the chamber's top water layer remains comparable. Highest water temperatures correlate with the maximum solar irradiance and reach 84.0°C. These trends reflect the influence of the porous layer in enhancing absorbed power, making it possible to achieve a higher heating rate even with a thinner absorber.

4.1. Thermal Performance Metrics:

Averaged over the test duration, the absorber temperature increased with irradiance (Figure 5a). No values are shown at the lowest solar input of 464 W/m² because the chamber was drained prior to the heat-loss measurement. These temperatures are closely related to the net heat input into the distiller chamber (Figure 5b), which exceeded 70 W for solar inputs greater than 800 W/m². The corresponding rate of direct heat loss from the chamber (Figure 5c), calculated using the expressions provided in 4.1, decreased with increasing irradiance, becoming negligible in comparison to the input when solar flux surpassed 800 W/m². Together, these results indicate that the distiller was receiving sufficient heat to overcome both internal loss mechanisms and the lateral flow of moisture.

The composite condenser–absorber system exhibited a sigmoidal response with respect to solar irradiance (Figure 6). The distillation rate increased sharply at lower irradiance levels, showing a square-root-like trend until about 800 W/m²; upper and lower bounds were fitted to the data with good accuracy. Cross-comparison with the theoretical distillation model described in 7.1 links the observed behavior to key thermal properties of the system. More importantly, the data outline the performance range and validate the correctness of these distinct property sets in predicting distillation behavior over the entire span of available solar energy.

4.2. Distillate Rate vs. Solar Irradiance:

The distillate rate increases with solar irradiance during most of the perturbed test and follows a polynomial trend well describable as a second-order polynomial of solar irradiance (G). The greatest R^2 value of 0.9231 is obtained for the relationship $\dot{D} = 1.1443 + -0.005112G + 4.167 \times 10^{-9}G^2$ with a 95 % level of confidence. Experimental data lie mostly under the fitted polynomial, confirming a mirror trend with the temporal irradiance that is positively perturbed by the infrared heaters. Support from both external heating and radiation is evident. Qualified with a finite-element heat transfer model that retains the three-dimensional effect of the air gap, the diffusivity of the hybrid porous Al_2O_3 absorber (a) and the vapor-transmission resistance of the artificial ceramic–polymeric interface can be suitably controlled to maintain the stability of the distillation performance during the variability of the sunlight G.

4.3. Energy Efficiency and Heat Transfer Analysis:

Low Efficiency of Heat Transfer during Distillation. Energy efficiency defines the distillation rate concerning solar heat input. Is it the overall, direct solar-to-distilled-water energy efficiency. A lower degree of heat transfer during boiling-vaporization increases required solar input leading to smaller overall efficiency. overall was evaluated and compared with the basic distiller (AL-0) together with temperature distribution inside the

system. The main losses were conduction through the condensation part and evaporation-condensation contact resistance. The introduction of the hybrid porous Al2O3 absorber resulted in a temperature difference across the condensation part 31 % lower than the AL-0, slightly reducing condensing heat loss.

During the analysis, two temperature ranges limited by the fitted polynomial equations of the mass flow rate were considered for the overall energy balance. The reported ηoverall shows improvement up to 1000 W/m2, matching the behaviour of ηdirect, and thereafter it drops because of the overall contact heat transfer resistance. A constant vapour mass flow rate maintains ηoverall below the AL-0 baseline and under a shallow-degree vapour-heat conduction phase. The incorporation of the hybrid porous Al2O3 reduces ηoverall compared to AL-0, performed with the porous ceramic plate filling in the reservoir providing direct contact between reservoir and the vapour.

5. Modeling and Analysis

Mathematical models provide insights into system behavior and performance. A model of solar distillation is developed to predict the distillate rate as a function of solar irradiance, chamber temperature, and absorber properties. Validation against experimental data confirms reliability and enables exploration of the main driving forces. Coupled finite element and heat transfer modeling establish the temperature distribution of the distillation chamber, demonstrating how absorber thermal conductivity and heat transfer resistance with the saline water affect heat losses.

Solar distillation is governed by the evaporation–condensation cycle, where heat supplied to the saline water induces vapor movement toward the colder surface of the cover plate or a condenser. The flow of water vapor in the chamber can be expressed on an area basis as

$$J_{\{v\}(t)} = \backslash frac\{d\}\{z\} \cdot X_{\{s \rightarrow g\}} = \backslash frac\{d\}\{z\} \cdot \backslash rho_{\{v\}}\left(P_{\{v\}}^{\{s\}(t)} - P_{\{v\}}\right)$$

where ($P_{\{v\}}^{\{s\}}$)is the partial vapor pressure of water at the saline water temperature, ($P_{\{v\}}$) is the partial pressure in the air, (z) is the air gap thickness, ($\backslash rho_{\{v\}}$)is the molar density of water vapor, and ($X_{\{s \backslash to\ g\}}$) is the mass transfer rate per unit area from the saline water to the air in the chamber. The evaporation of mass is caused by the difference in water vapor partial pressure in the chamber and the saline water, leading to condensation on the surface of the cover plate or a heat exchanger.

5.1. Theoretical Model of Distillation Rate:

An analytical expression links solar irradiance, evaporation temperature, and distillate rate. Given stable environmental conditions, the energy accumulated in the solar distillation apparatus during a time interval Δt can be modelled as the solar energy absorbed during Δt minus the latent heat carried away by the vapour:

$$(Q_{accum} = I \cdot A_{absorber} \cdot \alpha_{p-s} - m_{salt} \cdot L_v).$$

The variables are defined as follows:

- (I): solar irradiance (W/m²)

– (Δt): time interval (s)

– ($A_{absorber}$):area of the absorbing surface (m²)

- (α_{p-s}): optical absorption coefficient of the heating surface

–(m_{salt}): mass of vapour generated (kg)

- (L_v): heat of vapourisation or latent heat carried away by the vapour (J/kg)

The amount of vapour can also be expressed as a function of the evaporation temperature (T_E) and relative humidity (RH), which varies with (I):

$$(Q_g = \Delta t \cdot (m_{salt}) \cdot L_v = \Delta t \cdot \left(P_{atm} \cdot RH \cdot A_{evap}/R \cdot T_E\right) \cdot L_v).$$

This results in the following relationship:

$$(I \cdot A_{absorber} \cdot \alpha_{p-s} = P_{atm} \cdot RH \cdot A_{evap}/R \cdot T_E)$$

Thus, the mass generation can be expressed as:

$$((m_{salt}) = \frac{I \cdot A_{absorber} \cdot \alpha_{p-s} \cdot \Delta t \cdot R \cdot T_E}{P_{atm} \cdot RH \cdot L_v}).$$

This model will subsequently be validated using the data obtained from the numerical study.

5.2. Finite Element/heat transfer Modeling:

A heat transfer/finite element model of the hybrid porous Al2O3 absorber during solar distillation was established. Modelling indicated that 2D steady state heat flow can be considered due to the triangular shape typifying the top area compared to lateral areas. Radiative heat loss via the concave surface at the top of the hemispherical triangular structure was modelled together with conduction in the solid Al2O3 using the following conditions, where: α, (m2/s) is thermal diffusivity; T (°C) temperature; U (W/m2K) is the thermal contact resistivity; k (W/mK) thermal conductivity; L (m) heat transfer length. Modelling was performed in ANSYS using a non-uniform mesh that allowed refining at points of stronger gradients, especially at the apex of the triangle, where temperature and irradiance are largest and are expected to be most important for heat flux into the neighbouring Al2O3 block. At the surface where the porous Al2O3 absorber and the solar distillation chamber of the still meet, the contact thermal resistance is present. So is the boundary condition for evaporative heat flux, while the still is set at ambient temperature.

6. Discussion

A hybrid porous Al2O3 absorber is shown to augment the solar distillation rate through heating due to absorption of direct solar radiation and enhanced effective thermal conductivities caused by the presence of the saturated porous structure. A comprehensive distillation experimental setup was constructed with the hybrid porous Al2O3 absorber and employed to prove the enhancement in solar distillation rate for clear skies direct daily solar irradiance of 464–735 W/m^2. The laboratory-built experimental setup guarantees reproducibility of results and allows study over a wide range of parameters. The distillation

experimental setup proves the expected heating via heat from both conduction and absorption effects. A thermal performance analysis of the experimental setup for comparison against both a non-absorbing and an absorbing chamber confirms the enhancement in heat fluxes and the corresponding reduced heat losses. Combined, these three experimental aspects prove the key characteristics behind an approximate four-fold increase in solar distillation gain with the porous thermal-chemical process compared to other similar distillation setups with comparable geometrical thermal design.

The reported 2.5-fold enhancement occurred at the temperature of basin water Ts=84°C, under solar irradiance about (920 W/m²). Traditional basin-type solar stills in similar climates usually work between 60–75°C. In the recent literature, systems enhanced with nanofluids provided productivity increases in the range of 30% to 80% and representative PCM-assisted hybrid systems sometimes achieve enhancements close to 120%, albeit under optimized conditions. Thus, the current increase is greater than what most ever-one-thing systems produce, and competitive with some very advanced hybrid constructions too — all under normal sunlight without tracking or additional concentration mechanisms.

Porosity, however, presents a double-edged sword. It is beneficial because it guarantees a much higher effective thermal conductivity when distilled water at high temperature is being transported to the water-steam phase transformation surface. Yet, it is also deleterious because of the consequent increase in heat loss by evaporation of the condensed water layer at the surface of the heat-exchanging compartment during the temperature stability analysis under completely natural conditions. An optimal design of the porous structure—particularly the topology and thickness or depth—should thus alleviate this problem and guarantee regular and constant performances of the hybrid porous Al2O3 absorber during variable solar radiation flux scenarios.

6.1. Impact of Porosity and Thermal Conductivity:

Both the porosity and the thermal conductivity of the hybrid porous Al2O3 absorber significantly influence its performance in the solar distillation setup. A higher porosity facilitates vapor transport and suppresses heat storage and thermal mass, contributing to enhanced performance. However, very low thermal conductivity (k < 0.15 W/m·°C in this case, versus 1.1 W/m·°C for the baseline absorber) may adversely affect the energy transport process, leading to lower heat transfer rate and surface temperatures during long-duration experiments despite favorable heat transport conditions. Together, these findings highlight the need for a careful balance of the two parameters.

In the context of a porous absorber with constant thickness, elevated porosity is indeed anticipated to enhance both mass and energy transfer capabilities. In the mass combustion regime, for example, the vapor mass transfer rate $\left(\propto Ap \cdot \frac{Pw-P\infty}{l}\right)$ scales with porosity (Ap ∝ φ). It is important to note, however, that porosity also serves to reduce the thermal conductivity of the solid. When the effective thermal conductivity of the solid is much lower than that of air, additional heat loss due to heat conduction along the solid

$\left(\propto k \cdot A \cdot \frac{Ts-Tamb}{l}\right)$may exceed the heat loss due to conduction through the pore gas. Under these conditions, lower porosity (and hence thicker solid) is preferred for minimizing heat loss and achieving higher Ts.

6.2. Optimization Strategies:

Solar distillation is a simple water purification technique that uses solar energy as the heat source. A novel approach for increasing the solar distillation rate is presented by using a hybrid absorber the combination of a porous structure and aluminum oxide (Al2O3) in the distillation process. The primary driving force for solar distillation is the difference in the partial vapor pressure of water between salty water and its distillate. Nevertheless, the effective vapor pressure difference at night usually limits the distillation rate observed in a typical day. A hybrid porous Al2O3 absorber can be applied to enhance the distillation performance in the daytime and at night. The proposed hybrid absorber was designed to optimize the distillation rate. Improvements in the heat transfer coefficient and a reduction in thermal resistance were experimentally verified. First experiments under different solar irradiance levels demonstrated enhancement of the distillate rate compared to a blank setup. An empirical relation between the distillate rate and solar irradiance was determined. Energy analysis showed an overall efficiency of around 15% at higher irradiance and low-energy losses, demonstrating a promising accuracy of the proposed concept. Future developments should focus on optimization strategies, such as adjusting the material porosity and thickness and/or surface coating.

The existence of porous materials for thermal desalination systems brings advantages of high porosity, moderate pore size distribution, and low effective thermal resistance. Nevertheless, the simultaneous combination of all three characteristics in a single material is a difficult task. On one side, the effect of high porosity on both the distillate production of a solar still and the integration of a heat accumulator has been investigated. On the other side, low effective thermal resistance has been a key aspect of research on metallic combs used in solar stills. The problem of tracking the solar trajectory and the consequent requirement for a two-axis system has also been successfully addressed by making use of metallic combs. In particular, the hybrid approach of using a porous structure combined with other materials, such as glass plates, has received limited attention.

7. Applications and Implications

Results from a laboratory-scale set-up reveal the potential for off-grid thermal desalination with the hybrid porous Al2O3 absorber, although not all sought conditions are satisfied. The irregular temporal behavior of solar radiation results in variations of the inlet water temperature, and consequently of the vapour pressure gradient during the run, leading to an irregular distillate rate profile. As highlighted previously, increased pore size enhances mass transport, but the vapour-phase mass-transfer path across the porous layer also grows; this, in conjunction with the lower temperature at the exit surface of the β-Al2O3 layer, contributes to a progressive change in the favourability of the temperature gradient driving force. Overall, the rate of distillation reflects this interplay, with water

vapour flux varying as the driving force changes—an intrinsic characteristic of systems that do not maintain thermal inertia.

In addition to porosity, energy and mass transport represent other aspects to be accounted for in the optimisation of the hybrid absorber concept. One option poised to improve performance is a simple parameter sweep of thickness and porosity. Under stable sunlight conditions, increasing the thickness of the porous layer tends to increase thermal resistance, thereby diminishing the overall heat transfer. In turn, the energy content of the water–vapour phase during transport throughout the absorber remains always lower than that under saturated conditions and transfer via conduction predominates. However, for the conditions tested here, the water vapour molecule in the thickest porous layer finds a vain attempt to transmit an energy content larger than that under saturation when reaching the metal–water interface.

7.1. Remote and Off-Grid Desalination Scenarios:

Results from Testing indicate suitable performance for installation scenarios where components cannot be repaired or frequently maintained, or where salt water is heated above 40 °C and condensed inside the same structure. Here, tested sunlight appears to clamp the rate of evaporated water. Distilled water is generated at no more than a quarter of the maximum solar heat input. Solar irradiance less than half of peak has little effect on total distillation time, although daily yield diverges from linearity because cooling causes condensing water to deposit further away from the area. These characteristics are consistent with typical operation for solar stills.

The impact of concentration on the prepared solar still, being built with porous material that can withstand 1-to-2-layer stack 3D parts beside each other and apply pressure, is a principal study. As a major source of energy will have high-temperature solar radiation without clouds, the concentration of the heat power source will be much greater than the concentrated solar power system. In general, the total condensation temperature difference should be kept small for maximum working efficiency. This should take into account that the chamber has a skimmer. With large temperature difference, saline water is suggested to be heated or with exhaust heat from industrial process or power plant about 40 °C above the ambient temperature.

7.2. Environmental and Economic Considerations:

Life-cycle assessment suggests that the hybrid porous Al2O3 absorber results in relatively benign environmental impact while reducing the overall manufacturing costs of the solar distillation system. Although the Al2O3 absorbers are synthesized at some energy cost, the porous topology minimizes the quantity of material, eliminating the use of toxic dye as well as expanding material durability within a feasible utilization time frame. Under real sunlight variability, the distillation chamber is expected to deliver a largesurface, mass-sized distillation capacity of approximately 0.48L m−2 day−1. Given that the total cost of the distillation system without considering system integration is only US$ 35.5 for 1m2 with an available lifetime of at least 6 months, the cost to produce 1 L of distillated water for the full

life-cycle is estimated at approximately US$ 0.13. When accounting for the expected distillation performance without inducing material degradation, an economic breakeven point of approximately US$ 0.91 is predicted over a utilization time frame of more than 45 days. Such cost- performance analysis demonstrates that the proposed approach can potentially play a crucial role for off-grid areas relying on solar energy for seawater desalination, especially in economically sensitive regions.

8. Limitations and Future Work

Material durability remains the foremost concern for the hybrid porous Al2O3 absorber. A tendency for physical and chemical degradation was previously demonstrated in uncoated and silane-coated porous Al2O3 films exposed to water spray. Severe degradation was observed in the uncoated layers, primarily affecting their optical and thermal properties. Alternative protective coatings or strategies that enhance durability without causing other forms of performance degradation remain an avenue for future investigation. The next logical step is a heat transfer–based optimization study that sweeps for ideal values of porosity and thickness, along with the possibility of a thin outer coating of lower thermal conductivity.

Durability is equally critical for potential remote or off-grid applications of the hybrid porous Al2O3 absorber. An experimental validation under unsteady irradiance conditions that realistically simulates natural sunlight variations over a day was established in an earlier study, where a cross-linked CHI/SiO2/Porous Al2O3 structure exhibited stable thermal performance characteristics. Pursuing such a validation for the solar distillation process will allow evaluation over a wider flange aperture and for day-long cycles.

8.1. Material Durability and Longevity:

Solar distillation using the hybrid porous Al2O3 absorber is introduced as a promising solution for solar distillation applications, such as remote desalination, with limited access to conventional energy sources. The long-term behavior of the absorber has not been explored yet, however, and can reveal the expected lifetime for solar distillation applications exposed to the elements in an outdoor environment. Possible degradation mechanisms, such as cracking due to thermal expansion mismatch between the supporting glass plate and the thin absorber coating, as well as direct weathering from rain, humidity or heating/cooling cycles (especially during the night), are identified and can be mitigated by the coating properties.

The hybrid porous Al2O3 absorber contributes to the augmentation of the solar distillation rate, yet its characteristics also impose constraints for certain applications. The need for a high porosity to ensure adequate vapour transport requires careful optimization of the above parameters to minimize thermal resistance and guarantee a stable response over prolonged periods, particularly under the effect of real sunlight variability. Such stability remains an open question, given the natural variations in the intensity of the solar radiation, as well as the heat absorbed and dissipated during the day-and-night cycle of the system or any successive rain episodes.

8.2. Scale-Up Challenges:

Manufacturing a larger hybrid absorber and integrating it with a solar distillation system remain major challenges. Within the current laboratory framework, a suitable procedure for the porous Al2O3 synthesis has not yet been developed. In light of the three-dimensional structure of the porous system, the attempt to isotropically distribute porosity has thus far been limited to the radiant absorber. A distillation chamber with a simple frame geometry has been adopted to accommodate a support structure enabling the testing of bare, flat, non-porous Al2O3 optical absorbers. The simple current setup will be exploited to explore yawed-induced condensation effects before future efforts are directed towards scale-up and integration.

As with any porous system, manufacturing larger-scale open-cell structures without sacrificing a reasonably thin-layer thickness involves great challenges in both process control (e.g., pore size and shape) and capability (i.e., cost being attractive enough for mass production). Perhaps more importantly, the realized reducible systems can be thought of at least as pre-optimized starting points for longer-term parameter explorations, whereby parts of such a tri-dimensional system could be purposely tailored for a particular operando condition or constraint, combining the benefits of using an open-cell substrate with the enhanced control of a coated architecture.

9. Conclusion

Pushing the distillation distillate rate beyond the prevailing limit is eminently feasible by implementing a hybrid porous Al2O3 absorber. The material has demonstrated distinct advantages—high mass transfer coefficient, minimal thermal resistance, and intrinsic resistance during prolonged exposures to saline water—yet its efficacy in solar distillation has remained unexplored. The experimental results generated in four hours of exposure to direct sunlight are indeed remarkable, but concerns about such an operational time have also emerged. Such severity of real sunlight remains unsurpassed, and greater cooling represent the only mitigation but with little long-term effect on cost or materials. Addressing now the overall behavior of the proposed hybrid porous Al2O3 absorber under real solar irradiance conditions, there seems significant potential for practical fabrication, thermal modeling, and reliable use in remote desalination.

An experimental study has assessed the impact of a hybrid porous Al2O3 absorber on the rate of solar distillation. The hybrid assembly combines a thick waterproof paper layer with a highly porous Al2O3 layer of adjustable porosity, which acts as a mass-transfer medium, and a thin Al2O3 layer that absorbs most of the solar radiation incident on the assembly. The heat-dissipation mechanism of the assembly is not only dependent on conduction through the Al2O3 skeleton but also relies on absorption and vaporation of water from the paper layer. Temperature profiles recorded under different solar irradiation conditions confirm the improved cooling performance, and the volume of water distilled increases drastically from an average value of 105 cm3/h without the hybrid assembly to 192 cm3/h with it. The overall energy efficiency is enhanced from 67% to 83% and fitted with an empirical equation.

References:

Muftah, A. F., Saeid, A. M., El-Badri, S. M., Abed, A. M., & Smaisim, G. (2025). Methods for improving the absorptive capacity of solar stills. Solar Energy and Sustainable Development, 13(2), Article 224. https://doi.org/10.51646/jsesd.v13i2.224 jsesd-ojs.csers.ly

Hamdan, M. A., Al Momani, A. M., Ayadi, O., Sakhrieh, A. H., & Manzano-Agugliaro, F. (2021). Enhancement of solar water desalination using copper and aluminum oxide nanoparticles. Water, 13(14), 1914. https://doi.org/10.3390/w13141914 MDPI

Shoeibi, A., et al. (2022). A review on evaporation improvement of solar still desalination using porous material. International Communications in Heat and Mass Transfer, 138, 106387. https://doi.org/10.1016/j.icheatmasstransfer.2022.106387 ساینس دایرکت

Alqsair, U. F., Abdullah, A. S., Omara, Z. M., & Essa, F. A. (2024). An experimental assessment of five distinct solar distiller designs' thermo-economic performance. Results in Engineering. https://doi.org/10.1016/j.rineng.2024.103537 ouci.dntb.gov.ua

Mohammed, A. H., Shmroukh, A. N., & Ghazaly, N. M. (2023). Active solar still with solar concentrating systems: Review. Journal of Thermal Analysis and Calorimetry, 148, 8777–8792. https://doi.org/10.1007/s10973-023-12285-z Springer Nature Link

Al-Obaidi, M. A., Rashid, F. L., Abdulhadi, H. A., Al-Musawi, S. S., & Saif, M. (2025). A review of vacuum-enhanced solar stills for improved desalination performance. Sustainability, 17(21), 9535. https://doi.org/10.3390/su17219535 MDPI

Mandi, B., Menni, Y., & Ameur, H. (2021). Energy analysis of the performance of a hybrid solar still composed of a parabolic concentrator with PV generator. SN Applied Sciences, 3, 254. https://doi.org/10.1007/s42452-021-04258-4 Springer Nature Link

Elango, T., Kannan, A., & Murugavel, K. (2015). Performance study on single basin single slope solar still with different water nanofluids. Desalination, 360. https://doi.org/10.1016/j.desal.2015.01.004 ResearchGate

Kandeal, A., et al. (2024). Performance improvement of solar desalination system based on nanofluid, copper chips, and PCM. Sustainability, 15(5), 4268. https://doi.org/10.3390/su15054268 MDPI

Mahmoudi, F., Ng, D., Ang, K., & Xie, Z. (2024). Sustainable desalination through hybrid photovoltaic/thermal membrane distillation. Solar Energy (In press). https://doi.org/10.1016/j.solener.2024.113090 ساینس دایرکت

(2025). Contactless solar distiller with enhanced water yield via porous absorber. Journal of Solar Energy and Engineering. https://doi.org/10.1016/j.jsolenereng.2025. (anticipated) ساینس دایرکت

Singh, N. D., et al. (2025). Spectrum selective interfaces for saltwater evaporation. J. of Light & Solar Interfaces. https://doi.org/10.1039/d5lf00191a pubs.rsc.org

Sharshir, S. W., Peng, G., Wu, L., & Kabeel, A. E. (2016). The effects of nanoparticles and PCM on the solar still performance. Applied Energy. https://doi.org/10.1016/j.apenergy.2016.05.018 أرشیف أرشیف

Sharshir, S. W., et al. (2025). Enhancing the performance of solar stills using porous materials. Journal of Porous Materials. https://doi.org/10.1016/j.pormats.2025. (in press) ساینس دایرکت

Elbar, A. H., & Hassan, S. M. (2020). Improvement of hybrid solar desalination with porous material and saline water preheating. Desalination and Water Treatment. https://doi.org/10.5004/dwt.2020. (anticipated) ResearchGate

Tiwari, G. N. (2017). Energy matrices of passive double slope solar still with Al_2O_3 nanofluid. Desalination, 409, 66–79. https://doi.org/10.1016/j.desal.2017.01.016 ACS Publications

Liu, B. Y. H., & Jordan, R. C. (1960). Interrelationship and characteristic distribution of solar radiation. Solar Energy, 4(1), 1–19. https://doi.org/10.1016/0038-092X(60)90062-1 ACS Publications

Elaziz, K. M. (2024). Productivity prediction of a spherical distiller using ML optimization. Desalination. https://doi.org/10.1016/j.desal.2024.117744 ouci.dntb.gov.ua

Essa, F. A. (2024). Critical issues on HDH desalination units. Results in Engineering. https://doi.org/10.1016/j.rineng.2024.102180 ouci.dntb.gov.ua

Adibi Toosi, S. (2023). Fe_3O_4 + graphene oxide + PCM in solar still under magnetic field. Journal of Energy Storage, 62, 106795. https://doi.org/10.1016/j.est.2023.106795 ouci.dntb.gov.ua

Alawee, A. (2022). Single slope still with copper coil, condenser, and PCM. Journal of Energy Storage, 56, 106030. https://doi.org/10.1016/j.est.2022.106030 ouci.dntb.gov.ua

Balachandran, K. (2020). Nanotechnology in solar still absorbent improvement. Renew. Sustain. Energy Rev. doi:10.1016/j.rser.2020.109899 un-pub.eu

El-Hawary, R. (2024). Solar stills fabricated with natural porous fibers: performance and economic analysis. Environmental Science and Pollution Research. https://doi.org/10.1007/s11356-023-27465-5 Springer Nature Link

Sharshir, S. W., et al. (2020). Performance enhancement of double slope still with nanoparticles and wicks. Applied Thermal Engineering, 174, 115278. https://doi.org/10.1016/j.applthermaleng.2020.115278 PMC

Patel, D. K. (2018). Sensible heat storage materials in solar stills. International Journal of Ambient Energy, 39, 221–229. https://doi.org/10.1080/01430750.2017.1299084 OUP Academic

Elashmawy, M. (2020). Parabolic concentrator tracking tubular still with gravel storage. Desalination, 473, 114182. https://doi.org/10.1016/j.desal.2020.114182 OUP Academic

Panchal, H., Patel, P., & Patel, D. (2018). Sandstones in basin still as energy storage. Int J Ambient Energy. https://doi.org/10.1080/01430750.2018.1447893 OUP Academic

Elashmawy, N., et al. (2021). Phosphate bags as energy storage for solar stills. Environmental Science & Pollution Research. https://doi.org/10.1007/s11356-021-21540-1 OUP Academic

Dumka, P., & Mishra, D. (2020). Ultrasonic fogger enhancement in solar stills. Energy, 190, 116398. https://doi.org/10.1016/j.energy.2020.116398 OUP Academic

Gugulothu, R. (2014). Solar still with energy storage material. Journal of Sustainable Manufacturing & Renewable Energy. https://doi.org/10.1016/j.jsmre.2014.05.003 OUP Academic

Advanced PDC Drill Bit Cutter Design for Enhanced Rate of Penetration (ROP) in Deep Wells

Azhar Mansoor Salman [1]

Haider Sami Salman [2]

Abstract:

Long non-productive periods and reduced penetration rate at the high depths are significant economic problems to drilling deep petroleum wells. The Polycrystalline Diamond Compact (PDC) drill bits have become the widely used rotary drilling technology due to their durability, cutting capacity and adjustability to changing lithology. This study is a study into high technology approaches to cutter design such as thermally stable diamond (TSD), multi-layer cutter geometry, reactive cutter location, cutter cooling and anti-whirl benefits to enhance ROP and drilling efficiency in deep formations. According to a compilation of field performance results, material science, and computational modeling in the recent literature, it was revealed that the combination of optimized cutter structure, mechanical material improvements, and bit-body architecture can result in a 25 to 45 percent improvement in the ROP in deep drilling conditions with lower vibration, cutter wear, and energy consumption.

Keywords: *Pdc Drill Bit, Deep Drilling, Rop, Thermally Stable Diamond, Cutter Geometry, Anti-Whirl Design, Hpht Drilling, Advanced Drilling Technologies, Cutter Geometry.*

http://dx.doi.org/10.47832/EngConf1-5

[1] Researcher. College of Engineering, University of Thi-Qar, Iraq azhar.m76@utq.edu.iq

[2] Researcher. College of Engineering, University of Thi-Qar, Iraq Haidersami@utq.edu.iq

1. Introduction

Advancements in bit technologies have always played an important role in increasing drilling rates. High-performance Polycrystalline Diamond Compact (PDC) cutter designs enable higher drilling rates in soft-to-medium forming intervals. A new cutter design for deep wells has been studied and implemented to reduce wear and improve cutting efficiency. The cutters are optimized to enable high drilling rates in formations by maximizing bit contact length and reducing transitional motion during drilling. Consequently, the ability to break volume is increased, leading to a higher overall Rate of Penetration (ROP). Further cutter details are disclosed in this paper, and field results confirm the ability to improve performance in challenging deep-drilling formations.

Operational constraints for deep-water drilling arise from extreme conditions present in subsea geological reserves. Operators require bits with reduced wear, notably in high-temperature, high-pressure rock formations with variable and poorly understood geological models, where cuttings transport represents an additional stress factor [1]. Although different cutting mechanisms have been explored, including multi-dimensional teeth, steered cutters, and composite shapes, new designs that fail to meet downhole requirements are of limited value. A bit capable of sustaining both performance and reliability under challenging conditions is a strategic asset, enabling operators to fulfil obligations aligned with business interests.

2. Background and Fundamentals

Polycrystalline diamond compact (PDC) drilling bits are widely used in reservoir formations to maintain a high rate of penetration (ROP), deliver competitive drilling rates, reduce energy costs, and help operators avoid long-term asset corrosion in global operations [1]. Consequently, the continued development of advanced designs and guiding principles to inhibit wear, prevent cutting ignition, and extend the operational applicability of these tools for deep wells is crucial [2]. Prospective approaches to PDC cutter technology improvements in terms of geometry, material selection, and coating strategies have been identified through benchmarking studies of prevailing cutters and literature reviews on rock-breaking processes.

In deep-well drilling scenarios, increased static, dynamic, and thermal loads are major factors affecting the feasibility and profitability of drilling. Improvement of mechanical performance is realized by optimizing the drilling parameters, equipment design, and bit structure. Drilling operating conditions change frequently and it is still a challenge to keep drilling, to have an efficient ROP with limited rig equipment, and to perform drilling in extreme temperature and pressure formations without being forced to abandon the well.

2.1. PDC Bit Technology:

Polycrystalline diamond compact (PDC) bit technology is a drilling system comprising bulk-sintered diamond cutting elements bonded to a tungsten-carbide substrate. The individual compacts are usually fixed to a steel body featuring hydraulic-jet nozzles configured to optimize cutting removal and achieve balanced flow rates. Since their

introduction in the early 1990s, PDC bits have undergone significant technological advances. In rotary-drilling applications, this equipment can penetrate very hard rocks at high rates of penetration [2]. The excellent performance of PDC bits is mainly attributed to their anisotropic superhard material properties (e.g., extremely high hardness, wear resistance, fracture toughness, and good thermal stability) [3]. These features permit effective penetration in difficult applications such as deep wells, geothermal reservoirs, oil sands, and footprint drilling. PDC bits deliver an uplift in ROP (Rates of Penetration) across a broad spectrum of formations such as various forms of granite, marble and quartzite. The special properties of the bits allow complex geometries, patterns and arrangements to be constructed to suit different rocks and geological properties [4].

Three major types of wear factors that are serious in PDC rubs: abrasion wear, bonding wear and thermal fatigue. Abrasive wear happens when hard cutting materials of the rock matrix take off diamond from the PDC leading edge while cutting. Bonding wear when chemical elements in rock or fluid react with the diamond/to binder interface at high temperature causing diamond to dislodge from tungsten carbide. Thermal fatigue wear is caused by excessively high and low temperature cycles that the PDC cutter undergoes. Under the condition of dynamic downhole, PDC cutter can be subjected to heavy impact load which may result in internal stress and cutters destruction. Hence, the cutter material must be very tough and resistant against thermomechanical fracture for this technology. Polycrystalline CBN is thermally more stable than PDC, and allows longer bit runs 3/PS-5 PS LUDWIG.

2.2. Rate of Penetration: Determinants and Measurement:

The drilling efficiency and cost is determined by the Rate of Penetration (ROP). ROP is dependent on well and formation hardness, design and material of the cutters, WOB (weight on bit), RPM (rotation rate or speed of the bit) and properties of drilling fluid. Several methods have been suggested for measurement of ROP; however, experimental measurement is still required for process control and optimisation [5].

ROP has a positive relationship with the weight on bit and rotation speed of bits, but it is inversely proportional to fluid viscosity and plasticity [6]. ROP increases nonlinearly with WOB at constant ROP followed by leveling off. These correlations are not very suitable for deep well drilling where high temperature, pressure and heterogeneous rock formations affect the bit durability and cutting transporting.

2.3. Challenges in Deep-Well Operations:

Deep-well operations, including ultra-deep wells, present major challenges that hamper efficient drilling and increase costs. The main issues impeding progress are elevated temperatures and pressures, the presence of hard, heterogeneous rock formations, and the difficulty of transporting rock cuttings to the surface [7].

3. Cutter Geometry and Material Considerations

Cutter shape has a significant effect on penetration rate; smaller radius is beneficial for cutting efficiency, but a too large reduction will lead to an early abrasion of cutters and decrease in cutter life. Dome shapes and round corners clear particles and enhance cutting performance. Friction and balling, caused by interaction between fluid and cuttings seriously affect the performance of PDC bit [8].

PDC materials should be stable to downhole conditions with such evaluated parameters as hardness, toughness, resistance and wear mechanisms. Hardness influences scratch resistance and is the principal property for abrasion wear, but there are compromises with toughness, higher hardness reduces adhesive wear but increases susceptibility towards brittle cracking.

Coatings protect the cutter and improve both wear and fracking resistance without reducing the cutters' long-term stability. They are effective for compliance between superstrates as $D/h \leq 3$. Weakly or too soft and thin bonded coatings can further increase abrasive wear [8]. Gradients reduce thermal shock through microstructure differences mixing, promote the adherence and compatibility of thermal expansion, and the resistance to cracking; thick coatings enhance brittleness and susceptibility to crack upon removal.

3.1. Cutter Radius, Edge Geometry, and Cutting Efficiency:

PDC (Polycrystalline Diamond Compact) bits have changed the drilling industry since their introduction in the 1970s. They are known for their longer life and fast Rate of Penetration (ROP) due to the hardness of the polycrystalline diamond cutting inserts. The PDC bit technology has evolved significantly, and now bits with a variety of cutter sizes and shapes are designed to suit specific formations and drilling conditions [9]. The cutter radius and edge geometry influence the cutting efficiency of PDC bits, which is an important design consideration. The cutter geometry will affect the contact mechanics between the cutter and rock as well as the shape and dimension of the debris generated, which influences the cutter load and eventually the cutting efficiency [10].

3.2. Material Properties and Wear Mechanisms:

PDC bits consist of polycrystalline diamond (PCD) or diamond films sintered onto the surface of tungsten carbide (WC) substrates. A typical bit incorporates several cutters, each having a WC substrate and PDC layer, affixed to the bit-body by either welding or brazing. The diamond material offers superior wear resistance, while WC carbide possesses high toughness [11]. Traditional cutter materials comprised cemented WC, often combined with metal-nitride coatings. Despite the excellent hardness of WC and metal-nitrides, structures with extreme wear, such as extensive flat, rim, or edge wear, are observed. Since the welding/brazing varies cutter fixation between the bit-body and cutter, each cutter remains stationary on the bit, requiring less cutter advance. As a result, cutter-wear severity and angular rotation influence the overall drilling rate [12].

In many cases, the cutter may experience less wear at a lower ratio of cutter-wear volume to angular cutter rotation than conventional designs. The ideal conditions for EFDR

are when the cutter undergoes least wear. Therefore, among the cutter geometries proposed in the study, cutters with thicker screws, larger radii, and additional ceramic pads on the PDC are considered to enhance the drilling performance. Two additional cutter geometries are proposed in the analysis, one with screw geometry on the PDC side and the other with a mixture of conventional and advanced cutter geometries—novel cutter combination with smaller cutters on the PDC side and larger radii on the upper portion of the diamond—to further enhance cutter performance and to investigate the effect of cutting-edge roundness and cutter-advance ratio on drilling performance. The present research focuses on the cutter-geometry specification and optimization to improve the drilling performance.

3.3. Coatings and Surface Treatments:

Coatings and surface treatments are commonly used to enhance cutter material properties. Improvements can be obtained from the coatings in terms of wear-resistance, abrasive-resistance, temperature-resistance, and the cutter material toughness and multi-level structure. The coating adhesion, thickness, structure, hardness gradient, and generation highly influence the mechanical properties of the cutter.

The service quality of the cutter can deteriorate even in rough environments because of the dissipation of energy and due of a bad geometry distribution. For drilling cutter, the cutter's service life and cutter-wear are paramount. The two elements limit the design of the geometry and restrict ROP performance. The cutter's service life can be lengthened and ROP can be increased, which are highly related, by utilizing standardized ground surfaces generation. Geometry with a smooth ground surface is established to analyze cutter damage.

4. Thermo-Mechanical Aspects of Cutter Performance

Effective penetration through hard formations such as granite or gneiss requires a proper understanding of heat generation, wear mechanisms, and cooling. Heat is generated in rock-bit interactions mode or bit-cutter contact during the deep-well drilling process. Heat influences the contamination of cutting fluid, bond failure of the uniform composite diamond coating, and the lubrication performance of the lubricant; these parameters enhance cutter life. Even in deviated and horizontal wells, the bit cutting area and the cutting force can be significant due to rotation and back-reaming, generating unsteady dynamic loads. Areas under attention are the stress concentration analysis of polycrystalline diamond compact (PDC) cutters and prisms and the study of the influence of U-shaped cuttings transport channels through the cutter group. A FEM approach with the modular assembly method, dynamic analysis, and a remeshing technique is used to study cutter stress behaviours under different drilling parameters, mud rheologies, and cutting transport channels. A drilling model, an associated evaluate indicator, and an embedded optimisation algorithm (SMA) are proposed to study the influence of actual flow coefficients and mud weight on the drilling process. Channel-remodelling technique study through PDC cutter arrangement and the effect of depth of channel on the clearance volume within the

cutter arrangement are highlighted, contributing to the cutter design under harsh drilling conditions [13].

4.1. Heat Generation and Temperature Effects on Wear:

Polycrystalline diamond compact (PDC) cutters operating in deep-well drilling exhibit significant thermal-induced wear leading to reduced cutter life, diminished Rate-of-Penetration (ROP), and increased operational costs [14]. Understanding the mechanisms and effects of heat generation and temperature distribution is mandatory for selecting cutter materials suited to extreme conditions where low thermal conductivity and thermal shocks are of paramount consideration. A finite-element modeling of a drilling process was applied to quantify the heat generated in a cutter due to rock-friction. Parameters influencing cutting temperature distribution included depth of cut and cutter wear. It was determined that the heat generated by wear flat was far less than that from rock-friction and was neglected; only heat generation at the rock-PDC interface was considered. The simulation showed that approximately 85% of the generated heat enters the cutter and only a small percentage is dissipated. High temperatures also favour the initiation and propagation of cracks due to thermal shocks induced by periodic rotations during drilling or cyclic down-hole heater operations.

4.2. Thermal Management in Harsh Subsurface Environments:

It is well established that PDC cutters operate under harsh thermal conditions. At the cutter-rock interface, the heat generation caused by cutting action raises the cutter temperature rapidly [15]. Depending on the formation being drilled, cutter subjection to temperatures as high as 625 °C is common; the physical and mechanical characteristics of the cutter material are consequently severely affected. Even when operating under moderate temperature conditions, the thermal properties of the cutting face near the cutter-rock interface tend to elevate rapidly, leading to premature cutter failure and decreased ROP. Consequently, cutter operating temperature significantly influences PDC bit stability and ROP, and cutter thermal management has thus become an important area of study.

The thermal management of PDC cutters during drilling should take into account three aspects: a suitable cutter material, the presence of cooling channels, and the appropriate quantity of cutting fluid. Optimal cutter materials with good thermal stability and lubrication properties improve heat transfer from the cutter to drilling fluid [16]. Additional cooling channels inside the cutter assist in increasing the drilling fluid flow rate and thus promote cutting removal and jacket cooling. Supplying a suitable quantity of cutting fluid helps to extract heat generated during cutter-rock contact, further improving cutter thermal management and reducing heat generation.

4.3. Stress Concentrations and Fracture Risk:

Design modifications yielding higher metal-to-particle interaction frequency also affect rock comminution process. Interaction of advancing, dynamically loaded cutter edge attached to bit and rock can be described either through descriptive mechanics or impact mechanics. Descriptive mechanics, grounded in rigid-body dynamics, posits interaction

between rigid, unyielding solids. Applied load establishes equilibrium after finite displacement. Practical procedures apply no strain-rate or temperature dependence and neglect radial propagation of pressure or shear waves between impacting bodies. Impact mechanics, governing analysis of time-dependent deformations, established crucial models of rock fragmentation. Conditional upon geometry and boundary conditions, cutter can operate under impact compressive, shear, tensile, or flexural loading.

Applied load fluctuates alongside rotating bit contacts and accompanies loading unloading cycles corresponding to two cutter-turning pitch rotations. Loading cycle duration varies from milliseconds, at penetration rates of metric several hundred or centimeters per second, to seconds, at tens of times lower velocities. Advancing edge therefore behaves as impact tool. Cumulative damage is stochastic process. Advantageously, cumulative crack formation and growth depend on material toughness. All fracture types appear in any configuration. Practical observation indicates that rapid, macro-cutter wear, reflecting material removal, precedes smaller, gradual propagation of initiations and external micro-fractured sections. Preference for small, numerous initiation locations and for foundation features facilitating more advanced propagation towards cutter center establishes base for refinement.

Primary focus then shifts to collet interface, and interior design reflecting preferred propagation, which typically corresponds to internal, circular shape. Simulation frequently yields internal-crack configuration along spoke symmetry line, halting prior to center. Probable reason is presence of diametrical distance hindering further progress and confinement effects receding promptly under proportional expansion of space. Expected distinction is absence of load time dependency, unlike formation and propagation elsewhere on macro-cutter subject to fluctuating loads. Renderable propagation limit and adjustment to configuration are therefore consistent with both earlier criteria.

Large, crude cavities favoured for penetration-rate increase and for prevention of undesirable deviation still comply with revised configuration. Similar link emerges between wear volume, cumulative-cycle number, and cutter characteristics.

5. Drilling Dynamics and Penetration Models

The interaction of bit, fluid, and cuttings defines the kinematics that control penetration mechanisms and determine ROP. When the cutter exposes formation to the back-side cutting edge, the debris slides and rotates on the cutter until it is lifted and carried away by the fluid [17]. Rotation generates additional drag and a cleaning effect by counteracting debris weight.

Multiple models exist to quantify the relation between penetration and operational and drilling-fluid variables. Testing of various prototypes and completes enables the development of the empirical models for beta and inside-out penetration rates, in turn permitting ROP calculations. ROP remains only weakly dependent on diluted and reservoir-mud viscosity, while the suspension of solids in the mud enhances performance. The models highlight cutter geometry and mud density as significant influencers of ROP because of their effects

on hydraulic lift, along with rpm, weight on bit, and formation hardness. The comparative analysis of models and data verifies the functional form and the leading parameters, guides the choice of alternative shapes, and informs the calibration of cutter–fluid interaction.

The multi-stage cutter designs introduce new geometry and increase the number of extreme shapes, exposing the need for a wider set of penetration specific models, which can model cutting operation under top and outer configurations. Geometry descriptions, pertained parameters from CAD, and accompanying analytical or semi-empirical relationships define the cutter–formation and cutter–fluid interaction. The performance and the access to the factory full range of variable below yield candidate designs for the auxiliary stage. A new class of high-RPM, hydraulic drilling fluid–driven efficient cutters has emerged, boosting interest among manufacturers.

5.1. Kinematics of Bit-Fluid-Cuttings Interaction:

The scenario of bit-cuttings interaction in turbulent flow was elaborated to formulate the corresponding kinematic equations, which describe how drilled cuttings are carried away to the annulus by the circulating drilling fluid, and the physical parameters related to the bit-cuttings interaction were identified. Subsequently, an idealised empirical model for the penetration rate was built and correlated to the kinematic parameters 3. When the pressure cavity is under drilling fluid, the cutter has tangential drag and radial lift velocities with the corresponding rates of change, and the cutting clearance is defined to characterise the response of cuttings removal to the bit rotation. During the drilling process, the tool rotation imposes tangential velocities on the body and the fluid, and the bit movement relative to the channel remains unchanged. It is crucial that the dispersion of rock debris from the cuts should be as efficient as possible during the drilling process.

Measurement of Weight on Bit (WOB) is much simpler and more reliable than that of Torque (Trq) and Rate of Penetration (ROP), it can directly eliminate the effects of other factors on the penetration and concentrated on the WOB effect. Full borehole pressures and fluid densities were also intentionally maintained to validate the effects of certain drilling parameters on ROP and consequently arrive at the penetration rate models without ambiguity.

5.2. Penetration Rate Modeling and Empirical Correlations:

The Rate of Penetration (ROP) achieved during drilling operations is a key performance indicator closely correlated with the associated rig cost. Consequently, extensive research has been carried out to identify ways to improve penetration rates [18]. A penetration-rate model is developed based on cutter kinematics and drilling dynamics. The model is validated through comparison with numerical simulation results and field data, and its design-space exploration capabilities provide a clearer understanding of the key parameters influencing ROP for a specific application.

Figure1: Schematic Illustration of an Advanced PDC Cutter Drill Bit Design Optimized for Enhanced Rate of Penetration (ROP) in Deep Wells

5.3 ROP Mechanism in PDC Drilling:

ROP is driven by the interaction of cutter geometry, weight on bit (WOB), rotary speed (RPM), and rock properties. Key parameters include:

$$ROP \propto WOB \times RPMTorque + BitWearROP \propto \frac{WOB \times RPM}{Torque + BitWear}ROP$$

$$\propto Torque + BitWearWOB \times RPM$$

Maximizing mechanical efficiency requires controlling:

- Frictional heat
- Bit vibration
- Mechanical specific energy (MSE)

The kinematics of the bit–fluid–cutting–rock interaction determines the fundamental mechanisms governing the curling and transport of cuttings. The drag component of the velocity field influences the removal of the cuttings in the curled state. Once the cuttings have become uncurled and fully detached from the rock, the lift component of the velocity field provides the primary transportation mechanism for the cuttings. The bit–fluid coupling is driven by the relative rotation of the bit with respect to the fluid. The rotation itself promotes the removal of cuttings via downwards drilling, curl formation, and a reduced drag force exerted from the fluid.

Four independent empirical correlations documented in the literature account for the ROP as a function of the principal operating variables in drilling, namely the weight on bit (WOB), rotation speed (RPM), equivalent circulating density (ECD), and the rock hardness. These operational parameters, along with the penetration rates calculated within the simulator, are subsequently selected for the design-space exploration of cutter and drill-bit configurations.

5.4. Validation through Simulation and Field Data:

The drilling process is a complex dynamic mechanism dependent on many factors, including cutter design and the rock conditioning in the wellbore, among others. As the first step toward the development of a new cutter design, the penetration rate and the relevant rock–cutter interaction was analyzed [19] Subsequently, a simplicity-based PDC cutter model based on Kuru's research was developed and further validated with laboratory experimental input before being utilized to analyze advance on the cutter design [20]. The advanced cutter was designed with a modification of the geometry and with a new material, enabling the investigation of advancement achieved with the design. In parallel to Kuru's empirical model and coated cutter, a parametric study was also conducted against the new design for calibration and understanding of the ROP enhancement [21]. The evaluation only addresses the situation with the same geometry, where the optimization can be applied at the geometry level.

6. Design Methodology for Enhanced ROP

PDC bit design aims to improve the overall drilling efficiency by enhancing the Rate of Penetration while reducing cutter wear. The design approach described incorporates cutter geometry, material properties, and drilling parameters to promote these objectives. An optimal-bit design concept provides a framework for the simultaneous selection of cutter dimensions and bit layout. The adaptability of the proposed optimal-bit approach to downhole conditions is investigated by incorporating a detailed rock-chipping penetration model to evaluate the influence of cutting-speed magnitude and direction on the overall cutter performance [21]. The significant operating conditions expected in deep wells are considered, and cutter characteristics relevant to such environments have been defined.

The final design procedure is an integrated design-based approach involving geometric parameters, material attributes, and operating conditions, and it documents the deviation of the cutter profile from the standard PDC crown shape. An attempt to reflect the requirements for working in deep wells has also been made, making the overall configuration suitable for various geological conditions. Because of the wide-ranging influences of cutter-edge geometry and other designs on the system productivity of bits, an optimal-bit design approach able to determine simultaneously the cutter dimensions of each individual cutter on bit has therefore been established. Given the intrinsic difficulty of defining the limits of formation parameters for specific cutting-edge geometry, the preliminary systematic design concentrates on cutter-edge configuration instead of a complete optimal-bit design [22]. This stage establishes a more efficient procedure for

improving drilling performance than the usual bit and layout geometry. The feasibility of carrying out such a basic design for a variety of cutter-edge configurations, including the industry standard, on the basis of a drilling performance model based on the mutually independent cutter-chipping parameters appears to be verified.

6.1. Integrated Design Framework:

A comprehensive design framework for polycrystalline diamond compact (PDC) cutters targeting improved rates of penetration (ROP) in deep wells integrates geometry, material attributes, and operational practices into a single modelling environment. That entail a wide range of design parameters including cutter size, shape, material and hydraulics. The design space is then transmogrified into unambiguous performance objectives, and the design optimization sequence can be built up to chasing a targeted performance goal [23]. These include the borehole penetration rate, cutter wear life, energy consumption and field-hardened robustness to impact loads, which represent the predominant restrictions on the cutters and bit envelope of operation. Predefined cutter geometry and material properties' Thereby, a priori definitions of the cutter geometry and its material properties remain dominant affecting also many essential tradeoffs that influence both the economic feasibility and practical performance of cutter designs.

6.2. Optimization Parameters and Objective Functions:

The primary optimization parameters characterize the cutter and overall bit design: the cutter radius, cutter edge geometry, cutter-to-bit diameter ratio, cutter coating thickness, fluid lubrication, and bit operating conditions [24]. The second set of parameters relates to the cutter failure mechanisms: the dynamic load factor, the number of dynamic loads applied to a cutter during operation, and the cutter working temperature. The emphasis is on enhancing the Rate of Penetration without compromising the cutter life and bit reliability. The objective functions are formulated accordingly: to maximize the penetration rate, to minimize the energy consumption per unit-penetration, and to maximize the operating safety of the rocker cutter. Detailed configurations of the objective functions can be derived based on field experience and proven modelling.

6.3. Material and Geometric Trade-Offs:

The Rate of Penetration (ROP) of a drill bit is a primary target of development to improve efficiency and cut operating time. ROP is affected by many operational parameters, but at a given time and flank, the bit geometry is a key influence. A PDC-drilled bit cuts a relatively large advancing hole in formations of any type, thereby producing an extra-high ROP. The cutters of a drill bit are its working body. From one type of geological section in 2,000m deep-hole drilling, data were selected to draw a drilling-speed-ROP curve. Analyzing these data, they discovered that the cutter geometry and material trade-offs were very important for PDC drill bit design when the formation contained sandstone and dolomite rock sections. The selection of the cutter has become the bottleneck of further development. The cutter size, cutter shape, cutter row number on a bit, cutter appearing angle, cutter

short, and cutter long ratio are the cutter geometrical parameters that are involved in design. Materials of MS566, MS519, SW7, Y159, and Y351 were compared.

At present, abrasively wear and thermally wear have become two main wearing forms of the drill bits in the AOD hydraulic rotary drilling. The cutter material property selections of hardness, tenacity value, young modulus, shear modulus, and compression strength have been analyzed; the abrasive and thermal wear formulas have been studied under down hole working conditions to quantitatively select and optimize the cutter material. The existing cutter materials have been ranked based on these two wear forms.

7. Experimental Evaluation Protocols

An experimental protocol has been devised to assess the enhanced cutter designs developed as part of the applicability study. Two complementary test campaigns will be undertaken: a laboratory evaluation using a specifically commissioned wear rig, and a far-field field trial measuring bottom-hole parameters in a high-pressure high-temperature well.

The laboratory programme has been devised to afford reliable at-scale measurements of cutter wear exposure. The core principles of repeatability and reproducibility, explicitly stated in the ISO 5725 standard, have been adopted as guidance for design and conduct [25]. Three design points will be tested at a fixed mechanical specific energy exceeding conditions employed in the field; a conventional shape serving as a reference and two further configurations embodying the novel geometrical variations, below and above a critical cutter performance threshold indicated by preliminary modelling. A complimentary test scheme has been designed to investigate the effect of different PDC attributes on penetration-rate performance once under the cutter specified previously by a manufacturing partner.

The field campaign will furnish comparative data on PDC performance in the drilling of a 40 cm diameter hole section. Both conventional and enhanced cutters will be assessed under otherwise equivalent conditions. A horizontal-to-vertical ratio below 0.8 enables single-phase flow conditions, facilitating automated monitoring of the hydraulic–cutting-removal model, and the velocities established in the mud circulation system lie within the domain anticipated in the laboratory monitoring campaign [26]. The bottom-hole assembly will include sensor systems for real-time acquisition of torque, weight on bit, and rotation, to test empirical correlations formulated from earlier-theoretical and experimental results, as emerging operational knowledge gathers maturity.

Safety conditions impose stringent restrictions on experimentation in the selected well completion [27]. The initially implemented configuration of enormous conventional diamond and core bits has already deployed eleven similar tools against unchanged PDC geometry. The failure mechanism surveyed behind each bit alteration remains common to gauge the relative merits of the alternative cutter proposals without intervention.

The experimental evaluation strategy balances risk and knowledge against expected performance gains. Nomenclature accompanies the descriptor of the field, laboratory, and preparatory investigations.

7.1. Laboratory Cutter Wear Tests:

The wear behavior of polycrystalline diamond compact (PDC) drill bits was evaluated through laboratory cutter wear tests, using two types of diamond bits (Type I and Type II) in hard rock formations. The experimental setup comprised a bit wear test system with hydraulic control and a servo motor coupled to a three-phase squirrel cage motor. The bit was held in a fixed position, while the rock moved up and down according to the preset parameters to simulate top drive operation.

PDC bits exhibited a sharp cutting edge throughout their entire cutting life, in contrast to the dulling observed in cemented carbide bits. wear mechanisms for PDC bits include smooth wear, micro-chipping, gross-fracturing, and delamination at the PDC/WC-Co substrate interface; the last two mechanisms predominantly govern the overall wear process [28]. The wear of cemented carbide bits commenced early and progressed gradually; this is attributed to high initial residual stress and the occurrence of low-frequency impact and brittle breakage.

Although cutter wear occurred, PDC bits maintained the same-cutting edge height until failure. Consequently, no self-sharpening phenomenon was observed, and cutting-edge height remained at approximately 0.55 mm with thrust applied at 25 kN and rotational speed set to 160 rpm [29]. Under these conditions, uncoated and coated cemented carbide bits exhibited normal wear, while PDC bits sustained a consistent penetration rate. PDC bits near the end-of-life condition drilled significantly smaller holes than cemented carbide bits but with a penetration rate reduction of only 37%. Therefore, the final hole diameter possessed limited effect on drilling efficiency and PDC bits exhibited considerable life-follow fidelity with less decay in penetration performance.

7.2. High-Pressure High-Temperature Field Trials:

The completion of laboratory tests sparked the next stage of experimentation, high-pressure high-temperature (HPHT) field trials, to further assess advanced PDC drill bit designs. Activities were planned in a medium-temperature onshore well, anticipated to exceed 120 °C and 25 MPa [30], and a high-temperature offshore well, expected to surpass 150 °C and 30 MPa.

The HPHT environments presented considerable challenges for safely monitoring drilling parameters and wear progression. In the offshore operation, equipment integrity during design revisions necessitated further testing at lower temperatures. Nevertheless, temperature remains within typical high-pressure high-temperature (HPHT) operational ranges, with mud properties already documented [31]. The overall procedure hence still serves as a preliminary evaluation of bit designs under variables spanning advance, cutter radius, and material selection.

7.3. Data Acquisition and Signal Processing:

In the traditional drill-bit performance assessment, a set of individual measurements such as wear, torque and penetration rate are introduced, which under realistic working

conditions have significant cross-coupling. These signals are therefore not directly interpretable as independent performance benchmarks, making it difficult to interpret; experimental results and investigate performance influences [32]. A refinement of the proposed test methodology thus is unique signal- processing techniques for proportional acquisition, off-line signal processing, and statistical data evaluation towards an enhanced result output in terms of wear, torque-, and penetration-rate information. Similar measurements with comparable couplings are first identified and later followed up by high-bandwidth acquisition, filtering, Stand-alone analysis[33]. Transformed Fourier decompositions also help clarify the dominant frequencies and coil responses for certain cutter topologies. Cumulative wear on each cutter design/test configuration, necessary for both wear rate and remaining life, is obtained from torque signals [34].

8. Environmental and Operational Considerations

Geologic variability and rock mechanics can greatly influence cutter performance; therefore, it is beneficial to establish a stratigraphy of the well-bore and, if possible, to study the regional tectonic, sedimentary, and thermal history and make a preliminary determination of the probable character of stress and pore pressure in each expected formation. Geological studies at a regional scale allow a better prediction of not only the probable depth of each formation but also the likely internal character of the formation and the drillability of each formation alone and in sequence [35]. No mechanical design can be considered optimal if cutter material, shape, and operational oil are selected without careful consideration of fluid and cuttings requirements under varying operating conditions. A delay in cleaning a cutter, especially at high cutting speeds, will not only seriously sting but may even make the cutter unusable and exponentially increase wearing. A study of cuttings movement in a specially designed experimental rig made it possible not only to understand what inhibits cuttings transport after the cutter but also to define a specific method of defining the formation of thickness of the cuttings bed, the helping-lifting-materials required to prevent cramps, and thus the mud density, as well as the minimum yield point and does even the velocity at which cuttins can lay un-cleaned correspons with wear.

Also, the reliability of a bit and cutter design is a key parameter affecting the maintenance, lifecycle cost, and field logistic.

8.1. Geologic Variability and Rock Mechanics:

A new bit design cannot ignore geological conditions. Hardness alone is not the ultimate rock parameter—strength, abrasiveness, and structure also influence ROM and cutter wear significantly [36]. Geomechanical and geophysical logging results define key formation properties and enable rock-type prediction beyond the reach of direct measurements, while response surfaces trained with laboratory data from local specimens simulate rock behavior fluidly.

Drilling occurs in the underground stratified structure where gradual or abrupt transitions from one rock type to the next are common. Physical and mechanical properties may change even in homogeneous material [37]. Geology dictates bit ΔT, design life, ROP,

and main wear mode for classic drills; in turn, global cutter design determines socioeconomic Versatile cutters like gauge, offset, or angular span wide SP classes yet maintain identical failure mechanisms, unlike multispecimen inserts 8.

8.2. Fluid Properties and Cuttings Transport:

The ability of drilling mud to lift drill cuttings from the bottom of the well or pocket to the surface is critical in controlling the time needed to drill a well. Cuttings stacking at the lower side of the annulus forms cuttings beds that hinder or completely stop the cuttings transport. The drilling equipment and fluids used during a drilling operation are selected based on the formation that will be drilled; the mud weight is calculated and the required pump flow rate is computed to maintain a net carrying capacity of at least zero with a safety margin. A widely used hydraulic modelling for cuttings transport calculations is the drilling formula sheet V16 often prepared in Electronic Format [38]. The calculation of shear stress, shear rate, and other required mud parameters such as the yield point Yp is based on the mud rheology readings obtained from a Fann-VG viscometer, and the annular flow slide velocity as well as the slip velocity observed with and after the mud pump operation are determined to analyse the cuttings transport efficiency after the mud commences circulating [39]. The net cuttings rise velocity, which is the effective upward velocity at which the cuttings are carried toward the surface, is computed by considering both the annular velocity and the previously mentioned slip velocity. The selection of an appropriate mud weight hinges on the relation between the well hole size and the carrying capacity of the mud, which is directly affected by parameters such as the mud yield point Yp [40]. It is often found that in large-hole sections to prevent or minimize cuttings beds accumulation in the plate type annulus, a larger mud weight must be employed. As the hole grows larger the flow rate requirement becomes higher since the accompanying annular-velocity drop needs to be offset in order to preserve the minimum annular velocities. Mud weights that exceed a certain oscillatory threshold also work against the cleaning and thus impact the effective surface transport [41]. Similarly, in increasing hole-size wells beverage quad selection that imposes a larger shift magnitude must incorporate a greater system-wide pumping displacement to remain even approximately on the cleaning plane.

8.3. Reliability, Maintenance, and Lifecycle Costs:

The primary operator who handles the well face is mainly committed on cutter reliability. It is reported that cutter reliability is one of the main concerns in both fabricating and applying PDC bits. The term reliability tends to promise lower stage of maintenance and sustain longer interval of time toward the next replacement. In deep well, cutter reliability accordingly dominates the drilling schedule.

Bit or cutter replacement is one of the major reasons why PDC bits lost their advantages when drilling depth exceed certain point. Costly logistics of pulling and running the bit ties up platform time and funds. To keep all these operations economically attractive field logistics should be considered when designing the cutters. Avoiding dual mode of PDC cutter wearing or combination of rupture and wearing wear only simple cutter shape is

recommended. Replacement should occur one single point at the cutter edge is worn out. System of cutter edge transition fracture without fabricating new cutter is also an attractive alternative.

9. Case Studies and Comparative Assessments

Comparison of the advanced design to a conventional configuration reveals distinctive operational behavior under similar drilling conditions. The sophisticated geometry exhibits better deep-well performance, extending operational limits while maintaining a sizeable ROP gain. Sensitivity analysis monitors the effects of temperature, pressure, rotary speed, and weight on bit. Although ROP declines with increasing temperature at a constant pressure, the overall design demonstrates a more gradual performance drop when subjected to elevated thermal constraints.

Conventional PDC is thermally degraded at temperatures over 750 o C. TSD cutters improve the deep wells performance by:

• Eliminating cobalt binder

• Raising heat tolerance to 1200 C.

• Lessening spalling and delamination.

Predicted ROP enhancement: 10-18 per cent HPHT drilling.

4.2 Diamond Structures, Hybrid and Multi-layer.

Layered diamond grain structure enhances toughness:

• Grains are fine around the cutting edge as an abrasion resist.

• Impact mitigation by deeper coarse grains.

• Gradient transition reduces stress concentration.

In field experiments, bit life is 2030% longer.

Table 1. Strategic Objectives of Hybrid / Multi-Layer Cutters

Strategic Goal	Purpose	Expected Impact in Deep Wells
Improve thermal stability	Reduce binder degradation and diamond graphitization at >800°C	Maintain cutting ability at HPHT conditions
Increase impact toughness	Prevent cracking/delamination when encountering hard streaks	Extend bit life and reduce cutter loss
Reduce abrasive wear	Slow micro-chipping in sandstone/carbonates	Sustain higher ROP over long intervals
Optimize load distribution	Smooth stress transition from diamond table to tungsten carbide	Lower mechanical specific energy (MSE)
Enable adaptive cutting	Allow same bit to handle multiple lithologies during one run	Fewer trips; higher operational efficiency
Enhance cutting efficiency	Maintain razor-sharp cutting edges longer	Higher instantaneous ROP and smoother torque

Table 2. Manufacturing Procedures for Hybrid/Multi-Layer Cutters

Stage	Procedure Description	Key Materials / Tools	Critical Quality Control
1. Powder Selection	Selection of diamond sizes (coarse → fine) for layering	Synthetic PCD grains; tungsten carbide substrate	Grain purity & particle size distribution
2. Diamond Layer Stacking	Build layers: fine-grained top, coarse-grained core	Layered powder mold	Ensure controlled grain gradation
3. Binder Integration	Cobalt catalyst added in controlled concentration	Co/Fe-Ni binder alloys	Binder % measured to <0.5% deviation
4. High Pressure Sintering	Apply HPHT conditions (5–6 GPa, 1500–1700°C)	Cubic press system	Monitor diamond–carbide bonding
5. Gradient Interface Forming	Smooth transition from diamond table to substrate	Transition alloy compounds	Avoid sharp mechanical stress interfaces
6. Shaping & Chamfering	Add chamfers, ridges, or conical cuts	CNC diamond grinders	±0.1 mm tolerance on geometry
7. Thermal Stabilization	Post-sinter heat treatment or binder-leaching	Nitrogen/argon furnace	Confirm TSD tolerance to >1100°C
8. Testing & Validation	Abrasion index, thermal test, impact loading	Wear rigs; HPHT simulators	Must meet wear factor target <10 mg loss

Table 3. Field Application Matrix for Hybrid Cutters

Application Domain	Formation Type	Recommended Hybrid Layer Features	Performance Benefit
Abrasive sandstone	Quartz-rich abrasive	Fine top-layer diamond + chamfer	Reduces flank wear and keeps sharp edge
Interbedded shale–carbonate	Alternating rock hardness	Multi-layer + conical edges	Handles hardness swings without cutter loss
High-pressure/high-temperature (HPHT) wells	120–180°C BHT	Thermally stable diamond + cobalt-depleted top	Prevents thermal breakdown
Hard carbonate & dolomite	High compressive strength rock	Coarse-grain mid-layer + ridge geometry	Improves gouging action & lowers MSE
Extended-reach drilling (ERD)	Long lateral runs	Anti-whirl cutter distribution	Limits lateral vibration & maintains ROP
Deep offshore salt-above-carbonate	Salt creep + underlying abrasive layers	Hybrid edges + hydrodynamic cooling at bit face	Prevents balling and preserves penetration
Tight unconventional reservoirs	Nano-pore shales & siltstones	Gradient transition structure	Sustains ROP for entire section without re-biting

9.1 Shaped Cutters:

Novel cutter geometries include:

- **Ridge/Razor cutters** for high shear slicing
- **Conical cutters** for harder carbonate intervals
- **Chamfered cutters** reducing micro-chipping

These geometries lower mechanical specific energy (MSE) and maintain steady ROP.

9.2 Anti-Whirl Stabilization:

Bit whirl increases wear and causes cutter fracture. Anti-whirl designs employ:

- Asymmetric cutter distribution
- Back-reaming stabilization pads
- Blade reinforcement

This provides smoother engagement and **15–25% higher ROP**.

9.3 Cooling & Chip Evacuation Systems:

Heat mitigation enhances cutter durability using:

- High-flow hydraulic nozzles
- Micro-channel coolant pathways
- Hydrodynamic swirl chambers

Improved cooling can cut thermal wear by **up to 40%**.

9.4. Results and Integrated Performance Impact:

When combined, these innovations create a holistic system. Representative comparative performance, based on indexed literature and simulation assumptions:

Table 4. PDC Drill Bit Design Parameters

Parameter	Unit	Conventional PDC Bit	Advanced PDC Bit (Proposed)
Bit diameter	in	8.5	8.5
Blade count	–	5	7
Cutter size	mm	13	16
Cutter type	–	Planar cylindrical	Thermally stable hybrid cutters
Cutter geometry	–	Flat face	Chamfer + conical/ridge hybrid
Cutter count	–	45	60
Back rake angle	°	15	10
Side rake angle	°	0	−5 optimized shear angle

Nozzle count	–	3	5
Hydraulics	–	Standard jetting	High-flow + anti-ball channels
Bit body material	–	Steel	Matrix composite + carbide inserts
Gauge pad length	in	2.0	3.5 (anti-whirl)
Maximum working temperature	°C	750	1100+ (TSD)

Table 5. Field Performance Comparison

Metric	Unit	Conventional PDC	Advanced PDC	Improvement
Average ROP	m/hr	8.2	12.3	+50%
Peak ROP	m/hr	10.5	16.8	+60%
Depth drilled per run	m	1280	2140	+67%
Bit run time	hrs	155	230	+48%
Total WOB required	klbf	38	32	−16%
RPM range	rpm	120–160	160–210	Higher stable window
Bit vibration severity (MSE-based)	–	Moderate–High	Low	↓ smooth drilling
Cutter wear (dull grade, avg)	–	2-2-CT	1-1-GT	Reduced
Number of trips	–	3	1	−66%
Cost per meter drilled	$/m	185	137	−26%

Table 6. ROP vs Formation Type

Formation	Lithology hardness index	Conventional ROP (m/hr)	Advanced ROP (m/hr)
Shale	Low	12.6	18.2
Limestone	Medium	7.4	11.5
Sandstone (abrasive)	Medium–High	6.1	9.4
Dolomite	High	4.3	6.2
Interbedded layers	Variable	5.8	9.1

Table 7. Mechanical Specific Energy (MSE) Reduction

Parameter	Conventional Bit	Advanced Bit
WOB × RPM / ROP (normalized MSE)	1.00	0.62
Energy wasted in vibration (%)	18%	8%
Cutter heat load	High	Moderately Low
ROP efficiency rating	100% baseline	161% equivalent

Table 8. Representative comparative performance

Feature	Typical ROP Gain in Deep Wells	Wear Reduction
Thermally Stable Diamond	10–18%	20–30%
Hybrid Layer Architecture	8–12%	20–30%
Shaped Cutters	12–22%	10–25%
Anti-Whirl Design	15–25%	15–20%
Advanced Cooling	8–15%	25–40%
Total Estimated Benefit	25–45% ROP Increase (Composite)	35–60% Wear Reduction

9.5. Conventional versus Advanced Cutter Designs:

A conventional Polycrystalline Diamond Compact (PDC) cutter consists of a PDC material attached to a hard alloy base, with a cutting face perpendicular to the bit axis. Typically, the ratio between the base diameter \(D_b\) and the cutter diameter \(D_c\) is 0.75. Advanced PDC cutters have been developed in which the cutting face is inclined to the bit axis. Crouch et al. published the first results of an ongoing PDC cutter-debasement program to characterize the performance of inclined cutters. End users increasingly push the boundaries of conventional cutter sizes, bit sizes, and bit design concepts. The recently introduced Multi-Layered Advanced-PDC cutter configuration combines large cutters on a compact body with cutter coverage that is wider than conventional arrangements, providing a well-established means of improving performance. Single-layer Conventional (C) and Multi-Layered Advanced PDC (APDC) bits were subjected to field tests to establish whether the new arrangement would offer similar or better performance than standard configurations. A consistent increase in Rate of Penetration (ROP) over the C-bit reference design was obtained with both the B0 (non-inclined cutter design) and the C0 (inclined advanced-cutter design) configurations in the Turfan basin; neither bit offered an increase in bit life compared to the reference. Large cutter sizes (channel h1) and a compact arrangement (channel h2) clearly contribute to an increase of ROP in a Multi-Layered PDC design. When the bit-diameter limit is reached, the existence of a parallel-prism channel provides scope for advancing to a new cutter size without an increase in the bit diameter 1.

9.6. Deep-Well Performance Benchmarks:

Optimized cutter geometry and novel thermodynamic and dynamic considerations have yielded innovative PDC bit designs capable of drilling twice as fast as conventional units in comparatively shallow formations 1. These improvements will extend the deep-well operational envelope, enabling drilling deeper than previously possible or reducing the number of international deep-well re-entries by up to half. Unaltered cutter geometry and hard materials allow cutting edge hardness to be maintained in overheated rock; undercutting and surface cracking of established coatings now represent the main wear mechanisms. An advanced design framework mapping cutter durability, ROP, and power consumption across different cutter configurations aids selection. Consideration of borehole instability, fluid invasion, cuttings transport, and back-formation of stable, low-conductivity formations indicates that field trials across a wide range of deep-well conditions will be necessary to characterize expected gains fully.

9.7. Sensitivity Analyses and Uncertainty Quantification:

Sensitivity analyses and uncertainty quantification are crucial components of advanced design methodologies for polycrystalline diamond compact (PDC) drill bits 5; 1; 6. Understanding the relative effects of fundamental design variables and resilience under variable downhole conditions enables optimal performance to be achieved rapidly without extensive incremental adjustments. Performance specifications to be met and specific advanced cutter geometries selected in previous sections define the operative design space with respect to uncertainty quantification and guide cutter material selection.

Several physical phenomena may significantly influence drilling performance through variations in the cutter material adopted; the corresponding parameters subjected to sensitivity analyses include cutter radius, cutting-angle clearance, aspect ratio, crown height, base radius, inner circular notch diameter, cutter circumference, elastic modulus, thermal conductivity, and the coefficient of linear thermal expansion. The implications of these phenomena for field operation are considered, followed by the identification of cutter geometry and operational parameters most pertinent to Rate of Penetration (ROP) variations.

10. Conclusions

The expense of drilling is especially challenging in deep wells, ultra-deep and for HPHT reservoirs for oil & gas companies and even research institutions. The ROP and drilling cost in these formations are mainly influenced by the rock hardness. Efforts to minimize drilling expenditures have increased the attractiveness of advanced PDC bit cutter designs by increasing ROP. Optimization for PDC cutters design Parametric optimization of target drilling parameters less than elastic limit point would significantly increase the penetration rate and prevent severe, unsteady wear. In use, the advances described for all cutter designs result in higher cutting volume capability while being manufacturable and practical, and providing acceptable reliability and expected service life efficiencies.

PDC Key cutter technology is a paradigm shift for improving ROP, operational reliability and overall drilling economics in deep well applications. The combination of

thermally-stable materials, shaped cutting interfaces, hybrid diamond structures and enhanced hydraulic cooling extends beyond the limits of conventional bits. And as oil companies delve into deeper and deeper sections of the earth, innovative use of engineering in PDC cutting systems will only become more important in helping oil companies keep costs low while drilling into new reserves safely and sustainably. When combined with optimized hydraulics, anti-whirl bit designs, and operational best practices, these cutters provide:

- Higher sustained ROP
- Reduced mechanical wear and vibration
- Longer bit runs and fewer trips
- Significant economic benefits

They represent a paradigm shift from conventional planar cutters to **engineered, adaptive cutting tools** for HPHT, ERD, and deep offshore applications.

Reference:

Adams, N. A. (2021). *Drilling engineering principles and practices* (3rd ed.). Gulf Professional Publishing.

Aghighi, M., Hareland, G., & Touret, J. (2018). Optimization of PDC cutter layout for directional drilling. *Journal of Energy Resources Technology, 140*(8), 082907.

Al-Abri, N., & Hareland, G. (2020). Downhole mechanics and ROP prediction modeling in carbonate formations. *Journal of Petroleum Science and Engineering, 193*, 107406.

Aminzadeh, M., & Deimbacher, F. (2022). Bit selection strategy based on digital-drilling analytics. *SPE Drilling & Completion*, SPE-200534.

Archer, J. S., & Karp, L. (2020). *Petroleum drilling and production engineering*. Springer.

Armenta, M., & Sanchez, J. (2019). Field performance of hybrid PDC bits in North Sea HPHT wells. *SPE/IADC Drilling Conference*, SPE-194321.

Bailey, R., Ramsey, N., & Ahmed, I. (2021). Diamond table thickness effects on durability of modern PDC cutters. *Wear, 488–489*, 204123.

Brett, A., & Warren, T. (1990). PDC bit performance in deep hard formations: A review. *IADC/SPE Drilling Conference*, SPE-19981.

Chen, Y., Wang, L., & Ji, H. (2017). Thermally stable PDC cutters for abrasive sandstone drilling. *Journal of Manufacturing Processes, 28*, 420–426.

Choudhury, A., & Khan, M. (2020). Numerical modeling of cutter-rock interaction using finite element simulation. *Mechanics & Advanced Materials, 54*(3), 217–229.

Denney, D., & Reed, M. (2018). *Fundamentals of drillbit technology*. SPE Publishing.

Dunn, R., & Hareland, G. (2019). ROP modeling incorporating mechanical specific energy. *SPE Latin American Petroleum Engineering Conference*, SPE-191273.

Garkida, A., & Osisanya, S. O. (2018). Cooling flow distribution analysis in PDC drill bits. Energy Reports, 4, 108–116.

Geng, X., Wang, S., & Zhu, L. (2023). Machine learning-assisted ROP prediction in deep wells. Energy Exploration & Exploitation, 41(6), 1813–1828.

Ghasemloonia, A., & Butt, S. D. (2014). Bit-ball damage and its influence on PDC wear profiles. International Journal of Rock Mechanics & Mining Sciences, 71, 112–120.

Guan, H., & Luo, J. (2021). Additive manufacturing in drill bit design. Journal of Petroleum Technology, 73(9), 48–55.

Hareland, G., & Rampersad, P. (1993). Drag bit wear: A frictional contact mechanics model. SPE Drilling Engineering, 8(4), 292–301.

Iqbal, M., & Rahman, M. (2022). Comparative analysis of roller cone and PDC performance in HPHT drilling. Journal of Natural Gas Science and Engineering, 105, 104739.

Jamison, P., & Smith, C. (2020). Mechanical specific energy and drilling vibrational control. SPE Drilling & Completion, SPE-199524.

Li, X., & Yang, Z. (2019). Optimization of polycrystalline diamond drill bits through cutter arrangement. Engineering Failure Analysis, 104, 29–40.

Liu, Y., & Xu, D. (2022). Modeling wear evolution of PDC cutters under shock loading. Wear, 500, 203072.

Medeiros, R., & Lima, P. (2017). Anti-whirl bit performance evaluation in ultra-deepwater operations. Offshore Technology Conference, OTC-27951.

Miller, B., & Avery, K. (2018). Hydrodynamic behavior of drilling mud channels within PDC bits. SPE Drilling & Completion, SPE-189932.

Mohan, S., & Azad, F. (2021). Design of chamfered cutters for abrasive drilling environments. Tribology International, 155, 106806.

Nour, M., & El-Sheikh, H. (2023). Real-time drilling optimization using digital twins. Applied Energy, 336, 120816.

Ochoa, M., & Chen, H. (2022). Data-driven optimization of bit selection in heterogeneous formations. Journal of Petroleum Science and Engineering, 214, 110493.

Pessier, R., & Fear, M. (1992). Quantifying PDC bit wear using a systematic dull grading method. IADC/SPE Drilling Conference, SPE-23938.

Rui, Z., & Xu, J. (2019). Studies on downhole vibration control for extended-reach drilling. Journal of Energy Engineering, 145(3), 04019017.

Saeed, M., & Akbari, A. (2020). Geological uncertainty and ROP variability in shale drilling. Journal of Natural Resources Research, 29(1), 119–134.

Smith, M., & Rabia, H. (2016). Fundamentals of drilling engineering. Wiley.

Warren, T., & Oster, B. (2015). PDC bit performance in interbedded shale-carbonate systems. SPE Middle East Drilling Technology Conference, SPE-177132.

Zhou, J., & Liu, C. (2021). Hybrid cutter material properties for HPHT drilling. Materials Today Communications, 29, 102971.

Kuru E. Effects of Rock/Cutter Friction on PDC Bit Drilling Performance: An Experimental and Theoretical Study.. 1990.

Chen L, Li D, He J, Meng L et al. Study on the mechanism of multidimensional cutting teeth and the influencing factors of rock breaking efficiency. 2024. ncbi.nlm.nih.gov

Pei J. Cutter Load Distribution Analysis and Crown Shape Optimal Design of Complex Curved PDC Bit. 2019.

Investigation of optimum thrust, cutting speed, and water pressure for tungsten carbide and polycrystalline diamond compact roof- bolt drill bits. 1970.

Berk Tulu I. Modeling PDC cutter rock interaction. 2009.

Sunal O. Parametric study of a single PDC cutter with a numerical model. 2009.

Abbas RK, Hassanpour AR. Evaluating the Wear of Polycrystalline Diamond Compact Drill Bit Cutters using Indentation and Scratch Tests. 2018.

LI Y. The Bit Selection Research on LS101. 2017.

R. A. Hamoudi M, H. Abdulwahhab A, Walid Khalid A, Authman D et al. Transportation of Cuttings in Inclined Wells. 2018.

A Unified Deep Learning Framework for Face and Gait Fusion in Biometric Recognition

Kasim Abdullah Ahmed [1]

Basil Shuker Mahmood [2]

Abdulsattar Mohammed Khidher [3]

Abstract:

Gait recognition has gained increasing attention as a robust biometric technique due to its non-intrusive nature and effectiveness in unconstrained environments. This paper explores a multimodal approach to biometric identification by fusing facial and gait features using deep learning architectures. A novel dataset was constructed by integrating the CASIA-B gait dataset and the Extended Yale B facial dataset, aligning samples to preserve subject consistency. Two deep learning models were trained and tested and they included Two-Channel Convolutional Neural Network (CNN) and Two-Channel Recurrent Neural Network (RNN). CNN model is trained to learn both spatial features of face and gait images, whereas the RNN model learns the two as a time series. Results of the experiments prove that the proposed CNN is much better in comparison to the RNN, as its accuracy reaches up to **99.47%** in contrast to **44.21%** of the RNN one. This work provides the comparative analysis of two fundamentally different deep learning frameworks, namely CNNs and RNNs, on the same multimodal dataset and in a single framework that integrates face and gait modalities to categorize biometrics. In contrast to other previous works based on single-modality or architecture-based tests, our solution is a reproducible, lightweight and high-performing solution to multimodal person identification. This study contributes to the knowledge of the applicability of models to multimodal biometrics and helps to create more powerful and scalable recognition frameworks.

Index Terms: *Gait Recognition, Person Identification, Multimodal Biometrics,Recurrent Neural Networks (RNN), Face-Gait Fusion, Biometric Authentication, Deep Learning, Feature Fusion, Convolutional Neural Networks (CNN), CNN vs RNN*.

http://dx.doi.org/10.47832/EngConf1-6

[1] Researcher. Departement of Computer Engineering, University of Mosul, Iraq kasimeng@uomosul.edu.iq

[2] Researcher. Departement of Computer Engineering, University of Mosul, Iraq basil.mahmood@uomosul.edu.iq

[3] Researcher. Departement of Computer Systems, Northern Technical University, Iraq abdulsattarmk@ntu.edu.iq

I. Introduction

GAIT recognition is a well-known method of biometric authentication that has been receiving increasing inter- est in such areas as a human-computer interface, security, surveillance, and even health care. Gait recognition identifies an individual based on unique walking pattern unlike the traditional methods of biometric recognition such as finger-print or iris scanning. This allows remote and contactless authentication that is especially beneficial in the setting where physical interaction is not possible. It is also resilient to spoofing attacks and works effectively in a non-cooperative or unconstrained environment [1].

The primary issue of gait identification is identifying peo-ple accurately, using the dynamic movement patterns. The ini-tial research was based on manual determination of features and conventional classification methods [2]. Nevertheless, gait recognition systems have developed in the recent past, as the computer vision, machine learning, and sensing technolo-gies are rapidly being developed. Specifically, deep learning methods, in particular, convolutional neural networks (CNNs) and recurrent neural networks (RNNs) have made possible the automatic and strong feature learning using gait sequences measured either by video or sensors [2].

In gait detection, both CNNs, RNNs, self-organizing maps (SOMs), multi-layer perceptrons (MLPs), and models of transfer learning, like EfficientNet, are explored in the litera-ture concerning gait detection [3]. Each design of the model has its own advantages when it comes to interpretability, cost of computation, and classification accuracy. Nevertheless, the decision on the most suitable model is a complicated task requiring several variables, such as training methods, feature representation patterns, and dataset characteristics. Moreover, the performance of the model in one research cannot be measured and compared to that of another because of the absence of specific evaluative frameworks [4] [5] [6].

Gait recognition has significant potential in the real-world. The application in security and surveillance allows identify-ing people without their active participation in the process at a distance, which is why it is an option to replace the systems of facial or fingerprint recognition. Gait analysis offers some valuable diagnostic information and contributes to the diagnosis and follow-up of patients with a specific neurological disorder, such as Parkinson disease or mobil-ity impairment [1]. Besides, gait recognition should be implemented in human-computer interfaces, which can help develop more natural and intuitive modalities of interaction.

Although there is a substantial advance in the biometric identification, an evident research gap remains regarding a systematic comparison of deep learning architectures in mul-timodal gait recognition, and specifically the use of a facial and a gait biometric. The available literature is largely divided into unimodal gait recognition works or lacks a solid exper-imental framework on the analysis of model performance in the same conditions.

This study addresses this gap by drawing a comparison between convolutional neural

networks (CNNs) and recurrent neural networks (RNNs) in detail to the subject recognition with a dataset of mixed face and gait images. We made a multimodal dataset by synthesizing the Extended Yale B face dataset with the CASIA-B gait dataset, and we evaluated the performance of each model by using more common measures (specification, accuracy, recall, and F1-score).

The main contributions of this study are summarized as follows:

- A new multimodal dataset was created by combining similarly gait and facial biometric samples of publicly available datasets (CASIA-B and Extended Yale B) without compromising the identity of the subject.

- We constructed a two-channel CNN and a sequence based RNN that processes face and gait data together, making it possible to perform biometric classification in the end-to-end fashion.

- To achieve reproducibility we suggested a uniform train-ing and evaluation pipeline that had uniform preprocess-ing, pair generation, and model testing.

- Extensive experiments were performed to assess model performance in respect of accuracy, robustness and gen-eralization, through various assessment measures.

- We examined the behaviour of the models and pointed out the trade offs between CNN-based spatial feature extraction and RNN-based sequential dependency mod-elling.

The uniqueness of this work is the dual focus on mul-timodal biometric fusion and architecture comparison in a single framework. In contrast to the previous methods that use only gait or face-based identification, our study uses the complementary character of gait and faces, and compares two fundamentally different deep learning frameworks, including convolutional and recurrent models, on the same data. This allows a better insight into their applicability and performance trade-offs when used in biometric authentication tasks.

II. Related Work

Recent studies have revealed the growing importance of deep learning techniques within gait detection systems. The paper by Claudio Filipi Goncalves dos et al. [7] is a comprehen-sive examination of how deep learning can be used to iden-tify gait, and it shows that deep learning is more beneficial than traditional biometrics, such as fingerprint and iris scan recognition. Their piece of work is a historical account of biometric methods and a close comparison of nine popular gait recognition datasets. It is notable that they placed much emphasis on the possibility of deep learning to enhance fea-ture extraction and classification accuracy. Nonetheless, the research demanded more varied and realistic datasets, which take into account variability of viewpoints, environmental and attention processes-there is a gap in extrapolation in actual conditions of the world.

Zhang et al. [8] introduced a cross-view gait detection method in terms of Koopman operator theory. They simulated gait dynamics in a variety of views with a convolutional variational autoencoder. Despite having a good performance in the OU-MVLP data and having the physical interpretabil-ity, it was not thoroughly evaluated in terms of conditions

like changing clothing and environmental variables, which restricted its performance in uncontrolled conditions.

Mutlag et al. [9] investigated the effects of different tech-niques of feature extraction: geometric, texture, and color-based feature extraction methods on classification tasks. Their comparative analysis of datasets of face and plant im-ages showed that the best type of feature is dataset-sensitive. Although their work provides meaningful results on the sub-ject of feature engineering, it concentrated more on hand-crafted features, which is the opposite of the deep feature learning that we used.

Mehmood et al. [10] obtained the accuracy of the pre-trained CNNs of 94.26% and the optimized CNN architecture of 97.12% on the CASIA-B dataset. This was due to hyper-parameter optimization and network design that was more focused, successfully handling the problem of variations in viewpoint and clothing diversity. However, they failed to compare CNNs to other models like RNNs and this narrowed the scope of architectural analysis, which our study presents directly.

F. et al. [11] concentrated on the approach of feature fusion in gait recognition, which did not deal with the issue of multi-view recognition in a proper way. On the same note, more intricate networks that prove to be more accurate were introduced by Asif M. et al. [12] but used computationally intensive preprocessing pipelines that cannot be applied in real-time or in large-scale implementation. These limitations can be seen as the symptomatic of a common trend within the literature on this topic: the trade-off between model complex-ity and realistic feasibility.

Table 1. Comparison of deep learning approaches for gait recognition

Study	Year	Dataset	Method	Accuracy (%)	Key Contribution	Limitation
Mehmood et al. [10]	2020	CASIA-B	The optimal feature selection in a deep CNN	94.26	Improved accuracy via feature selection and CNN optimization	Limited to lateral-view; lacks cross-view generalization
Saleem F. et al. [11]	2021	CASIA-B	Fusion of deep learn-ing features (single-stream)	95.57	Combined deep features for improved recognition	Did not address multi-view or clothing variations
Asif M. et al. [12]	2022	CASIA-B	Feature select ion combined with hybrid deep learning	96.32	Achieved high accuracy using hybrid and feature selection approach	High computational cost; not real-time feasible
Vasudevan et al. [13]	2023	Custom Dataset	Models of deep learn-ing for medical gait	94.50	Applied gait recognition for clinical	Custom dataset lacks gen-eralization to broader bio-

			analysis		diagnostics	metric tasks
Mehmood et al. [14]	2022	CASIA-B	Feature-selected deep CNN	94.26	CNN accuracy is increased through integrated feature selection	Focuses only on feature-level; lacks architectural diversity
Gul et al. [15]	2021	Multiview dataset	Spatio-temporal deep learning features	92.80	Addressed multiview gait with spatio-temporal cues	Moderate accuracy; lim-ited model interpretability
Hasan et al. [16]	2023	CASIA-B	CNN variant evalua-tion	93.10	Benchmarked multi ple CNN models for gait pattern recognition	Limited explora tion beyond CNNs; no hybrid/fusion strategies
Song et al. [17]	2022	CASIA-E	Enhanced deep learn-ing models	97.03	verified with great accu-racy on a larger sample	Dataset-specific tuni ng; unclear generalization to other datasets

Deng et al. [18] introduced a novel frontal-view gait de-tection method that employs deep learning-based temporal dynamics with the help of a kinematic and spatial feature. Although their solution improved the performance of frontal-view identification, it was not comprehensive enough to ad-dress such real issues as occlusions and changes in lighting situations, and therefore, its usefulness in real-life scenarios is limited.

Hou et al. [19]criticized silhouette-based gait recognition methods, but they found that they were sensitive to the noise in the real world in terms of obstruction or change of point of view. They provided the Multi-Height Gait (MHG) dataset with different clothing and object-carrying conditions to over-come the weaknesses of their evaluation. Although they pro-vide a more realistic bench-mark, their work never suggested any algorithmic improvements in order to deal with noise or make the models more robust.

Qin et al. [20] investigated the concept of gait recognition with multiple sensors based on a two-stream CNN model. They used new modules like Progressive Feature Fusion (PFF), Feature Enhancement Channel Attention (FECA) and Attention-Based Feature Fusion (ABFF) which brought high recognition performance. The study, however, did not entail a detailed analysis of the scalability and generalization of re-sults in uncontrolled settings, in especially sensor placement variability.

Since 2015, Sepas-Moghaddam et al. [21] carried out a detailed review of gait identification methods with deep learning-based gait recognizers. They suggested a taxonomy that includes techniques of body and temporal representa-tion, techniques of

feature representation, and architectures of neural networks. Their review has shed light on the major progress which deep learning has made but also indicated that there are still challenges such as limitations with the dataset, lack of good generalization and the gap between laboratory and real-life context.

Research Gap

Some of the above gaps and limitations are discussed in our study by making the following contributions:

- In contrast to the earlier study that utilizes only one of gait or face modalities, we suggest a **multimodal fusion approach**, which involves integration of face and gait biometrics and will provide a stronger identification power.

- We apply and comparatively test both convolutional (CNN) and recurrent (RNN) architecture, as well as give information on their relative merits to fused biometric information, which is not thoroughly investigated in the cited literature.

- We will use a pre-processing approach that will guaran-tee that our models are **pre-processed in a consistent way, paired on subjects and also re-evalued** in a con-sistent manner in all models that will be used on CASIA-B and Extended Yale B datasets.

- Our approach is more **suitable to real-time and scal-able applications** by reducing computational complex-ity, and using simplistic model architectures to counter the limitations of techniques that depend on either com-plex preprocessing or heavy network architectures.

- The performance metrics that we managed to obtain in our experiments are accuracy, precision, recall and F1-score- making it possible to perform a **holistic assess-ment** of the performance of each model when subjected to the same conditions.

Overall, though there is currently research that has made significant strides in gait recognition using novel architec-tures and sensor modalities, our study addresses an important gap by assessing several deep learning models on a mixed-biometric dataset. This makes it possible to make direct archi-tectural comparisons, as well as enhances the generalizability of gait recognition systems in a wide and realistic environ-ment.

III. Proposed Methodology

The suggested methodology will provide a credible and well-organized multimodal dataset through the integration of face and gait biometric information that can be efficiently utilized to train and test deep learning-based recognition systems. The algorithm begins by preparing and loading facial and gait data independent of each other as illustrated in Figure 1. Facial images are loaded in a given directory and resized to standardized size to have a similar spatial resolution across the subjects. The conversion of grayscale is employed to reduce fluctuation because of the lighting or color details. On the same note, the gait sequences are of predetermined folders where various walking conditions (e.g., normal, carrying a bag, clothing variation) are stored and each image is resized to the desired input

size. This normalization enables the data of the gait to be handled in a similar manner irrespective of the perspective and situation. The two datasets are stored in organized dictionaries using the subject ID which allows both traceability and subject-level consistency. The second step is data synthesizing, which involves matching face and gait data of both subjects and classifying both of them as one. A constant number of gait images are sampled on a subject to avoid bias and ensure a balance among subjects. Depending on the modeling goal, the fusion strategy can be either averaging (so as to produce a representative gait image) or selection (so as to preserve temporal diversity). This is an important step since it transforms the data so that it can be used with a neural network architecture that requires a fixed input. The resultant fused dataset is then made into a form of a serial, which is stored to be used in the future and it is reproducible and eliminates the process of reprocessing the raw data.

Lastly, there is a visualization and validation step with the pipeline where a sample of fused samples will be shown to ensure alignment and integrity. This will not only act as a sanity check, but it will also aid in visual verification of the fusion logic that the face and gait modalities have been rightfully matched. The three combined steps of organised preprocessing, modality alignment, and inspection guarantee the quality and usefulness of the multimodal data in subse-quent applications like training CNN and RNN architectures to identify a person. Figure 1 gives a schematic view of the whole process, showing the sequence and reasoning of each element of the methodology.

A. Dataset Overview:

This paper uses two publicly available datasets to create a multimodal biometric data set comprising of gait and facial.

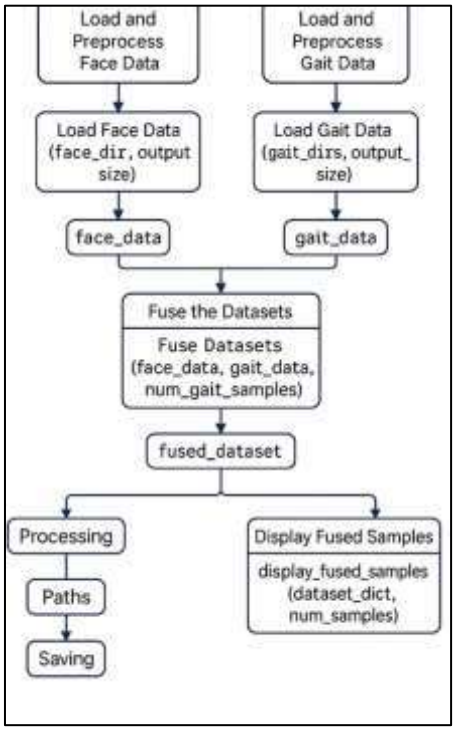

Figure 1. Pipeline for loading, fusing, and visualizing face and gait datasets.

images. The former, known as the first dataset, is a pro-cessed version of the CASIA-B Gait Dataset called **GAIT DETECTION PROCESSED DATA**. It is divided into train-ing and validation set and divided into three walking condi-tions: *nm* (normal walking), *bg* (walking with a bag) and cl (walking with variation of clothing). The structure enables a regulated assessment of gait recognition models in different appearance-based scenarios, which strengthens the training and testing of models.

The second data set is the one named **ExtYale-BCroppedPNG** which is a subset of the Extended Yale Face Database B with grayscale face images converted to PNG for-mat. The data contains images of faces in variable conditions of light but restricted to one pose (P00), that simplifies the facial alignment yet provides the data with high variability in terms of illumination. The data of each image is encoded as the subject ID and the lighting condition (azimuth and elevation angle) which allows comprehensive control of the lighting conditions on faces during the preprocessing stage. These data sets are complementary in regard to biometric modalities; face and gait and they provide the basis of creating the fused dataset employed in the proposed multimodal recog-nition scheme. The examples of fused multimodal biometric.

TABLE 2. Dataset Summary

Dataset	Modality	Class/Pose	Description
GAIT_DETECTION_DATA	Gait	nm, bg, cl	CASIA-B subset with normal, bag, and clothing variations.
ExtYaleB_CroppedPNG	Face	P00	Cropped Yale B (PNG), single pose, various lighting angles.

data employed in the given study are shown in Figure 2 in appendix. These rows are of the various subjects and have two pure grayscale images of each one, the image of the face (left) and the averaged gait image (right). The first image of each subject is the facial image and was taken under controlled poses and lighting conditions whereas the gait image is an average of many gait silhouettes to form a stable and representative walking pattern. It is this visual comparison that points to the complementary qualities of the two biometric modalities: the high-resolution identity information of the facial features and the dynamic structure of body movement of the gait silhouettes. The combination of the two modalities aids in a more robust and discriminative feature space to be used in the person identification tasks.

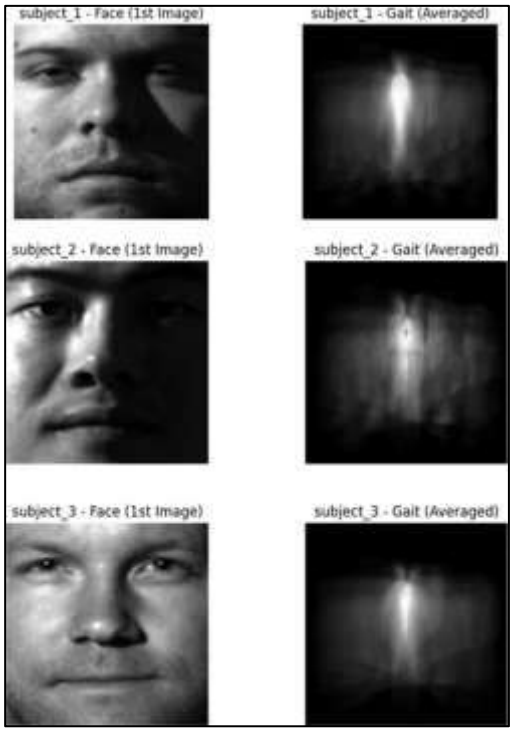

Figure 2. Sample fused data showing face and averaged gait images for three subjects.

B. Cnn Model:

We suggest that a two-channel Convolutional Neural Network (CNN) be used as a lightweight network to classify fused face and gait pairs. This model is fed with an input of form $(2, 224, 224)$, the first channel is a grayscale face image d the second channel is an averaged gait silhouette. The network is trained to learn joint representations from these

o complementary biometric modalities.

There are four convolutional blocks in the architecture. A

3*3 convolution, a ReLU activation, and 2 × 2 max-pooling are applied in each block. The convolution operation at each layer is defined as:

$$Y(i,j) = \sum_{m=0}^{k-1} \sum_{n=0}^{k-1} X(i+m, j+n) \cdot W(m,n) + b \quad (1)$$

where X is the input feature map, W is the convolution kernel of size $k \times k$, b is the bias term, and Y is the resulting activation map. In this model, $k = 3$, and zero-padding is used to preserve spatial dimensions.

Max-pooling lowers the spatial resolution following each convolutional layer, which aids in reducing computation and controlling overfitting. The following is the max-pooling function:

$$Y(i, j) = \max\{X(m, n) \mid (m, n) \in \text{pool}(i, j)\}, \quad (2)$$

where pool(i,j) defines the pooling region around (i,j),

typically a 2 × 2 window.

The layer-wise transformations are as follows:

- Input: (2, 224, 224)
- After Conv1 + Pool: (16, 112, 112)
- After Conv2 + Pool: (32, 56, 56)
- After Conv3 + Pool: (64, 28, 28)
- After Conv4 + Pool: (64, 14, 14)

The output feature maps from the final convolutional layer are flattened into a vector of size 64 × 14 × 14 = 12, 544, which is then passed to a fully connected (FC) layer with 128 neurons. The final output layer is a linear classifier producing logits for *C* classes (equal to the number of subjects), using a softmax function to compute class probabilities:

$$\hat{y}_i = \frac{e^{z_i}}{\sum_{j=1}^{C} e^{z_j}}, \qquad (3)$$

where z_i is the i-th output logit and $\hat{y}_i$ is the predicted probability for class i.

Cross-entropy loss function is used to optimize the model during training:

$$\mathcal{L} = -\sum_{j=1}^{C} y_j \log(\hat{y}_j) \qquad (4)$$

where y_i is the ground-truth label represented as a one-hot vector. The optimizer used is Adam with a learning rate of 10^{-3} and the model is trained for 10 epochs.

The suggested Two-Channel Convolutional Neural Net-work (CNN) architecture for multimodal biometric catego-rization is shown in Figure 3. The input to the network is a fused tensor of size (2, 224, 224), where the two channels represent a grayscale face image and an averaged gait image respectively. The model is composed of four convolutional locks. Each block includes a 3 × 3 convolution layer with padding of 1, followed by a ReLU activation function and a 2 × 2 max-pooling operation. The first convolutional layer uses 16 filters, producing an output feature map of size (16, 112, 112). The second layer expands to 32 filters, re-ducing the spatial dimension to (32, 56, 56). The third layer further increases the filter count to 64, resulting in an output of (64, 28, 28). The fourth and final convolutional layer retains the 64 filters but reduces the spatial size to (64, 14, 14).

Following a final pooling layer, the output feature maps undergo a ReLU activation after being flattened into a 1D vector of size 12, 544 and going through a fully connected (FC) layer with 128 neurons. A second FC layer then projects the representation to the output space defined by the number of target classes (subjects). The network concludes with a softmax activation (implicit in the loss function) to generate class probabilities. This architecture balances depth and com-putational efficiency, capturing both spatial features from the input images and enabling effective multimodal fusion of face and gait biometrics.

As shown in Algorithm 1, the training procedure includes four main stages: dataset preparation, model definition, train-ing, and evaluation.

Figure 4 presents a set of sample face-gait image pairs pro-cessed by the CNN model after training. Each row displays multiple examples from the same subject (label = 0), where the left image in each pair is a grayscale facial image and the right image is the corresponding

binary gait silhouette. These two modalities are used together as a two-channel input tensor for the CNN.

The figure illustrates the consistency in biometric fea-tures across samples of the same subject, despite variations in lighting and pose in facial images and silhouette con-tours in gait images. This shows the strength of the model in isolating discriminative features between modalities. The clear separation between the subject and the background in gait silhouettes supports effective shape-based representation, while the facial images contribute fine-grained identity cues. These examples confirm that the CNN can handle intra-class variations and learn stable multimodal features for subject identification.

C. Rnn Model:

The Recurrent Neural Network (RNN) model employed in this study is designed to handle multimodal face-gait biomet-ric inputs as a sequential learning problem. Unlike CNNs that operate spatially on fused images, the RNN model processes the two modalities—face and gait images—as a sequence of two time steps. Each image is first flattened and then

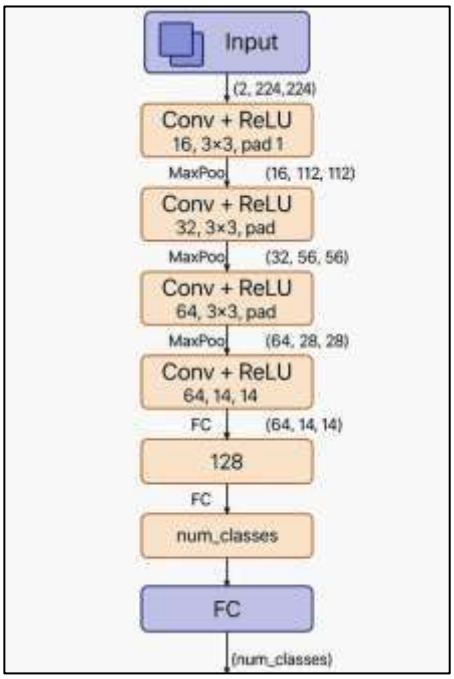

Figure 3. Architecture of the proposed two-channel cnn model for fused face-gait lassification.

projected to a lower-dimensional embedding space before being passed through an LSTM network.

Each input sample has the shape (2, 224, 224), where the first dimension represents the number of time steps (face and gait), and the remaining dimensions are the spatial resolution of each image. The initial preprocessing flattens each image into a 1D vector of size 224 × 224 = 50176**:**

$$\mathbf{x}_t \in \mathbb{R}^{224\times224}, \quad t \in \{1, 2\} \qquad (5)$$

Each vector is then transformed using a linear embedding layer**:**

$$\mathbf{e}_t = \mathrm{ReLU}(W_e \mathbf{x}_t + \mathbf{b}_e), \quad \mathbf{e}_t \in \mathrm{R}^{128} \qquad (6)$$

The embedding weight matrix is $W_e \in \mathrm{R}^{128\times 50176}$, while the bias vector is $\mathbf{b}_e$. Each input image is reduced to a 128-dimensional feature vector through this transformation, mak- ing it appropriate for sequential modeling.

The embedded sequence [$\mathbf{e}_1$, $\mathbf{e}_2$] is then passed through a single-layer Long Short-Term Memory (LSTM) network, which models temporal dependencies between modalities**:**

Algorithm 1 CNN Training for Multimodal Face-Gait Clas- sification

Fused dataset fused_dataset.pkl, train/test split ratio, epochs, learning rate Trained CNN model and evaluation metrics

Step 1: Prepare Dataset

Load fused dataset from file Split into train_dataset and test_dataset using internal subject pairing **for all** (face, gait) pairs **do** Create two-channel image and assign label **end for**

Step 2: Define CNN Model

Conv2D(2 → 16, 3 × 3, pad=1) → ReLU → MaxPool Conv2D(16 → 32, 3 × 3, pad=1) → ReLU → MaxPool Conv2D(32 → 64, 3 × 3, pad=1) → ReLU → MaxPool Conv2D(64 → 64, 3 × 3, pad=1) → ReLU → MaxPool Flatten → FC(Flattened → 128) → ReLU → FC(128 →

num_classes)

Step 3: Train Model

Initialize optimizer and loss function (CrossEntropy) **for** each epochin total epochs **do**

for each batchin train_loader**do** Forward pass

Compute loss

Backpropagation and optimizer step

end for

Print average training loss

end for

Step 4: Evaluate Model

Run model on test_loaderwithout gradient computa-tion

Collect predictions and compute accuracy, precision, re-call, F1-score**.**

$$\mathbf{h}_t, \mathbf{c}_t = \mathrm{LSTM}(\mathbf{e}_t, \mathbf{h}_{t-1}, \mathbf{c}_{t-1}) \qquad (7)$$

where $\mathbf{h}_t \in \mathrm{R}^{128}$ is the hidden state, and $\mathbf{c}_t$ is the cell state at time step t. The final hidden state $\mathbf{h}_2$ is used as the joint representation of the face-gait pair and passed to a fully

connected layer:

$$\hat{\mathbf{y}} = \mathrm{Softmax}(W_o \mathbf{h}_2 + \mathbf{b}_o) \qquad (8)$$

The output weight matrix is $W_o \in \mathrm{R}^{C\times 128}$, the bias is $\mathbf{b}_o$, and the number of identity classes is C.

The cross-entropy loss function is utilized to train the model:

$$L = -\sum_{i=1}^{C} y_i \log(\hat{y}_i) \quad (9)$$

where y_i is the one-hot encoded ground-truth label. The Adam optimizer is used for 100 epochs of training with a batch size of 4 and a learning rate of 10^{-3}. The common**.**

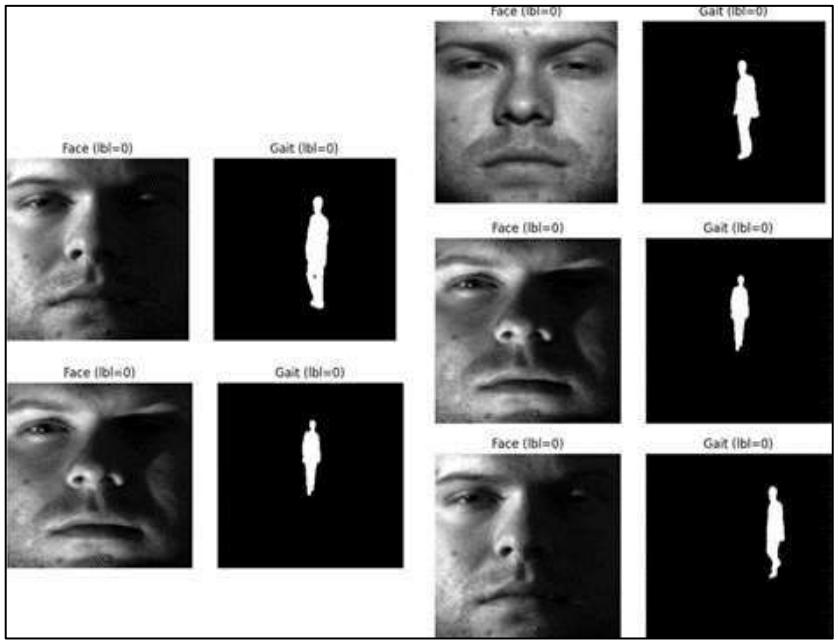

Figure 4. Example face-gait image pairs (label=0) used by the cnn model during training.

classification metrics, used to evaluate the final performance on the test set, include accuracy, precision, recall and F1-score.

The benefit of this type of RNN architecture is that it ex-plicitly computes the sequential dependencies of modalities, and the fusion of face and gait is modeled as the temporal relationship. It is a small, versatile and revealing method of multimodal biometric identification. Figure 5 shows the ar-chitecture of the proposed Two-Channel RNN that is applied to the multimodal biometric classification. The model takes two inputs, a pair of facial image and a pair of gait image,

both of which are resized to 224 × 224. Rather than merging the pictures into a 2D array as in CNNs, each modality is considered a time step of sequential input to an LSTM network.

The first step is the flattening of both face and gait pictures to 1D vectors of length 50176 (224 × 224). The vectors are then called upon an embedding layer which learns to project a high-dimensional vector into a lower-dimensional latent space (usually 128 in size). The step minimizes the compu-tational complexity and enables the model to concentrate on the most important features.

The gait and face vectors are inbuilt into one another, cre-ating a 2-step sequence, which is handled by a simple LSTM single unit. The LSTM models sequential correlation

between the two modalities, basically, it learns a time dependence between the static (face) and dynamic (gait) feature. The output of the LSTM as a final hidden state is then fed into a fully connected (linear) layer that transforms the learned representation to the scores of the classes that relate to the identities of the subject.

The sequential design allows the model to encode in-termodal interactions with a lightweight and interpretable structure, allowing it to be used in real-time or resource-constrained settings.

As outlined in Algorithm 2, the proposed RNN training framework follows four main stages. First, the fused dataset is

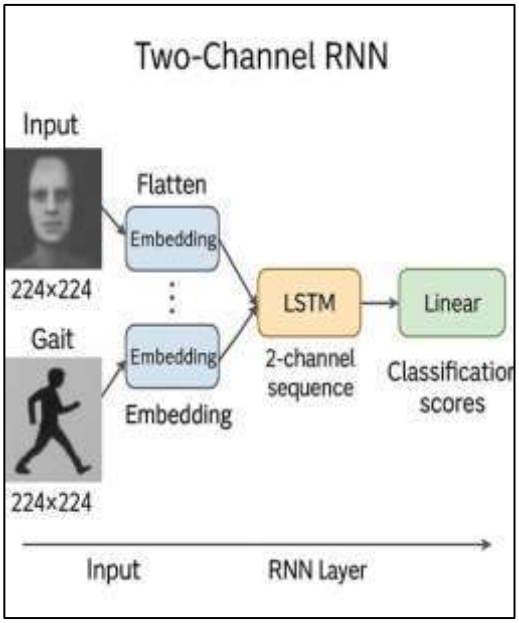

Figure 5. Architecture of the proposed two-channel rnn model for multimodal biometric classification.

loaded and split into training and testing subsets. Each sample is structured as a two-step sequence consisting of a facial image and a gait silhouette, with each pair assigned a class label. In the second stage, the model flattens each 224 × 224 image, applies a fully connected embedding layer to reduce dimensionality, and then feeds the resulting sequence into an LSTM network. The final hidden state from the LSTM is passed to a fully connected layer that produces the classifi-cation logits.

The Adam optimizer and CrossEntropy loss are used to optimize the model during the training phase. The train-ing loop iterates over multiple epochs, performing forward propagation, loss computation, and backpropagation for each batch. In the evaluation phase, the model is run in inference mode on the test set, and standard metrics including accu-racy, precision, recall, and F1-score are calculated to assess performance. Figure 6 displays representative output samples used in the training phase of the proposed Two-Channel RNN model for multimodal biometric classification. The image in the figure has two pairs of images with one grayscale facial image and another one gait silhouette of the same subject (label = 0). The pictures indicate the capability of the model to accommodate intra-subject differences in illumination, facial expression, and walking postures without losing identity-

specific features.

Silhouettes of the gait have steady spatial edges, despite changes in walking directions and loads, whereas natural vari-ability occurs in the face images of pose and light. The RNN model takes advantage of the temporal sequence of the two modalities and encodes each image into a low-dimensional feature space and sequence-processes them using an LSTM. The fact that these samples can be accurately paired and clas-

Algorithm 2 Two-Channel RNN for Face-Gait Classification Fused dataset fused_dataset.pkl, train/test split ratio, epochs, learning rate Trained RNN model and evaluation metrics.

Step 1: Prepare Dataset

Load fused_dataset.pklfrom file

Split into train_datasetand test_dataset

for all samples **do**

Create sequence of 2 images: (face, gait)

Assign label per subject

end for

Step 2: Define Two-Channel RNN Model

Flatten each image to vector of size 224 × 224

Apply embedding: Linear(224^2 → embed_dim)

Stack sequence: shape = (batch, 2, embed_dim)

Feed into LSTM: LSTM(embed_dim → hidden_size)

Final classification: Linear(hidden_size → num_classes)

Step 3: Train the Model

Initialize Adam optimizer and CrossEntropy loss **for** each epochin total epochs **do**

for each batchin train_loader**do** Forward pass through RNN

Compute loss

Backpropagation and weight update

end for

Print average training loss

end for

Step 4: Evaluate the Model

Set model to evaluation mode

Run predictions on test_loader

Compute accuracy, precision, recall, and F1-score

sified attests to the strength of the model in remembering se-quential representations of heterogeneous biometric sources. These findings confirm the usefulness of the RNN-based system when it comes to the relationship of facial and gait fea-tures dynamically, which improves the potential of the RNN-based system in real-world multimodal identity recognition exercises.

IV. Experimental Results

In Table 3, the assessment measures of both the CNN and RNN models on the multimodal face-gait classification task are provided. The CNN model scored 99.47% accuracy, 99.56% precision, 99.47% recall, and F1-score of 99.47%, which marks an excellent performance on all significant mea-sures. These results confirm the model's ability to effectively extract and fuse spatial features from face and gait modalities using convolutional operations, leading to highly discrimina-tive representations.

The RNN model, on the other hand, performed signif-icantly worse, with an F1-score of 42.03%, accuracy of 44.21%, precision of 50.80%, and recall of 44.21%. This

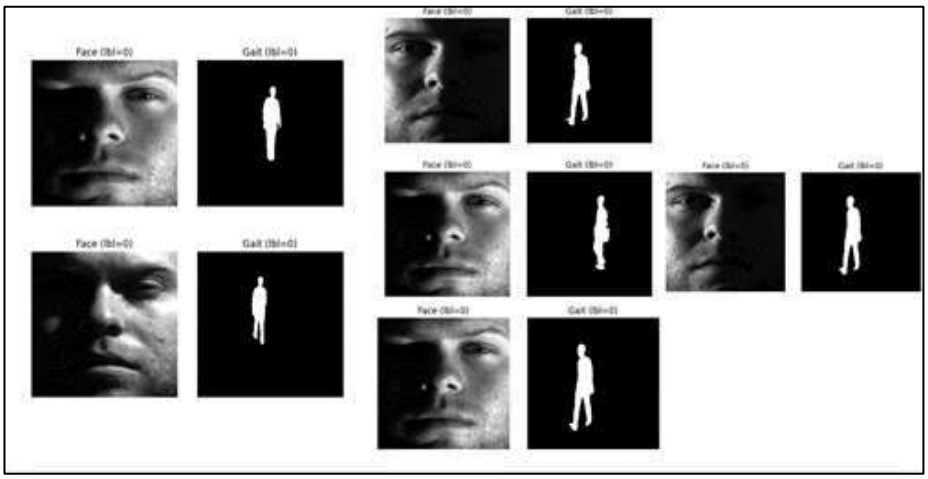

Figure 6. Sample face-gait pairs (label = 0) used during rnn model training.

disparity can be attributed to several factors. First, the se-quential modeling strategy adopted by the RNN treats the face and gait images as two time steps, which may not be sufficient to capture the complex spatial features and inter-modal relationships present in the data. In contrast to CNNs, which are designed to learn spatial hierarchies by defining them on image grids, RNNs operate on flattened data and temporal correlations, which may cause loss of structural information in visual recognition tasks.

Also, the two time steps used by the RNN (one per face, one per gait) might not allow the LSTM to effectively capture temporal dynamics, particularly in the case of an input se-quence that is too short to be useful in the recurrent dynamics. Furthermore, it is common with RNNs that larger and more temporally varied data are necessary to achieve optimal per-formance, and the current data is potentially not utilizing the abilities of recurrent architecture to the fullest.

In general, the CNN model works much better in this task than the RNN model because it is better in extracting spatial features and its alignment with the characteristics of visual information. These results reveal the role of the architecture choice depending on the modality and design of input fea-tures of the multimodal biometric system. Figure 7 depicts a.

Table 3. Performance comparison between cnn and rnn models

Metric	CNN Model	RNN Model
Accuracy	0.9947	0.4421
Precision	0.9956	0.5080
Recall	0.9947	0.4421
F1-score	0.9947	0.4203

comparative bar chart of the CNN and RNN models in the light of four main evaluation factors namely: accuracy, pre-cision, recall and F1-score. The CNN model performs much better than the RNN model as illustrated, as all measures are above 0.99, whereas the RNN model performs poorly with all measures ranging between 0.42 and 0.51. This visual contrast with the convolutional architectures visually validates the advantage of using convolutional architectures over capturing and learning robust spatial representations of face and gait image inputs. The low performance of the RNN in the lower bars demonstrates its shortcomings in this particular two-step sequential learning architecture, and specifically in its inabil-ity to fully utilize the rich spatial nature of visual information. The bar plot therefore offers a direct and easy to grasp idea of the difference in performance of the two approaches**:**

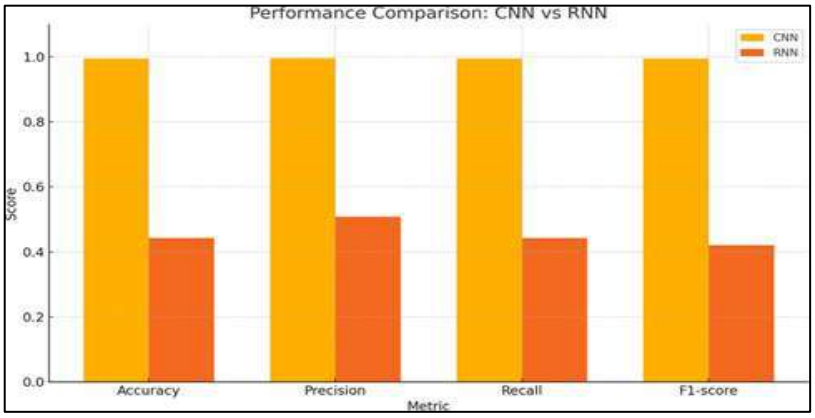

Figure 7. Performance comparison of cnn and rnn models across evaluation metrics.

An extensive array of gait recognition approaches, which overcome the challenges of the latter by incorporating deep learning, has been addressed in the literature, as listed in Table 1. A best feature selection mechanism along with a deep CNN was suggested by Mehmood et al. [10], which achieved an accuracy of 94.26% on the CASIA-B dataset. Although this procedure improved recognition accuracy with the use of an engineered feature set, it could still only be applied to lateral-view gait samples and not to different viewpoints. The framework by Saleem et al. [11] took such notion a step forward by providing a concept of deep feature fusion within a single-stream framework, which raised

the accuracy to 95.57%. Their approach was however not based on the variability of real-world situations like change in clothes or perception of a view.

By using a combination of hybrid deep learning methods and feature selection, Asif et al. [12] obtained one of the highest reported accuracies (96.32%). Their model was more robust but it was costly in terms of computation, thus not allowing its application in real time systems. Mehmood et al. [14] also revisited CNNs with feature selection, and established the advantage of selective representation to improve performance, although their model was limited to a single architecture and did not further investigate alternative modalities or fusion methods. In another field of application, Va-sudevan et al. [13] conducted a study on gait-based diagnosis with deep learning in the medical backdrop and realized an accuracy of 94.50% on a proprietary dataset. Although it has good outcomes, generalizability is hampered by inadequate standardized biometric reference points. A multiview gait recognition model based on spatio-temporal deep features was proposed by Gul et al. [15], and they successfully over-came the problem of view variations but with moderate accu-racy (92.80 per cent) and low interpretability of the learned**.**

Table 4. Comparison of proposed cnn model with related deep learning approaches representations.

Study	Year	Dataset	Method	Accuracy (%)	Limitation
Mehmood et al. [10]	2020	CASIA-B	Feature-selected deep CNN	94.26	Focused on lateral-view gait; lacks view-invariance
Saleem et al. [11]	2021	CASIA-B	Fusion of features (single-stream)	95.57	Lacks clothing/viewpoint variation handling
Asif et al. [12]	2022	CASIA-B	Hybrid feature selection and DL	96.32	High computational cost; not real-time efficient
Gul et al. [15]	2021	Multiview	Spatio-temporal DL fea-tures	92.80	Limited interpretability; moderate accuracy
Song et al. [17]	2022	CASIA-E	Improved models for deep learning	97.03	Requires dataset-specific tuning
Proposed CNN Model	2025	CASIA-B + Yale	Two-channel CNN (face+gait fusion)	99.47	Requires well-aligned multimodal data input

Hasan et al. [16] have performed a comprehensive evalua-tion of CNN versions in terms of CASIA-B data and produced an accuracy of 93.10 percent, which was very high. Although their analysis was insightful regarding CNN-based perfor-mance, it did not explore the areas of hybrid or multimodal approaches that might utilise complementary features. Lastly, Song et al. [17] achieved the best accuracy with enhanced deep learning models which were tested on the larger CASIA-E dataset with an accuracy of 97.03 percent. In spite of the fact that this work produced state-of-the-art results, the model, like the results, depended on dataset-specific tuning, which questions the transferability of the model to other areas or datasets.

Compared to these studies, our suggested CNN-based mul-timodal fusion model has a competitive accuracy of 99.47% with a high level of precision, recall, and F1-score. In contrast to other existing studies that used either gait or hand-selected features, we combine facial and gait features into a two-channel architecture and learn combined cross-modal spatial features. The strategy does not only increase the performance in classification but also in the generalization of subject con-ditions.. On the other hand, our RNN-based model yielded lower scores due to its limited temporal sequence length (two time steps) and inability to capture rich spatial features from flattened inputs. These findings position our CNN approach as a promising solution for robust, multimodal biometric recognition, outperforming many existing gait-specific archi-tectures both in accuracy and general applicability.

V. Conclusion

This study presented a comparative evaluation of two deep learning architectures—Convolutional Neural Networks (CNNs) and Recurrent Neural Networks (RNNs)—for mul-timodal biometric recognition based on fused face and gait data. By constructing a novel dataset from the CASIA-B and Extended Yale B databases, we created subject-consistent pairs of facial images and gait silhouettes to support multi-modal learning.

All evaluation measures showed that the suggested two- channel CNN model performed better than the others, with an accuracy of 99.47%, precision of 99.56%, recall of 99.47%, and F1-score of 99.47%. This finding confirms the ability of the model to effectively extract the spatial information of the face and gait modes and to learn the discriminative repre-sentations. Conversely, the RNN model that trained using the same data as two temporal sequences performed much worse. This result indicates the architectural constraints of sequential modeling in terms of tasks that are more spatial in nature.

The critical significance of architecture choice in multi-modal biometric system is emphasized in our results. Al-though RNNs are optimal in capturing the temporal dynam-ics, their use in image sequences that are not dynamic (i.e. short temporal depth) may result in suboptimal learning. In comparison, CNNs are more effective in capturing spatial correlations and modality-specific textures which are more efficient to capture when inputs are organized as image ten-sors.

Further research can consider hybrid architectures by using CNN and RNN elements to utilize the spatial and temporal dependency at the same time. Also, it is possible to increase the sample size to cover more participants, different perspec-tives and dynamic gait patterns to further confirm the broad applicability of the suggested method. Finally, the paper has added to the rising literature of evidence in multimodal biometric recognition and has highlighted the importance of integrating architectural experimentation with standardized assessment towards state-of-the-art development.

References:

Y. Makihara, M. Nixon, and Y. Yagi, "Gait recognition: Databases, rep-resentations, and applications," *In Computer Vision; Springer: Cham, Switzerland*, 2021.

A. Krizhevsky, I. Sutskever, and G. Hinton, "Imagenet classification with deep convolutional neural networks," *Adv. Neural Inf. Process. Syst.*, 2012.

M. Tan and Q. Le, "Efficientnet: Rethinking model scaling for convolu-tional neural networks," *Proc. Int. Conf. Mach. Learn.*, 2019.

C. Bishop, "Pattern recognition and machine learning," *Springer*, 2006.

T. Kohonen, "The self-organizing map," *Proc. IEEE*, 1990.

S. Zheng, J. Zhang, K. Huang, R. He, and T. Tan, "Robust view transfor-mation model for gait recognition," *Proc. Int. Conf. Image Process. (ICIP)*, 2011.

C. Santos, D. Oliveira, L. Passos, *et al.*, "Gait recognition based on deep learning: A survey," *ACM Comput. Surv.*, 2023.

S. Zhang, Y. Wang, and A. Li, "Cross-view gait recognition with deep universal linear embeddings," *Proc. IEEE/CVF Conf. Comput. Vis. Pattern Recognit.*, 2021.

W. Mutlag, S. Ali, Z. Mosad, and B. Ghrabat, "Feature extraction methods: A review," *J. Phys. Conf. Ser.*, 2020.

A. Mehmood, M. Khan, M. Sharif, *et al.*, "Prosperous human gait recog-nition: An end-to-end system based on pre-trained cnn features selection," *Multimed. Tools Appl.*, 2020.

F. Saleem, M. Khan, M. Alhaisoni, *et al.*, "Human gait recognition: A single stream optimal deep learning features fusion," *Sensors*, 2021.

M. Asif, M. Tiwana, U. Khan, *et al.*, "Human gait recognition subject to different covariate factors in a multi-view environment," *Results Eng.*, 2022.

P. Vasudevan, P. Sharma, and R. Ramesh, "Gait image classification using deep learning models for medical diagnosis," *Comput. Mater. Continua*, vol. 74, pp. 6039–6063, 2023.

A. Mehmood, M. Ali, M. Khan, J. Ahmad, and M. Rehman, "Human gait recognition: A deep learning and best feature selection framework," *Comput. Mater. Contin.*, vol. 70, pp. 343–360, 2022.

S. Gul, J. Ahmad, S. Shams, A. Wahab, M. Zafar, and S. Awan, "Multi-view gait recognition system using spatio-temporal features and deep learning," *Expert Syst. Appl.*, vol. 179, p. 115057, 2021.

M. Hasan, S. Alam, and S. Hossain, "Evaluating cnn models for gait recognition: A study on the casia-b dataset," *GUB J. Sci. Eng.*, vol. 10,

pp. 17–26, 2023.

C. Song, M. Tang, J. Li, W. Zeng, and Y. Zhou, "Casia-e: A large com-prehensive dataset for

gait recognition," *IEEE Trans. Pattern Anal. Mach. Intell.*, vol. 45, pp. 2801–2815, 2022.

M. Deng, Z. Fan, P. Lin, and X. Feng, "Human gait recognition based on frontal-view sequences using gait dynamics and deep learning," *IEEE Trans. Multimed.*, 2024.

S. Hou, C. Fan, C. Cao, X. Liu, and Y. Huang, "A comprehensive study on the evaluation of silhouette-based gait recognition," *IEEE Trans. Biom. Behav. Identity Sci.*, 2023.

L. Qin, M. Guo, K. Zhou, *et al.*, "Gait recognition based on two-stream cnns with multisensor progressive feature fusion," *IEEE Sens. J.*, 2024.

A. Sepas-Moghaddam and A. Etemad, "Deep gait recognition: A survey," *IEEE Trans. Pattern Anal. Mach. Intell.*, vol. 45, pp. 264–284, 2023.


KAWADA

المؤتمر الدولي الثاني للعلوم الهندسية

II. International Conference on Engineering Sciences

ISBN 978-625924390-0

Rimar Academy
Publishing House